Doctoral Thesis

# Effects of Surface Characteristics in Pool Boiling Critical Heat Flux Enhancement, and its Prediction Model

Han Seo

Department of Nuclear Engineering

Graduate School of UNIST

2017

# Effects of Surface Characteristics in Pool Boiling Critical Heat Flux Enhancement, and its Prediction Model

Han Seo

Department of Nuclear Engineering

Graduate School of UNIST

# Effects of Surface Characteristics in Pool Boiling Critical Heat Flux Enhancement, and its Prediction Model

A dissertation
submitted to the Graduate School of UNIST
in partial fulfillment of the
requirements for the degree of
Doctor of Philosophy

Han Seo

1. 16. 2017

Approved by

Bang, In Cheol

Advisor

Prof. In Cheol Bang

# Effects of Surface Characteristics in Pool Boiling Critical Heat Flux Enhancement, and its Prediction Model

Han Seo

This certifies that the dissertation of Han Seo is approved.

1. 16. 2017

signature

Advisor: In Cheol Bang

signature

Jae Young Lee

signature

Ki-Yong Choi

signature

Ji Hyun Kim

signature

Heungjoo Shin

# Abstract

In nuclear power reactors, most of studies related to thermal-hydraulics have focused on increasing power density, efficiency, and safety of currently operating nuclear power reactors. The primary constraint in the aspect of thermal-hydraulics is determining and controlling of departure of nucleate boiling (DNB), called as critical heat flux (CHF). When the CHF is occurred, bubbles and vapors, which heat transfer coefficient is very low compared to liquid, covered whole heating surface; thus the temperature of heating surface will increase rapidly. The rapid increment of the fuel rod and cladding surface temperature due to the CHF will destroy the second barrier of the defense in depth and may release dangerous fission products in containment building or environment. This inferred that an accurate prediction of the CHF phenomenon is important because it is related to the safety of the environment. In addition, CHF enhancement enables increasing power density and safety margins of reactors; the CHF enhancement study and development of the accurate CHF prediction model should be conducted. In the present research, therefore, CHF enhancement studies based on surface modifications on a plain heating surface and modified CHF model that includes the effects of surface characteristics are presented.

For the CHF enhancement studies, surface modification techniques have been widely studied: deposition of nano- or micro-particles, mechanical machining, and micro-electro-mechanical techniques. In the present CHF enhancement study, deposition of nanoparticles (SiC and graphene) on a plain heating surface was used for the porous heating surfaces. Nonporous heating surfaces were also examined to compare with the porous heating surfaces. In addition, a hybrid graphene/SWCNTs heating surface was considered to show the effect of thermal properties for the heating surfaces on boiling performance. Surface characteristics for various heating surfaces were considered as the CHF enhancement parameters. Infrared (IR) thermometry was used to visualize the heating surfaces and several methods were applied on the parameter studies to quantify the enhancement mechanism. The discussed surface parameters were surface wettability, roughness, capillarity, permeability, porosity, and thermal effusivity. Because all the surface parameters are coupled each other, it was difficult to determine the major parameters that influence on the CHF performance. Therefore, several CHF models, such as hydrodynamic instability theory, bubble force balance, microlayer dryout, bubble interaction, and hot/dry spot, were evaluated to determine the appropriate the CHF prediction model in comparison of the experimental results. As a result, modified hydrodynamic instability theory was selected as one of the CHF enhancement model because it can predict the CHF enhancement trends when the effect of surface characteristics was considered as a change of RT instability wavelength.

Hydrodynamic instability theory has been widely used as the CHF prediction model because it can predict well under plain heating surface conditions. The hydrodynamic instability theory assumed that there is a critical region that the liquid could not penetrate into the heating surface and this point is

called as the CHF point. The critical vapor velocity was derived by Kelvin–Helmholtz (KH) instability. However, the measurement of the critical vapor velocity at near the CHF point is impossible because vigorous boiling is occurred on the heating surfaces under nucleate boiling situation. Instead of measuring critical vapor velocity or KH instability wavelength, Rayleigh–Taylor (RT) instability wavelength was considered as the KH instability wavelength. The present approach is started from the change of the critical vapor velocity due to the change of heating surfaces. Critical and the most dangerous RT instability wavelengths were applied on the hydrodynamic instability model and further approximation to derive the CHF prediction model was conducted. However, there are several assumptions in the hydrodynamic instability theory and these assumptions should be evaluated to provide credibility of the model. Therefore, the relation between RT and KH instability wavelengths and the consideration of the surface effects on the change of RT instability wavelengths incorporated into the hydrodynamic instability theory, called as a modified hydrodynamic instability approach, was studied in the present research. The relation between RT instability wavelength and CHF was examined in a pressurized wire pool boiling facility with various kinds of Ni-Cr wire diameters. The results indicated that that it is possible to make the relation between the RT instability wavelengths and the CHF values by using the modified hydrodynamic instability approach. Not only using the bare Ni-Cr wire surface, various kinds of nanoparticle-deposited heating surfaces were considered to evaluate the modified hydrodynamic instability CHF model. A correlation for the change of RT instability wavelength based on the experimental results was proposed to predict the CHF enhancement based on the heating surface characteristics. Because the RT instability wavelength which was determined by the effects of heater geometries can explain all the reasons of CHF enhancement in pool boiling conditions, the surface roughness and factor was also examined in the validation procedure for the proposed CHF model. The validation results indicated that the modified hydrodynamic CHF model is valid in the present research.

# Contents

**List of figures**

**List of tables**

**Nomenclature**

| | | |
|---|---|---|
| A | heat transfer area | [$m^2$] |
| C | specific heat | [J/kgK] |
| D | diameter | [m] |
| E | thermal effusivity | [$J/m^2Ks^{1/2}$] |
| g | acceleration due to gravity | [$m/s^2$] |
| h | latent heat | [J/kg] |
| I | current | [A] |
| k | thermal conductivity | [W/mK] |
| L | heating element length | [m] |
| l | liquid flow path | [m] |
| N | nucleate site density | [$m^2$] |
| P | applied pressure | [bar] |
| q" | heat flux | [$kW/m^2$] |
| Q | volumetric flow rate | [$m^3/s$] |
| r | pore size | [m] |
| R | roughness | [m] |
| S | mean spacing of roughness | [m] |
| u | velocity | [m/s] |
| V | voltage | [V] |

*Greek symbols*

| | | |
|---|---|---|
| β | receding contact angle | [$^o$] |
| δ | thickness | [m] |
| ε | porosity | [%] |
| θ | static contact angle | [$^o$] |
| λ | wavelength | [m] |
| μ | viscosity | [kg/ms] |
| ρ | density | [$kg/m^3$] |
| σ | surface tension | [N/m] |
| τ | time | [s] |

| | | |
|---|---|---|
| ρ | density | [kg/m$^3$] |

*Subscripts*

| | |
|---|---|
| ac | actual |
| b | bubble |
| c | critical |
| d | bubble dryout |
| CHF | critical heat flux |
| e | equivalent |
| h | heater |
| l | liquid |
| lv | vaporization |
| KH | Kelvin-Helmholtz |
| m | modulation |
| mea | measured |
| p | projected |
| RT | Rayleigh-Taylor |
| th | theoretical |
| v,c | critical vapor |
| w | bubble waiting |
| Z | Zuber |

# Chapter 1. INTRODUCTION

## 1.1 Research Background and Motivation

Energy conversions and managements have been an important topic in these days because the efficiency for transformation of energy from sources such as fossil and nuclear fuels into useful forms such as thermal, mechanical, and electric energy is related to economic. One of the efficient methods energy transfer is boiling method because it delivers a latent heat, which is the phase change heat transfer parameter from a liquid to vapor, governs the heat transfer process in boiling situation. Phase change by boiling is a highly efficient heat transfer method because it accommodates high heat fluxes with relatively small wall superheat compared to the natural convection mode. Therefore, nucleate boiling mode has widely used in industrial fields. However, there is a limit of nucleate boiling, which is called as critical heat flux (CHF). Fig. 1-1 shows an ideal pool boiling curve from natural convection to CHF point. There is a certain point that the wall superheat is decreased due to the start of the boiling and it is called as onset of boiling (ONB). The black line shows a typical pool boiling curve, and the other lines imply the boiling curves for which the CHF and the boiling heat transfer (BHT) are enhanced due to the surface modifications. As shown in Fig. 1-1, if the BHT could be enhanced, a large amount of heat can be removed at low wall superheat. This means that effective heat transfer as well as CHF enhancement could be achieved. As the applied heat flux is increased, the wall superheat will increase as well as heat transfer coefficient (HTC). Therefore, it is important to predict the CHF point and enhance the CHF for the safety of the power devices. Power industries determine the operation upper limit based on the CHF region. If the power density of devices exceeds the CHF region, the wall temperature of the heating surfaces will increase rapidly because the heat transfer capability of the vapor films is much lower than the liquid layer or mixture of liquid and bubble. The device could be damaged due to the heater burnout. This inferred that the enhancement CHF region can prevent the heater burnout and provide highly efficiency of power plants. Therefore, the CHF enhancement experiments are performed by surface modifications and development of the accurate CHF model that includes the effects of surface characteristics is presented. The CHF enhancement studies were performed by porous and nonporous heating surfaces and the CHF enhancement model was developed based on a hydrodynamic instability theory.

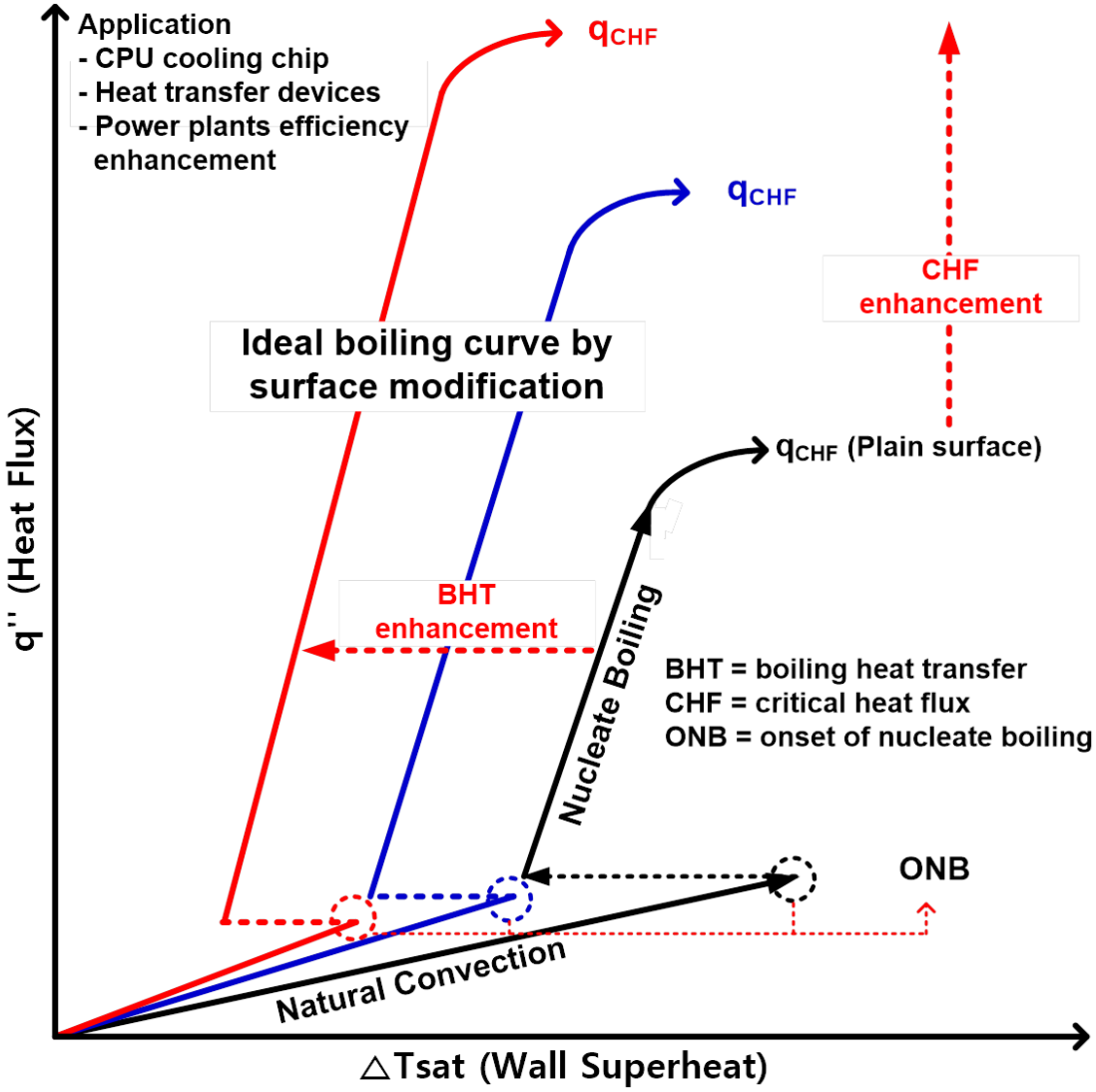


Fig. 1-1. Typical boiling curves

### 1.2 General Literature Reviews

Numerous studies have been conducted to enhance the CHF and the BHT phenomena based on heating surface modification techniques. Various methods of heating surface modification aimed for the CHF and BHT enhancement were suggested, such as deposition of nano- or micro-particles, mechanical machining, and micro-electro-mechanical system (MEMS) techniques. The deposition of nano- or micro-particles on heating surfaces has been widely studied because it gives rise to a very large surface area, which results in enhancement of the CHF and BHT[1-12]. The enhancement mechanisms that use deposition of particles on heating surfaces can be explained by improved surface wettability[4-7], formation of a porous structure[8-9], and change of the modulation wavelength[9-12]. However, several studies revealed that the enhanced surface wettability did not play significant role in the BHT enhancement. To decouple the effect of the surface wettability, a refrigerant was used on a nanoparticle-coated surface, and the results indicated that the BHT might be enhanced[12]. In addition, the effects of thermal properties of the heating surface and the working fluid on CHF and BHT have been reported[13-14]. In area of mechanical machining techniques, surface modifications were performed from the nanometer to millimeter scales. Polishing and sand blasting[15-17], electrical discharge machining[18-19], and shape-memory alloys[20] have been used to modify the heating surface structure; enhancements in the CHF and BHT were observed using these techniques. In the present research, deposition of nanoparticles through boiling of nanofluids was conducted to make the porous heating structures and nonporous heating surfaces with the same materials that were used in the porous heating surfaces were fabricated by deposition of coating layers through various systems for comparison.

Nanofluids are a new concept of nanotechnology-based heat transfer fluids fabricated by dispersing nanoparticles into conventional fluids, such as water, ethylene glycol, etc. Choi et al.[21] revealed that the heat transfer performance (thermal conductivity) by adding metal and metal oxide nanoparticles on base fluids can be significantly enhanced. The first boiling experiment using alumina-water nanofluids showed that the CHF can be enhanced up to 200% compared to the base fluid[1]. Vassallo et al.[2] performed wire pool boiling experiments with silica-water nanofluids and the experimental results showed that the CHF limit was enhanced up to 60%. Bang and Chang[3] performed plate pool boiling experiments under alumina-nanofluids and the results indicated that the CHF performance was enhanced, while the HTC was deteriorated. The deposition of nanoparticles changed the surface conditions and it discovered as the influencing parameter of CHF and HTC. From these start of nanofluids in boiling experiments, various kinds of application efforts using nanofluids under pool boiling, flow boiling, and quenching experiments have been conducted. In addition, enhancement mechanisms in boiling have been analyzed based on the prediction models for providing precise enhancement mechanisms for industrial applications.

The boiling experiments under pool boiling conditions have been widely conducted because the

influencing parameters on boiling performance are limited to the heater conditions. The first pool boiling experiment using $Al_2O_3$-nanofluid was conducted[1]. The experiment was conducted under low pressure condition using $Al_2O_3$ nanofluids on a flat square copper surface. The results showed that the CHF increased dramatically while the boiling heat transfer coefficients (HTCs) were almost same compared to the bare surface. They argued that the change of the surface tension due to the nanoparticles could bring the CHF enhancement, but it is difficult to fully understand the enhancement mechanism based on the hydrodynamic theory proposed by Zuber[22]. Vassallo et al.[2] used $SiO_2$ nanofluids under wire pool boiling experiment. They referred that CHF could be enhanced due to the change of surface roughness which brought the difference in nucleate site density and heat transfer mechanism. The change of surface roughness due to the nanoparticles was firstly observed by Bang and Chang[3]. Various concentrations of $Al_2O_3$ nanofluids were examined in the plate pool boiling with horizontal and vertical conditions. They used Rohsenow correlation which represented the effects of liquid and heating surface on the boiling performance. Owing to the change of surface roughness by the addition of the alumina nanoparticle, the decrease in the HTCs was observed while the CHF could be enhanced because of the change of the nucleate site density which can delay the bubble coalescences[23]. The observation of surface characteristics through scanning electron microscopy (SEM) was conducted under the deposition of $TiO_2$ nanoparticles[4]. The change of the material and dispersion conditions of the nanoparticles would bring the significant CHF enhancement. In particular, they reported that deposition of the nanoparticles on the heating surfaces could provide the capillary structure, which can give an additional liquid supply into the heating surfaces. Various kinds of nanofluids ($Al_2O_3$, $ZrO_2$, and $SiO_2$ nanoparticles) were examined in a plate pool boiling and the results showed that the surface wettability due to the deposition of the nanoparticles on the heating surfaces was changed[5]. Contact angles of a sessile droplet on the heating surfaces showed that the deposition of nanoparticles brought hydrophilic surface characteristics by referring the effective solid-liquid contact area differences due to the change of surface roughness. An equivalent thickness of the liquid film which considered the surface wettability was considered as the main enhancement mechanism in the study. In addition, various CHF enhancement mechanisms were introduced. They provided mechanisms of nanoparticle depositions on heating surfaces, enhanced surface wettability based on modified Young's equation which considered surface roughness parameter, and the effect of nanoparticles on nucleate boiling performance. As the effect of nanoparticle deposition on CHF performance, hydrodynamic instability theory, macrolayer dryout theory, hot/dry spot theory, and bubble interaction theory were discussed.

Most of studies using nanofluids have insisted that the enhancement in CHF can be illustrated by the surface wettability improvement, but the conflict results on the CHF enhancement were reported[10]. They reported conflict experimental results using carbon-based of nanofluids. The graphene oxide nanofluid showed the most enhanced CHF result, compared to other nanofluids used in that study, but the wettability and capillarity were not improved. They recognized that improved surface wettability and

capillarity could not explain all the CHF enhancement results. Modulation wavelength concept that was modified from hydrodynamic instability theory was introduced as the CHF enhancement mechanism[11].

### 1.3 Objectives and Scope

The present study aims for CHF enhancement study based on surface modifications through deposition of nanoparticles and various coating layers. In addition, modified CHF prediction model based on hydrodynamic instability theory is presented. The deposition of nanoparticles was performed by the boiling of nanoparticles and various coating layers (graphene, SiC, SWCNTs, and hybrid graphene/SWCNTs) were prepared by different deposition techniques. After the CHF enhancement experiments, various CHF models were evaluated to find the most appropriate model which can support the CHF enhancement results. Modified hydrodynamic instability approach was considered as the CHF enhancement mechanism model. For the CHF model based on the modified hydrodynamic instability theory, plate and wire pool boiling experiments were conducted with various experimental conditions to measure the RT instability wavelengths. Based on the measurement results, the modified CHF prediction model was developed. Based on the experimental results and experimental data obtained from literatures, the modified hydrodynamic CHF model was validated.

The present work can be divided into the 3 parts.

1) CHF enhancement experiments through surface modification techniques
2) CHF experiments based on hydrodynamic instability theory (measurement of RT instability wavelengths)
3) Development of a modified hydrodynamic instability CHF model

In chapter 1, research background and motivation, and general literature reviews related to the boiling experiments were introduced with the objective of the present research.

In chapter 2, plate pool boiling experiments were described under various heating surfaces to analyze CHF enhancement mechanisms under highly-wettable working fluid. The purpose of using the highly-wettable working fluid was to suppress a wettability effect because there are conflict CHF enhancement results related to the surface wettability. Various kinds of heating surface characteristics were defined and evaluated based on the experimental results including various CHF prediction models. Based on the evaluation of the CHF models based on the experimental results, hydrodynamic instability theory as the CHF enhancement mechanism was described.

In chapter 3, CHF experiments related to the hydrodynamic instability theory were performed. Measurements of the RT instability wavelength under various system pressures and heater conditions were performed to find the relationship the RT instability wavelength and the CHF performance. The results showed that the RT instability wavelengths were related to the CHF results. These results indicated that the critical vapor velocity can be changed by the RT instability wavelengths.

In chapter 4, the modified hydrodynamic instability CHF prediction model was proposed and

validated with the experimental results from the present experimental data and literatures. The surface characteristics were included in the modified CHF model. Measured RT instability wavelength as the function of surface characteristic was validated and surface roughness parameter was also examined for the validation of the CHF model. By comparing the prediction model with the experimental results, the modified CHF model was validated.

The conclusions and recommendations were described in chapter 5.

# Chapter 2. POOL BOILING CHF ENHANCEMENT EXPERIMENTS

## 2.1 Introduction

The CHF enhancement studies using nanofluids or nanoparticle-coated surfaces have widely conducted because significant CHF results were measured under various concentrations and types of nanofluids or nanoparticle-coated heating surfaces. To quantify the CHF enhancement mechanisms, various kinds of surface parameters that may influence on the CHF results have been suggested, but the exact enhancement mechanism was not proved yet. Several kinds of CHF enhancement parameters and CHF enhancement theories were suggested. For the surface parameters, surface wettability, surface roughness, surface capillarity, porosity, permeability, and thermal effusivity or activity were considered. One of the widely introduced as the CHF enhancement parameter was the improved surface wettability, but several studies argued that significant CHF enhancement ratio was observed even though the surface wettability of the heating surfaces was not improved. This means that the CHF enhancement study that can suppress the effect of surface wettability is needed. Therefore, in the present work, plate pool boiling experiments with porous and nonporous structures of heating surfaces and deposition of graphene and hybrid graphene and SWCNTs surfaces were examined using FC-72 refrigerant, which makes the heating surfaces as hydrophilic characteristics due to its surface tension (0.01 N/m).

The motivation of using SiC and graphene materials is as follow. A class of candidates that are suitable for use in extreme-environment applications is SiC materials, which can withstand high temperatures and high-radiation environments. The use of SiC materials has been studied in space applications and nuclear applications, such as fast reactors and nuclear fusion reactors, which have more severe conditions than existing systems[24]. There is no doubt that boiling surfaces constitute extreme conditions. For that reason, nanofluid applications of SiC materials have been tested for enhancement of heat transfer[25]. In addition, the use of graphene can be applied in nuclear conditions because it shows very high thermal conductivity[26-28] and it has low absorption cross section of carbon.

To find the CHF enhancement mechanisms, the analysis of surface parameters was performed. In addition, the CHF enhancement prediction model that can cover the all CHF results was suggested based on the experimental results with evaluation of various CHF models.

## 2.2 Experimental Setup

The pool boiling CHF enhancement experiments was conducted in a plate pool boiling facility under highly wettable fluid. Two kinds of the CHF tests were considered: the effect of porous and nonporous surfaces, and the effect of thermal effusivity that reflects of heat dissipation capability. During the experiments, infrared (IR) thermometry was prepared to measure the temperature fields of the heating

surfaces and detect CHF points.

### 2.2.1 Experimental apparatus

Fig. 2-1 exhibits schematic diagram of the experimental facility. A boiling vessel with dimensions of 200 × 200 $mm^2$ with a 180 mm height was prepared by transparent material of polycarbonate to observe the boiling occurrence at every face. There are four cartridge heaters (1.6 kW total power) that were embedded in the boiling vessel to maintain the desired temperature of the working fluid through proportional integral differential (PID) controller with two T-type thermocouples. A DC power supply with having a maximum voltage and current of 150 V and 35 A was used to control the heat fluxes that applied to the heating surfaces. The voltage and the current data were collected by a data acquisition system (DAS) with a 250 ms period. The applied heat flux on the heating surfaces was calculated as follows.

$$q'' = \frac{V_h I_c}{A_h} \qquad (2\text{-}1)$$

where $V_h$, $I_c$, and $A_h$ are voltage and current applied on the heating surfaces and the area of the heating surfaces, respectively.

### 2.2.2 Fabrication procedure of various heating surfaces

To conduct the CHF experiments, several kinds of heating surfaces were prepared: bare indium tin oxide (ITO), porous and nonporous structures prepared by the SiC and the graphene nanoparticles, and highly thermally conductive graphene and hybrid graphene/SWCNTs surfaces. All modified heating surfaces were deposited on the bare ITO heating surface. The purpose of using porous and nonporous structures was to show the deposition effect (porous and nonporous heating surfaces) on the CHF and BHT performances. On the other hand, the deposition of single-layered graphene and the hybrid graphene and SWCNTs surfaces was aimed for showing the effects of the thermal effusivity parameter on the boiling performance.

An ITO layer was used as a heating surface and it was deposited on a sapphire substrate (1 mm thickness). The area of the sapphire substrate was 50 × 50 $mm^2$, while a 750 nm thick with having 50 × 32 $mm^2$ area of ITO layer was deposited at the center of the sapphire substrate. To apply the power from the DC power supply, silver layers with an area of 9 × 32 $mm^2$ were deposited at the left and right side of the ITO layer. As a result, an actual heating surface of the ITO layer was 32 × 32 $mm^2$. An average sheet resistance of the ITO layer was ranged from 9 to 11 ohm/sq via an annealing process. Fig.

2-2 (a) shows a plain heater surface and Figs. 2-2 (b) and (c) exhibit scanning electron microscopy (SEM) images of the ITO layer and the boundary surface between the silver busbars and the ITO layer.

For the porous heating surfaces, deposition of the nanoparticles with boiling of nanofluids was conducted. Two kinds of nanoparticle materials were selected: SiC and graphene-oxide (GO). Transmission electron microscopy (TEM) was used to analyze the material morphology. SiC nanoparticles have a shape of spherical with having 100 nm average diameters, while the GO particles are plate-shape with a thickness of ~1 nm. To deposit the nanoparticles on the ITO heating surface, the 0.01 vol% of nanofluids by dispersing the nanoparticles in distilled water and sonication procedure for an hour was conducted to stabilize the mixture. After the sonication process, boiling of the nanofluids on the ITO heating surface was performed to make the porous structures with SiC and GO materials. The nanofluids were boiled for 15 min with continuous heat flux of 632 $kW/m^2$ with saturated condition (100 $^oC$) of the working fluids. During the boiling process, the reduction process of the GO nanofluid was appeared: the brown-colored of the GO nanofluid was changed to the black-colored fluid. This inferred that the characteristic of GO nanoparticles was changed to reduced graphene oxide (RGO) nanoparticles. The characteristics of RGO are similar to the graphene[29], thus the porous structure of the GO nanoparticles was assumed to be the graphene nanoparticles. Fig. 2-3 exhibits the surface images of the SiC and graphene nanoparticle-coated surface. The average thickness of the SiC and the graphene surfaces was measured as ~ 7.9 μm and ~3.4 μm, respectively.

For the nonporous heating surfaces of the SiC and graphene, plasma-enhanced chemical vapor deposition (PECVD) and rapid thermal anneal (RTA) processes were used, respectively. The nonporous SiC surface was deposited by using $SiH_4$ and $CH_4$. Because the operation temperature of the PECVD was lower than the conventional CVD process, the surface characteristics of the bare ITO heating surface were not changed. The optimized flow rates of $SiH_4$ and $CH_4$ were selected as 20 and 300 $cm^3$/min, respectively. The nonporous SiC surface was coated with 3 μm thickness by controlling the deposition of the SiC layer. On the other hand, the nonporous graphene layer was grown on a nickel surface by the RTA under vacuum condition. The nickel films were prepared on a $SiO_2$/Si wafer substrate with a thickness of ~100 nm at ~450 $^oC$ in the commercial evaporator. After the nickel films that were grown on the wafer substrate, the sample was annealed at ~1000 $^oC$ for 5 min using the RTA system: the high temperature annealing process changed the nickel samples to the few-layered graphene films[30]. The few-layered graphene surface was then transferred from the wafer substrate to the bare ITO heating surface through a spin coating technique with a poly(methyl methacrylate) (PMMA) solution. The SEM images of the nonporous SiC and graphene surfaces were presented in Fig. 2-4. As shown in the SEM images, the nonporous SiC surface had nano-smooth surface and the surface morphology of the nonporous graphene film showed as patches of different thicknesses, due to the characteristics of the RTA process.

For the hybrid graphene/SWCNTs heating surface, three kinds of the heating surfaces were prepared:

single-layered graphene, SWCNTs, and the hybrid graphene/SWCNTs layers. The hybrid heating surface was to determine the thermal properties on the CHF and BHT. The single-layered graphene surface was prepared by a CVD method because this method provided graphene as a single-layer with a large area. The Cu foil was used as the graphene growth material. The Cu foil was put in the CVD chamber for heating process with a flow of $H_2$. After annealing process, the single-layer graphene surface was transferred from the Cu foil to the bare ITO heating surface. For the hybrid graphene/SWCNTs layers, a simple technique of spray coating with SWCNTs was used. The SWCNTs have diameters and the lengths of 1.4–1.7 nm and 5–20 μm, respectively. The amount of SWCNTs of 4 μl was used based on the optimized sheet resistance of the hybrid films. To compare the graphene and the hybrid graphene/SWCNTs coated layers, only SWCNTs with the same amount that was used on the bare ITO heating surface was prepared to decouple the CHF performances of the graphene and SWCNTs. Fig. 2-5 indicates the SEM images of the various coating layers: the single-layered graphene, the hybrid graphene/SWCNTs, and the SWCNTs. As shown in the SEM image of the single-layered graphene, there were wrinkles or disconnected areas on the graphene surface. The high thermal conductive performance of the graphene can be deteriorated due to the wrinkles or disconnected lines. To compensate the degradation of thermal performance, SWCNTs were deposited randomly on the single-layered graphene surface. Fig. 2-5 (b) shows the SWCNTs deposition on the single-layer graphene surface where the wrinkles or line disruption areas are existed. By incorporating the SWCNTs on the graphene surface, the electrical conductivity can be enhanced based on the results of the sheet resistance, ultimately showing an enhanced thermal conductivity based on the Wiedemann-Franz law.

Table 2-1 summarized the purpose of using various kinds of heating surfaces in pool boiling experiments. The porous and nonporous heating surfaces applied to show the effects of heating surface structures and the hybrid graphene/SWCNTs surface was used to show the effect of the thermal properties of the heating surfaces. The single-layered graphene, SWCNTs, and hybrid graphene/SWCNTs surfaces can be also considered as the nonporous surfaces because the deposition thickness was ranged in the nano-scale and these structures did not have any cavities on the heating surfaces.

### 2.2.3 Test procedure

The plate pool boiling experiments were conducted under the saturation condition of the FC-72 working fluid ($T_{sat}$ = 56 $^{o}$C) through the PID controller. All the measurement data such as voltage and current were recorded through the DAS. The voltage control used to control the heat flux applied on the heater during the experiments. The heat flux was increased stepwise until the CHF appeared on the heating surfaces. The heat flux control was increased as ~ 10 kW/m$^2$ and ~1 kW/m$^2$ when there was a sufficient margin and close to the CHF, respectively. For measurement of temperature fields for the

heating surfaces, the IR thermometry was used. The IR intensity of the heating surface was detected through a gold-coated mirror. Because the ITO layer is opaque at the IR mid-region (3–5 μm), the investigation of the wall temperature and the bubble behaviors at the bottom of the heating surface was possible by using the IR thermometry. The resolution of the IR thermometry with 320 × 256 pixels with 172 fps was used to capture the boiling phenomena. A calibration process for all heating surfaces was conducted by matching the IR intensity to the temperature of heating surfaces obtained from a thermocouple. Fig. 2-6 exhibits an example of the calibration result. The calibration results showed that the maximum measurement error was less than 1 %. All the CHF tests were repeated at least three times with the same heating surface conditions to obtain the reliability of the experimental results.

Table 2-1. Heating surface characteristics

| Purpose | Heater | Fabrication method |
|---|---|---|
| | Bare ITO | CVD method |
| Porous & Nonporous | Nonporous graphene | RTA method |
| | Nonporous SiC | PECVD method |
| | Porous graphene | Boiling-induced deposition of nanofluids |
| | Porous SiC | |
| Thermal Effusivity | Single-layer graphene | CVD method |
| | Graphene/SWCNT | CVD and spray methods |

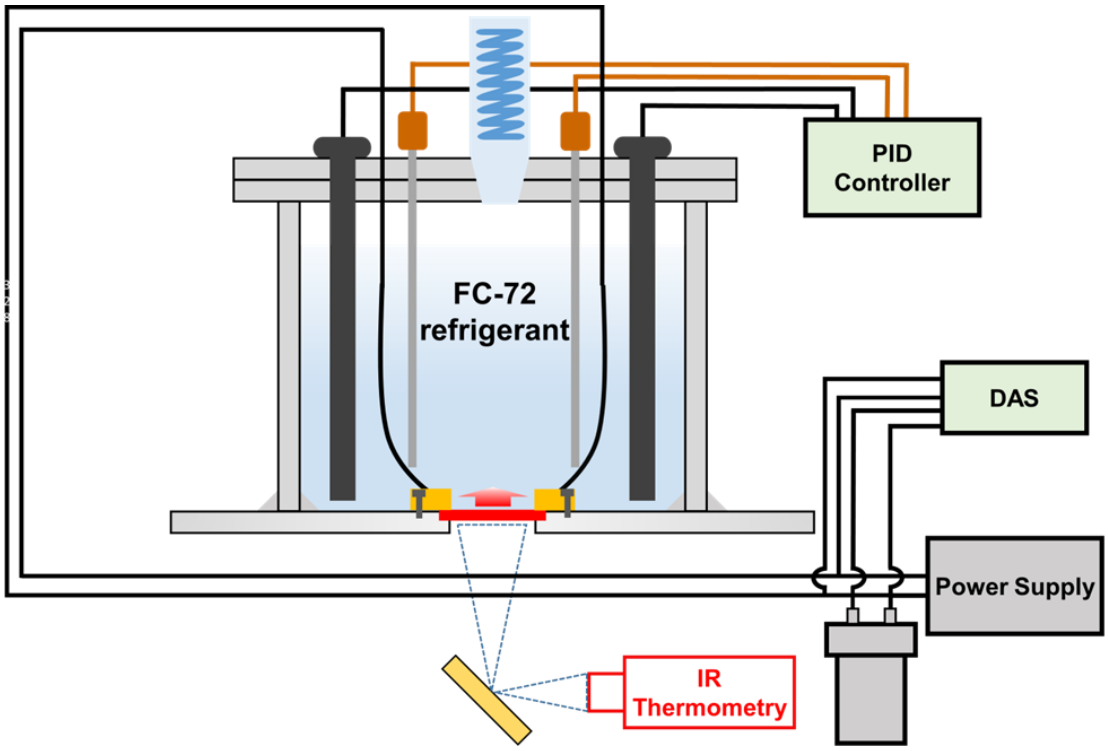


Fig. 2-1. Plate pool boiling facility

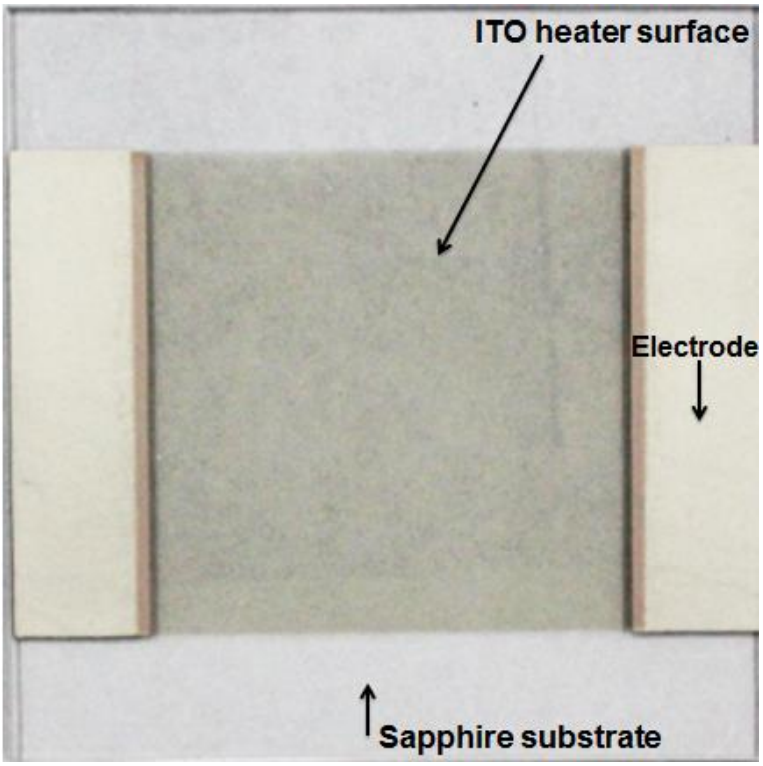


(a)

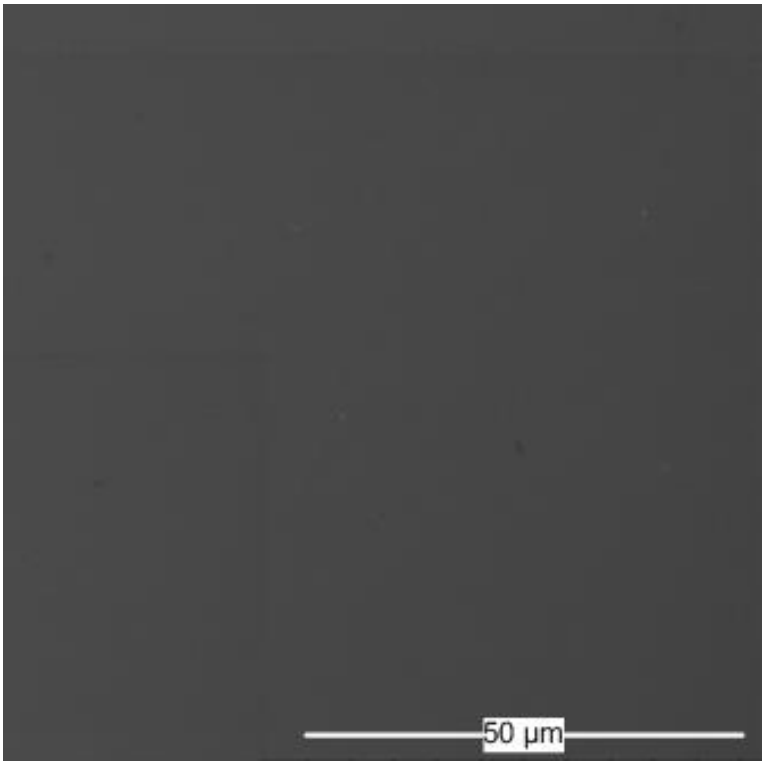


(b)

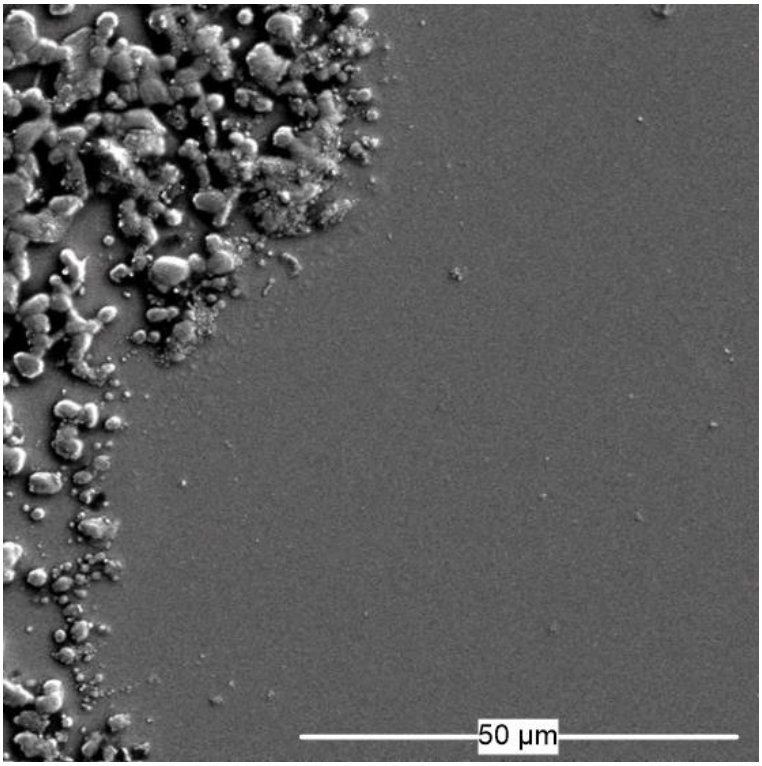


(c)

Fig. 2-2. ITO heater: (a) heater sample, (b) SEM observation of ITO heating surface, (c) boundary between ITO layer and silver electrode

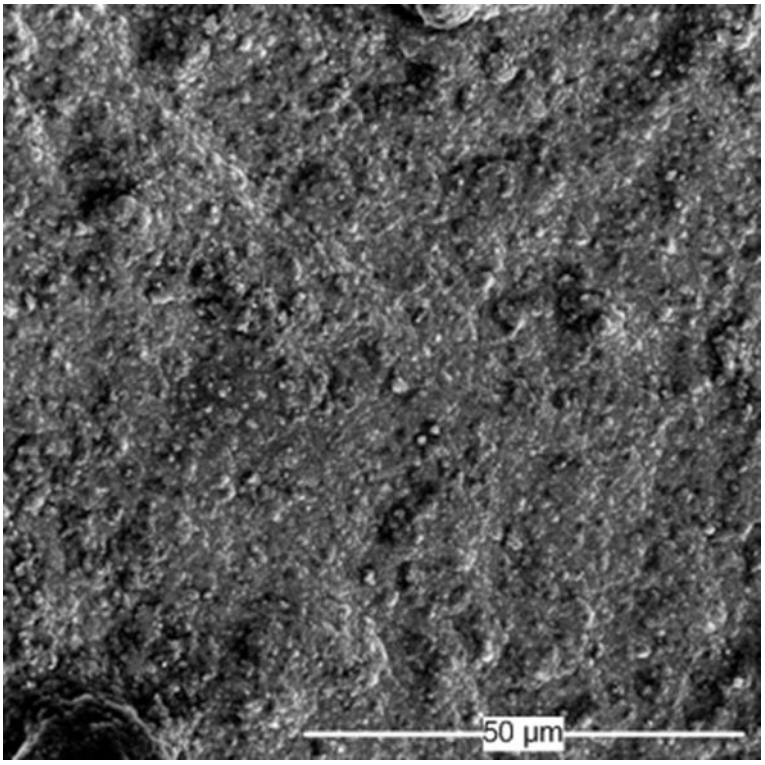


(a)

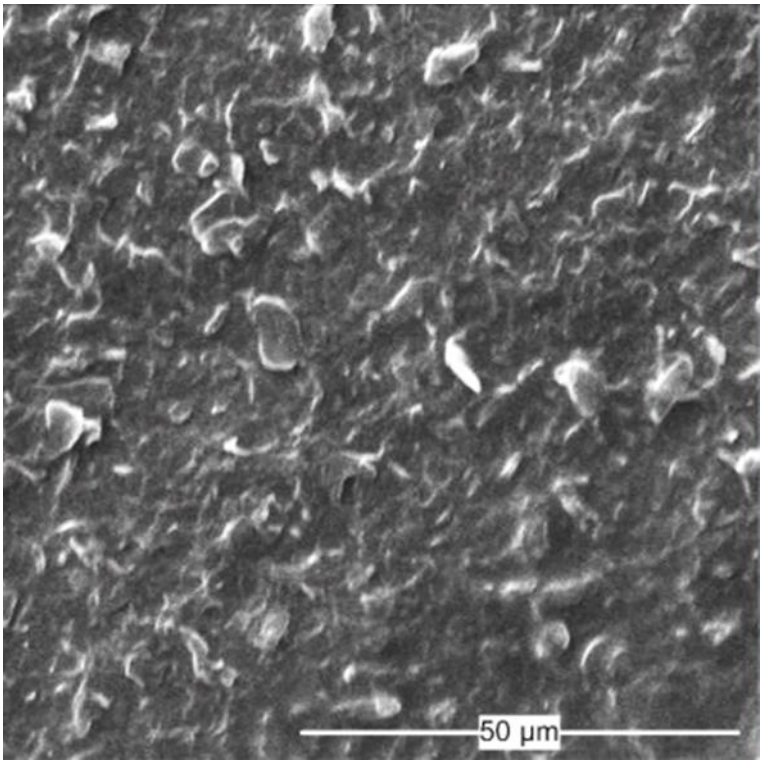


(b)

Fig. 2-3. Porous heating surfaces: (a) SiC, (b) graphene nanoparticles on heating surfaces

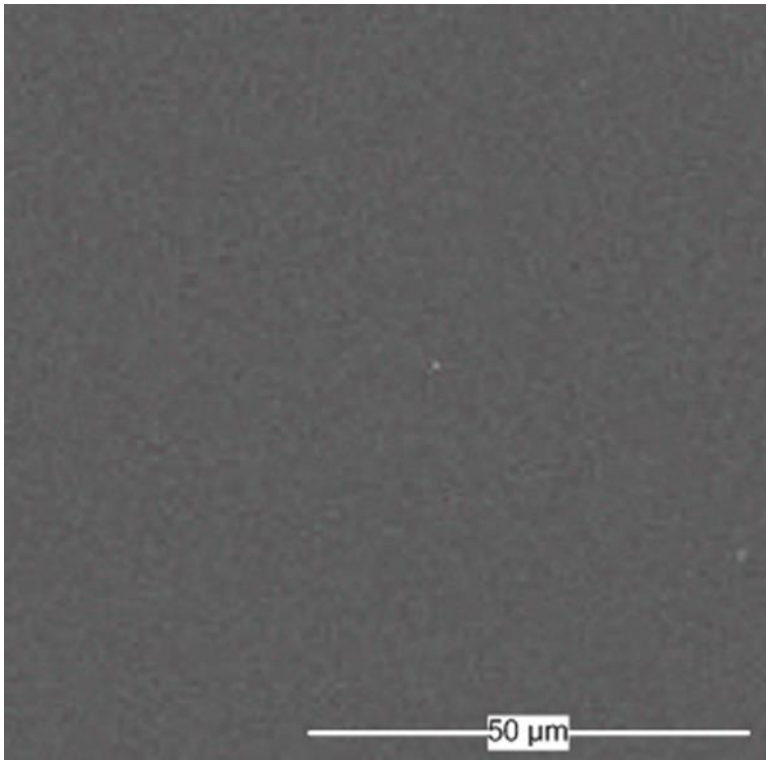


(a)

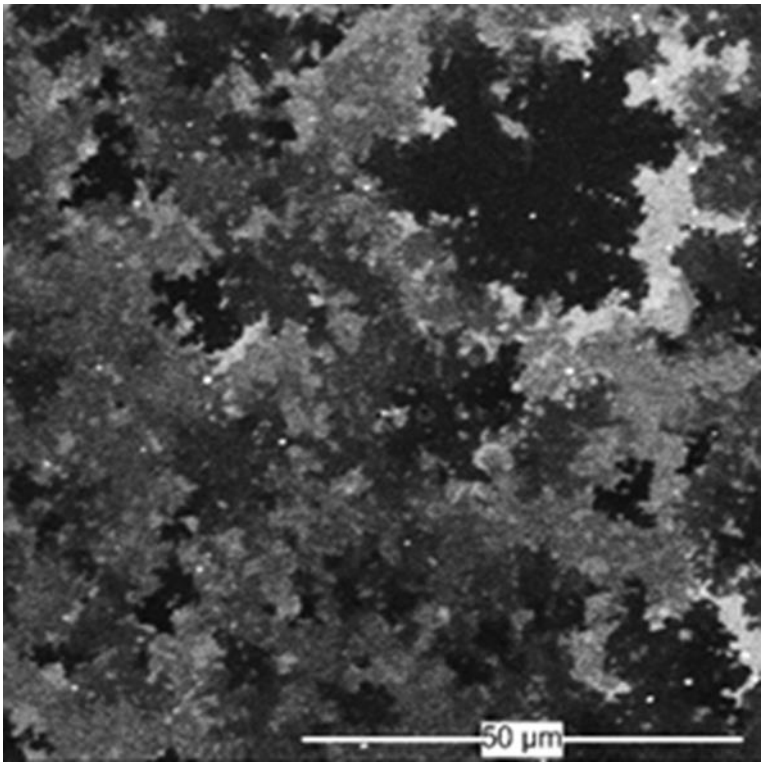


(b)

Fig. 2-4. Nonporous heating surfaces: (a) SiC, (b) graphene (RTA method)

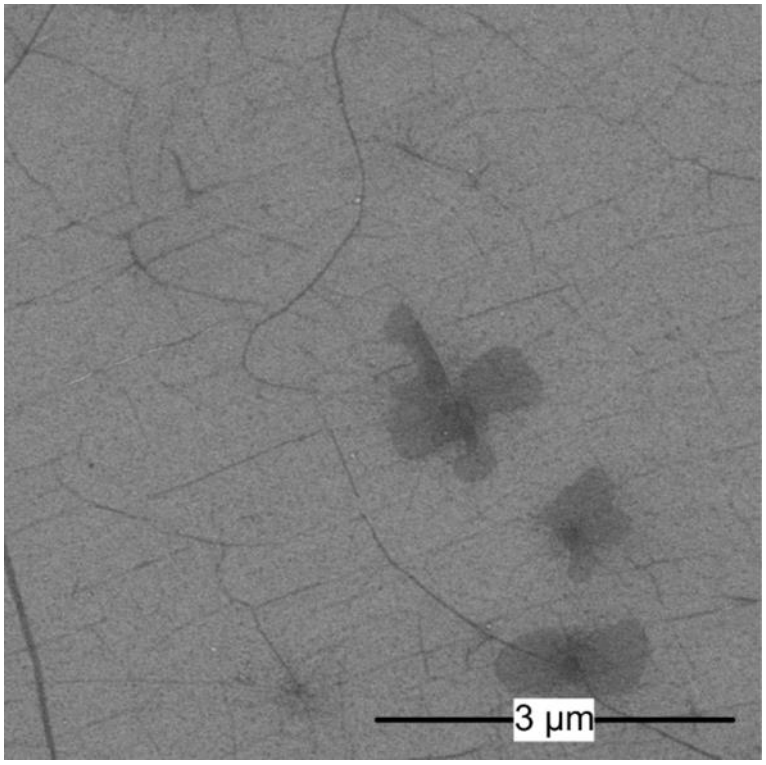


(a)

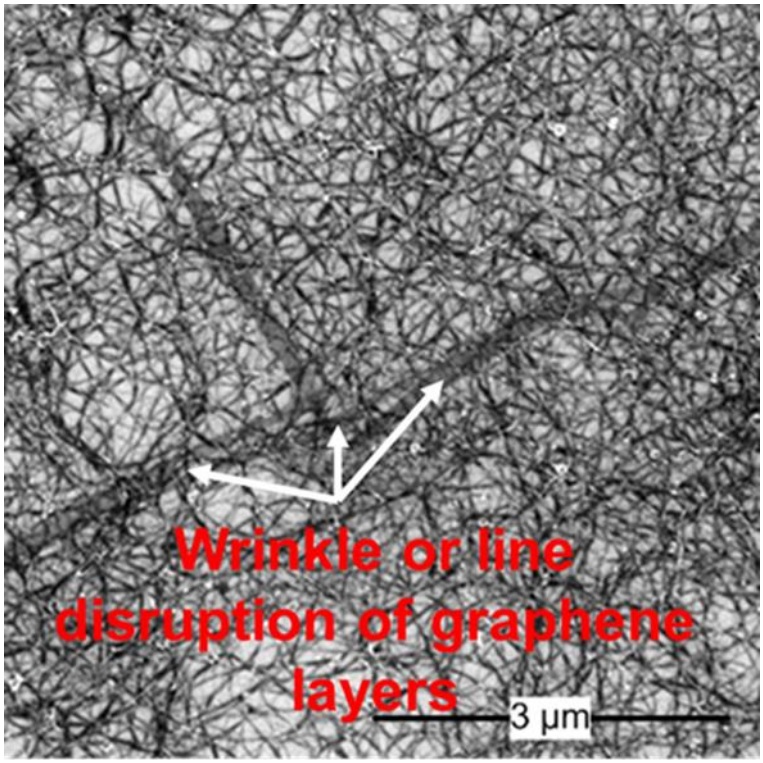


(b)

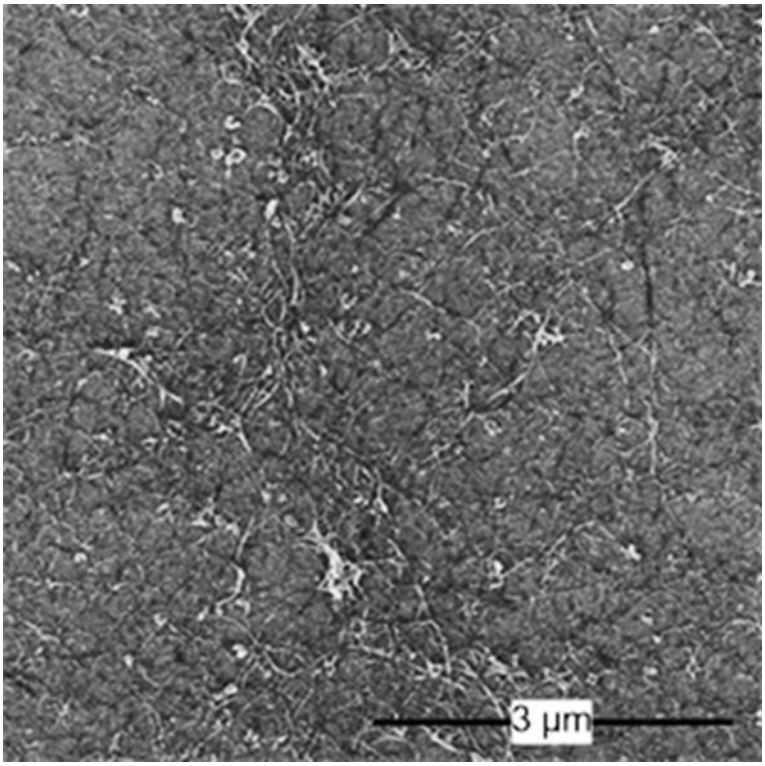


(c)

Fig. 2-5. SEM images of (a) graphene (CVD method), (b) hybrid graphene/SWNCTs, (c) SWCNTs heating surfaces

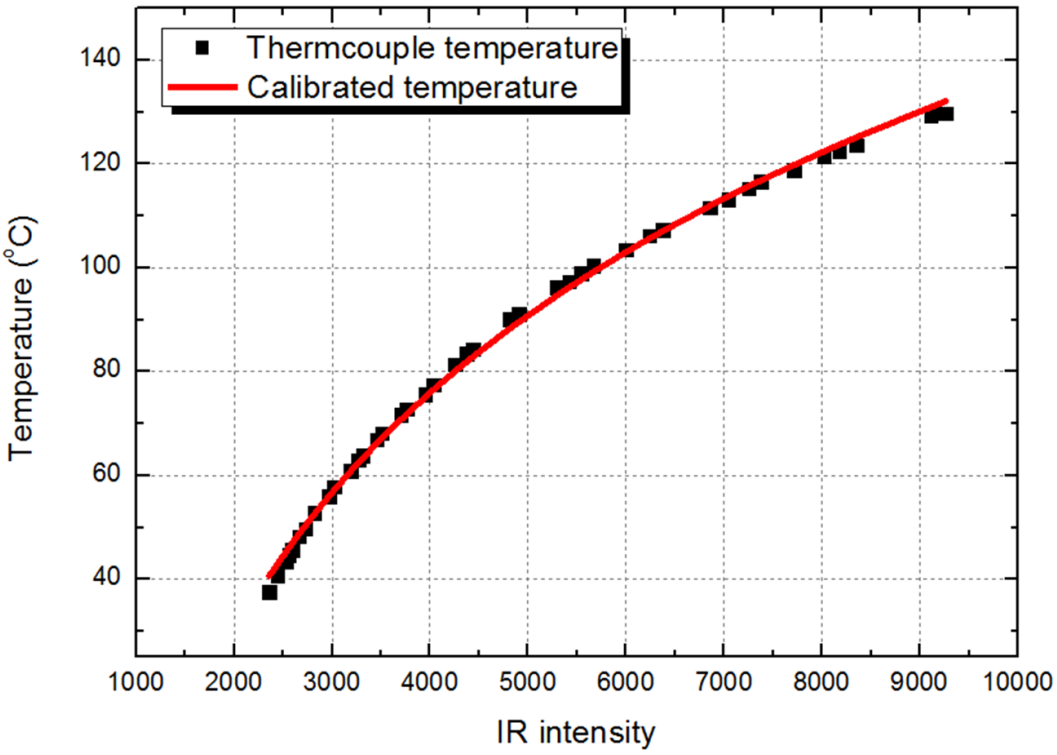


Fig. 2-6. Calibration procedure by matching IR intensity into measured heating surface temperatures

### 2.3 Results and Discussion

In this part, the experimental results of the CHF and BHT were discussed based on the various heating surface characteristics. Various kinds of surface parameters were quantified by several methods and various CHF prediction models, which considered the effects of surface characteristics on CHF performance, were discussed. In addition, the CHF enhancement prediction model that can describe all CHF enhancement mechanisms was suggested based on the experimental results. As a result, modified hydrodynamic instability approach was proposed as the CHF prediction model.

#### 2.3.1 Experimental results

In the pool boiling experiments, the CHF phenomena always appeared with a dramatic increase of the heater wall temperature. The CHF region was defined as the point where the sudden wall temperature increment occurred. If the applied heat flux was not controlled after the CHF, the heater surface will burnout. Fig. 2-7 exhibits the heating surface temperature profile by controlling the applied heat flux. After the CHF point, the vapors, which have much lower heat transfer ability compared to the liquid, covered the whole heating surface. Therefore, it is important to control the heat flux to escape heater burnout phenomena during the experiments.

The CHF tests performed for the bare ITO, porous SiC and graphene, nonporous SiC and graphene, single-layered graphene, hybrid graphene/SWCNTs, and SWCNTs heating surfaces. The CHF results for all coated-surfaces were compared to the bare ITO heating surface for quantification of the CHF enhancement ratios. Table 2-2 lists the CHF results for all heating surfaces. For the bare ITO heating surface, the average CHF value was 120.7 $kW/m^2$. To provide the reliability of the experimental data, the CHF prediction model based on a hydrodynamic instability theory was used. The CHF prediction value with the hydrodynamic instability theory for the FC-72 refrigerant was calculated as 148.15 $kW/m^2$. The obtained CHF value was similar to the hydrodynamic instability CHF model; the CHF result for the bare ITO surface indicated that the experimental procedure in the plate pool boiling facility was valid.

For the porous heating surfaces, the CHF values for the SiC and graphene nanoparticle-coated heating surfaces exhibited 190.7 and 229.2 $kW/m^2$, respectively. Significant CHF enhancement was observed in the porous heating surfaces (58% for SiC-nanoparticle and 89.9% for graphene-nanoparticle coated surfaces, respectively). On the other hand, the nonporous heating surfaces of the SiC and the graphene surfaces did not exhibit significant enhanced CHF performances (139.6 $kW/m^2$ for the nonporous SiC and 131.2 $kW/m^2$ for the nonporous graphene heating surfaces, respectively). The results inferred that the major influence characteristic on the CHF performance between the porous and the nonporous structure was the heating surface deposition characteristics. Boiling curves for the bare ITO and porous

and nonporous surfaces were depicted in Fig. 2-8. The CHF performances for the same heating surfaces showed similar, but there was a fluctuation at the ONB region due to the deposition characteristics for each specimen. The BHT performances for the porous structures also enhanced compared to the bare ITO and the nonporous structures. HTC is a criterion of the heat transfer ability at a certain heat flux, thus maximum HTCs can be regarded as the BHT performances. The maximum HTC for the bare ITO heating surface was measured as 4.335 $kW/m^2K$, while the maximum HTCs for the porous heating surfaces of the SiC and graphene were calculated as 8.825 and 12.92 $kW/m^2K$, respectively. On the other hand, the nonporous heating surfaces for the SiC and graphene showed similar HTC value compared to the bare ITO heating surface (4.739 and 4.517 $kW/m^2K$ for the nonporous SiC and graphene heating surfaces, respectively). Fig. 2-9 exhibits the heating surface temperature fields at various heat flux conditions. As shown in Fig. 2-9, an effective heat transfer was obtained in the porous heating surfaces. Significant enhancement in BHT performances were observed at the porous heating surfaces as well as the CHF results. The results inferred that the boiling performance is also depended on the surface structure characteristics.

The influence of thermal properties on boiling heat transfer test with the hybrid graphene/SWCNTs heating surface was conducted because the hybrid heating surface can improve the thermal conductivity by connecting the wrinkles or the disruption areas of the single-layered graphene surface by dispersing SWCNTs. The CHF values of the graphene, SWCNTs, and hybrid graphene/SWCNTs heating surfaces measured as 130.4, 123.0, and 141.6 $kW/m^2$, respectively. Among the tested heating surfaces, only the hybrid graphene/SWCNTs heating surface achieved the CHF enhancement (17.3 %). In other words, there was no impact on the CHF performance when the graphene and SWCNTs heating surfaces were used. The similar trend was also observed in the graphene surface developed by the RTA method (nonporous graphene heating surface). The result indicated that the superior thermal properties of the graphene were not exhibited on the single-layered graphene heating surface due to the wrinkles or the dislocations. In the hybrid graphene/SWCNTs heating surface, however, the enhanced CHF result would be appeared because the SWCNTs layers connected the disruption lines of the graphene heating surface. Fig. 2-10 exhibits boiling curves for the bare ITO, graphene, SWCNTs, and hybrid graphene/SWCNTs surfaces. As shown in the boiling curves, the BHT performance of the SWCNTs surface was higher than the single-layered graphene surface because the deposition thickness of the SWCNTs was larger than the single-layered graphene surface. Fig. 2-11 shows the temperature fields at different heat fluxes (10, 30, 84, 120, and 135 $kW/m^2$). As Fig. 2-11 indicates, the maximum and average wall superheat of the hybrid graphene/SWCNTs surface were lower than other heating surfaces. This means that the effective heat transfer during the boiling occurrence was observed in the hybrid graphene/SWCNTs surface due to the enhanced thermal heat transport. The highest HTC was measured in the hybrid graphene/SWCNTs surface (6.83 $kW/m^2$), while the maximum HTC for the graphene and the SWCNTs surfaces was obtained as 4.49 and 5.31 $kW/m^2$, respectively.

The experimental results showed that the significant enhanced CHF performance obtained when the heating surface characteristics were changed dramatically from the nano-smooth to the porous structures. In addition, the highly-thermal characteristics of the heating surface can improve the boiling performance based on the hybrid graphene/SWCNTs surface. Based on the experimental results, the investigation of surface parameters to find the CHF enhancement mechanism was conducted. The analysis of the surface parameters was surface wettability, surface roughness, surface capillarity, porosity, permeability, and thermal effusivity.

### 2.3.2 Surface parameter study

Table 2-3 lists the surface parameters that could influence on the CHF performance. For the surface wettability, the parameter could determine the wetting and rewetting zone on the heating surface area by surface-liquid interaction. If the surface reflects hydrophilic characteristic, the working fluid can spread out easily on the heating surfaces at high heat fluxes, compared to the hydrophobic surface. Most of the CHF enhancement studies argued that the change of surface wettability has been considered as the main parameter on the CHF performance. However, there were contradictory reported results that the significant CHF results can be obtained even though surface wettability was not improved or deteriorated[11]. In the present study, hydrophilic characteristics for all heating surfaces appeared because FC-72 refrigerant, which has lower surface tension (0.01 N/m) compared to water (0.0589 N/m), used as the working fluid. To support the hydrophilic characteristics for all heating surfaces, static contact angle measurements were performed. All heating surfaces showed hydrophilic characteristics: 14.3° for the bare ITO, 14.0° for the porous SiC, 13.5° for the porous graphene, 11.7° for the nonporous SiC, 13.6° for the nonporous graphene, 11.8° for the single-layered graphene, 12.1° for the SWCNTs, and 13.9° for the hybrid graphene/SWCNTs heating surfaces, respectively. Because static contact angles for all heating surfaces were ranged from 11° to 14°, the effect of surface wettability can be suppressed. Therefore, the ambiguous surface wettability parameter was not considered in the present experiments.

For the capillarity, this parameter influences on liquid supply to dry patch on the heating surface that could escape to cause the heater surface temperature excursion. The surface capillarity can be quantified by the measurement of capillary height or length. Several studies have evaluated the capillarity by the liquid adsorption on the heating surfaces[11, 31-32]. The previous studies indicated that the trend of the capillarity can support the CHF enhancement. In the present study, therefore, similar capillarity observation was conducted on the porous heating surfaces because nonporous heating surfaces could not provide any liquid path into the heating structures. The porous heating surfaces were cut by the low speed saw for the capillarity measurement. Because the FC-72 has low latent heat (88 kJ/kg) in comparison with water (2257 kJ/kg), the capillary wicking measurement was conducted at low temperature (~0 $^{o}$C). Fig. 2-12 shows the results of the capillary measurements. As shown in Fig. 2-12,

there was no difference between the porous SiC and graphene surfaces due to the low surface tension of the working fluid. This means that porous heating surfaces did not exhibit any capillarity, thus the effect of the capillarity was not also considered as the surface parameter that influences on the boiling performance.

The surface roughness parameter also considered as one of the main surface parameter in the CHF performance. When the surface roughness was created on heating surfaces, activation nucleation sites and boiling center can be created. This could bring the change of the CHF and BHT. In addition, the surface roughness affects to the surface wettability, but the effect of surface wettability through the change of surface roughness was not included in the present study. The surface roughness can be quantified by the measurement surface vertical deviation. The atomic force microscopy (AFM) was used to measure the surface roughness parameters. Fig. 2-13 shows the AFM images for all heating surfaces. As surface roughness parameters, the arithmetic average of the surface height deviation ($R_a$) and the root mean square ($R_q$) values were considered. Compared to the bare ITO and nonporous heating surfaces, higher values of the $R_a$ and $R_q$ were observed in the porous heating surfaces. The porous graphene and SiC heating surfaces could be differentiated from the bare ITO and nonporous heating surfaces which showed nanosmooth heating surfaces. This means that the surface roughness may influence on the boiling performance in the present experiments.

Porosity and the permeability parameters are related to the ability of the liquid transport into the porous heating surfaces. Therefore, the porous SiC and graphene heating surfaces were examined to quantify the porosity and the permeability. When the porous structures are created on the heater, the change of nucleation site density can be appeared. The surface porosity also provides the liquid transport space between the nucleate sites with the inner structure of the heating surface that can endure high heat fluxes compared to the plain heating surface. Fig. 2-14 is detailed surface structures. As Fig. 2-14 depicts, the characterization of the surface fields was possible, but the quantification of the porosity measurement through the SEM images was difficult because these images did not provide inner surface characteristics. To measure the porosity of the porous heating surfaces, mercury porosimetry was used. The mercury has hydrophobic that brings non-wetting characteristics on the heating samples. In other words, the mercury can be supplied into the porous structures when the system pressure changes. This enables the measurement of the size distribution of the pores and cavities of the structure as well as the porosity. The Washburn equation was used to calculate the pore sizes as a function of the applied system pressure.

$$r = -\frac{2\sigma\cos\theta}{P} \qquad (2\text{-}2)$$

where r is the pore radius, $\sigma$ is the surface tension of mercury, $\theta$ is the liquid-surface contact angle of mercury, and P is the applied pressure to the sample. The system pressure was varied from the

atmospheric pressure to 4081 bars, thus the pore sizes ranged from 3.6 nm to 950 μm were considered into the porosity estimation. Based on the porosity estimation, the porosities of the porous SiC and graphene surfaces were ~3.75% and ~13.1%, respectively. The trend of the CHF performance was similar to the porosity measurement results; the CHF of the porous graphene heating surface was higher than the porous SiC heating surface. Therefore, the surface parameter of the porosity may influence on the CHF performance and several studies related to the deposition characteristics of the nanoparticles supported the present experimental results[11, 33].

The permeability is a criterion of the ability for vapors or fluids to flow into the heating surface structure based on the pore properties. The permeability parameter can be quantified by the effective area in the porous structure. The permeability is related to the porosity . This means that the permeability of the porous graphene would be higher than the porous SiC heating surfaces. To quantify the permeability of the porous structures, the permeability measurement was conducted. The measurement tests with the heating surfaces that were used in the boiling experiments were difficult because there was no penetration path in the heating surfaces. Instead of using the heater samples, stainless steel plate with diameter and thickness of 25 and 1 mm, was used. There was a 1-mm-diameter hole at the center of the specimens to deposit the nanoparticles for the permeability test. The deposition of the nanoparticles on the samples was conducted in the hot plate. Fig. 2-15 shows the test samples and SEM images of the test samples. The permeability measurements were conducted based on the test samples and the permeability was calculated from Darcy's law, which describe a fluid flow kinetics through the porous structures.

$$K = \frac{Q}{A}\frac{\mu}{\Delta P}l \qquad (2\text{-}3)$$

where Q is the volumetric flow rate through the porous structure, μ is the viscosity, l is the flow length or thickness of the test sample, A is the cross-sectional flow area, and ΔP is the pressure drop through the porous structure. The measurement results indicated that the average permeabilities of the porous SiC and graphene heating surfaces were $2.0129\times10^{-11}$ and $2.060\times10^{-10}$ $m^2$, respectively. The permeability of the porous graphene heating surface was higher than that of the porous SiC heating surface, as was the porosity. Therefore, higher permeability brings the liquid penetration into the heating structures; this characteristic may bring the change of the CHF performance.

The material properties can also influence on the CHF performance[34-35]. One of the material parameter that has been used in the CHF enhancement mechanism studies is the thermal effusivity. Thermal effusivity has considered as the CHF and BHT enhancement mechanism because it contains the thermal conductivity, density, and heat capacity of the heating surfaces. The heat dissipation phenomenon at high heat flux regions could be explained by the thermal effusivity. This parameter is the rate at which

a certain material could absorb and transfer the heat to the surroundings. Higher thermal effusivity material can deliver more heat to the heating surface surrounding or the working fluid. At the high heat flux close to the CHF, there would be higher temperature regions that may cause the CHF due to the low heat transfer ability on that point. By using the heat material that reflects higher thermal effusivity, effective heat dissipation on the heating surface appeared and it can delay the hot/dry spot formation that causes the CHF. This means that the CHF and BHT performances could be enhanced due to the change of thermal properties of heating surfaces. The thermal effusivity parameter is given by

$$E = \sqrt{\rho_h c_h k_h}\ , \qquad (2\text{-}4)$$

where $\rho_h$, $c_h$, and $k_h$ are the heater material density, specific heat, and thermal conductivity, respectively. The higher effusivity heating material can increase the amount of the phase change of the fluid from liquid to vapor[36-37]. In addition, there was a correlation related to the HTC performance based on the thermal effusivity at the nucleate boiling regions with various working fluids [38]. This means that the HTC can be enhanced when the heating material properties are improved. Fig. 2-16 shows an illustration related to the thermal heat transport phenomena on the single-layered graphene and hybrid graphene/SWNCTs heating surfaces. For the hybrid graphene/SWCNTs heating surface, the result indicated that the CHF and HTC performances were higher than compared to the bare ITO, single-layered graphene, and SWCNTs heating surfaces. The main purpose of the hybrid heating surface was to connect the wrinkles or dislocation lines of the graphene layer with the SWCNTs for maximizing thermal properties of carbon structures. The main heat dissipation parameter in the thermal effusivity is the thermal conductivity. Therefore, the enhanced CHF and HTC appeared on the hybrid graphene/SWNCT heating surface.

Major surface parameters that could influence on the CHF performance were analyzed based on the experimental results. The independent evaluations of surface parameters were impossible because the surface parameters are linked each other. For example, the surface roughness is linked to the surface wettability because the static contact angle can be changed based on modified Young's equation, which considered the surface roughness into the surface wettability. In addition, the porosity and the permeability could not stand for the CHF enhancement parameters independently. It is hard to demonstrate the effects of each surface parameter because most of parameters are connected. Instead, there are many efforts to prove the CHF enhancement mechanism based on CHF prediction models. Various kinds of CHF prediction models were introduced and following CHF enhancement mechanisms based on the experimental results were discussed in the next part.

### 2.3.3 Comparison between CHF results and CHF prediction models

There are many efforts on developing CHF prediction models because the precise CHF prediction is related to the safety of industries including nuclear power plants. If the accurate CHF prediction model related to the nuclear power plants is developed, the margin for the departure nucleate boiling ratio (DNBR) will be controlled. In addition, nuclear power density and safety margins can be increased with the exact CHF prediction model. Several kinds of CHF models will be introduced to predict the CHF results measured in the pool boiling experiments.

The hydrodynamic instability theory for the CHF prediction has been widely used in various industrial and research fields because the model can predict the CHF performance when a plain heating is used. The hydrodynamic instability theory explains the CHF phenomenon by the critical vapor velocity. When the velocity of vapor reaches critical state at the CHF region, the downflow of a liquid to the heated surface is prevented by the vapor generation. The CHF model can be obtained as

$$q''_{CHF} = \frac{\pi}{24}\rho_v^{1/2} h_{lv} \sqrt[4]{\sigma g\left(\rho_l - \rho_v\right)} \qquad (2\text{-}5)$$

where $\rho_l$, $\rho_v$, $h_{lv}$, $\sigma$ are the liquid density, vapor density, latent heat, and surface tension, respectively. The predicted CHF value could be varied if the effect of heating surface characteristics were considered in the Zuber's model. To compensate for the surface effects on the CHF model, Liter and Kaviany[9] proposed a modulation wavelength that reflected the effect of CHF performance by changing the surface from the plain to the porous structures. Liter and Kaviany[9] insisted that the RT instability can be determined by the porous structures: the RT instability wavelength can be determined by a geometrically conditions. Following relations were considered into the hydrodynamic instability theory.

$$\lambda_{KH} = 2\pi a \lambda_m = 9a\lambda_{RT,c} \qquad (2\text{-}6)$$

$$\frac{q''_{CHF,h}}{(\pi/24) h_{lv}\rho_v^{1/2}\sqrt[4]{\sigma g\left(\rho_l - \rho_v\right)}} = \frac{3\sqrt[4]{\sigma / g\left(\rho_l - \rho_v\right)}}{\lambda_m^{1/2}} \qquad (2\text{-}7)$$

$$q''_{CHF,h} = \frac{\pi}{8} h_{lv}\left(\frac{\sigma\rho_v}{\lambda_m}\right)^{1/2} \qquad (2\text{-}8)$$

where a, $\lambda_{KH}$, and $\lambda_m$ are the constant, Kelvin–Helmholtz (KH) instability wavelength, and modulation wavelength determined by the heater geometry. The measurement of the modulation wavelength in the present experimental works (porous SiC and graphene heating surfaces) is difficult because the

deposition of the nanoparticles on the bare ITO heating surface was irregular because boiling-induced depositions were conducted. There is a prediction model for the modulation wavelength that can be derived as

$$\lambda_m = \left( \frac{\pi}{5.88\varepsilon^{2.28}} \right)^2 d \qquad (2\text{-}9)$$

where ε and d are the porosity of the structure and the pore particle size. The measurement of the pore particle size for the porous SiC heating surface can be estimated by the SEM images (Figs. 2-3 and 2-14). The SiC nanoparticles agglomerated onto the spherical shape during the deposition process with an average size of 230 nm. However, the measurement of the pore size for the porous graphene heating surface was not conducted because the deposition of the porous graphene had a plate shape, as shown in Figs. 2-3 and 2-14. The porosity for the porous SiC heating surface was measured from the mercury porosimetry (~ 3.75%), thus the estimation of the modulation is possible. When the porosity data for the porous SiC heating surface was considered in the model, there was a large discrepancy between the measured CHF result and the predicted CHF value, possibly because the pore size in the prediction model did not cover the nano-scale of the pore structure. This means that the models seemed to be limited in the micro- or millmiter-scale of the pore size. But there have been CHF enhancement mechanism studies related to the change of the RT instability wavelengths.

The balance between the capillary pumping force and the liquid viscous drag along its flow path can be used to predict the CHF due to the capillary pumping limit[9,39].

$$\frac{q_{CHF,c}}{0.53(\rho_l \sigma h_{lv} / \mu_l)(K\varphi_s)^{1/2} / D)} = 1 - \frac{C_E}{0.53} \frac{D}{\sqrt{\varphi_s}} \frac{q_{CHF,C}^{\ 2}}{\rho_l \sigma h_{lv}^{\ 2}} \qquad (2\text{-}10)$$

$$C_E = (0.018 / \varphi_s)^{1/2} \qquad (2\text{-}11)$$

where $\mu_l$ is the viscosity of the liquid, K is the permeability of the wicking structure, $C_E$ is the Ergun coefficient, D is the liquid flow distance, and $\varphi_s$ is the porosity of the surface subarray. For the porous SiC surface, the liquid flow distance D was ~7.9 μm, the structural porosity $\varphi_s$ was ~0.0375, and the permeability K was ~$2.0129\times10^{-11}$ $m^2$. For the porous graphene heating surface, the liquid flow distance D was ~3.4 μm, the structural porosity $\varphi_s$ was ~0.0131, and the permeability K was ~$2.060\times10^{-10}$ $m^2$. The values of $q_{chf,c}$ given by eq. (2-10) for the porous SiC and porous graphene heating surfaces are approximately 8983 kW/$m^2$ and 48,920 kW/$m^2$, respectively. A sensitivity analysis of the permeability and porosity, which influence on the capillary pumping limits, was conducted. As Fig. 2-17(a) shows, the permeability, which ranged from $10^{-16}$ to $10^{-10}$, changes the CHF exponentially. The porosity, on the

other hand, changes the CHF linearly, as shown in Fig. 2-17(b). Therefore, careful measurement of the permeability, taking into consideration the pore size, porosity, and working fluid, is needed.

There is a CHF theory related to the dryout of a liquid macrolayer on a heating surface, called as macrolayer dryout theory. This approach assumed that the CHF appeared when hovering time of large mushroom-shaped bubbles on the heating surface is relative larger than a departing period[40]. The macrolayer dryout can be calculated as

$$q''_{CHF} = \frac{\delta_e \rho_l h_{lg}}{\tau_d} \qquad (2\text{-}12)$$

where $\delta_e$ and $\tau_d$ are the equivalent thickness of the macrolayer and the time to dry out the macrolayer liquid film, respectively. The CHF for the macrolayer dryout model is determined when the hovering time of vapor clot or vapor mushroom ($\tau_h$) is longer than the time to dryout. Sadasivan et al.[40] estimated the equivalent thickness of liquid layer that contains the effect of surface wettability. The equivalent thickness of macrolayer can be estimated as

$$\delta_e = r_b \left[ \cos\theta - \frac{\pi}{12}\left(3\cos\theta - \cos^3\theta\right) \right] \qquad (2\text{-}13)$$

where $r_b$, and $\theta$ are the bubble radius, and the contact angle, respectively. When the heating surface exhibited hydrophilic conditions, the equivalent thickness of liquid will be increased which bring the enhanced CHF performance. In the present work, however, the increased equivalent thickness of liquid could not be considered because the highly-wetting fluid (FC-72 refrigerant) was used as the working fluid. Instead of the effect of surface wettability, the additional possible of increasing the equivalent thickness of liquid layer was proposed by the effects of porous structures on heating surfaces[11].

$$\delta_{total} = \delta_e + \varepsilon\delta_p \qquad (2\text{-}14)$$

where $\delta_p$ is the increment of equivalent thickness of liquid layer due to the porous structures. Total thickness of the equivalent liquid layer indicated that the CHF enhancement would be illustrated by the effect of surface wettability and porous structures. In the present study, the additional equivalent thickness of the liquid layer for the porous heating surfaces supported the CHF enhancement, but detailed quantification by using the increment of the liquid layer is difficult because the calculated of the equivalent thickness of microlayer for the porous heating surfaces was similar to the bare ITO

heating surface: 103.3, 103.6, and 103.7 μm for the bare ITO, porous SiC, and porous graphene heating surfaces.

Bubble interaction theory describes that the CHF is postulated by bubbles coalescence because of a large number of bubbles and departure frequency at high heat fluxes[41]. The correlation related to the bubble interaction was presented by shear force effect generated by the interaction of the growing and departing bubbles on heating surfaces. According to Kolev's model[42], the boiling performance from the nucleate boiling region and the CHF region can be predicted and expressed as

$$q'' \propto N_A^{1/4} \Delta T^2 \left(1 + 0.3 \frac{\Delta \tau_w}{\Delta \tau_d}\right)^{-1/2} \qquad (2\text{-}15)$$

where $N_A$, $\Delta T$, $\tau_w$, and $\tau_d$ are nucleate site density, wall superheat, bubble wait time, and bubble departure time, respectively. In the bubble interaction model, the parameters of nucleate site density and bubble wait and departure time are strongly influenced by the surface wettability. Example of boiling curves based on the bubble interaction theory is described in Fig. 2-18. As Fig. 2-18 exhibits, the CHF is increased as the surface wettability changes to hydrophilic, while the HTC at the nucleate boiling region is deteriorated. The surface wettability is the major parameter that influences on the CHF performance in the bubble interaction theory. If the surface characteristics are considered into the Kolev's model, the enhancement CHF mechanism could be improved.

When the heat flux is close to the CHF, hot/dry spots are appeared on the heating surfaces during bubble growth and departure period. The hot/dry spot could be appeared as reversible or irreversible. The theory of the hot/dry spot model is that CHF occurs when the irreversible hot spots are created and these irreversible hot spots bring temperature excursion[43-44]. Microhydrodynamics of the solid-liquid-vapor line at the boundary of a hot/dry spot was presented[45].

$$q''_{CHF} = k^{-1/2} \rho_v^{1/2} h_{lv} \sqrt[4]{\sigma g (\rho_l - \rho_v)} \sqrt{\frac{\rho_l + \rho_v}{\rho_l}} \qquad (2\text{-}16)$$

Interestingly, the equation of the hot/dry spot and the hydrodynamic instability theory equation are almost same except for the parameter k. The parameter of k is depended on the heater surface characteristics. Bang et al.[46] obtained temperature distributions of heating surfaces with base fluid and $Al_2O_3$ nanofluid. They used IR thermometry to measure temperature fields of all heating surfaces with various conditions. Fig. 2-19 shows series of the IR images in the base fluid and the nanofluid at the CHF region. As shown in Fig. 2-19, differences in the behavior of the nanofluids were confirmed by the IR thermometry: presence of several non-expanding hot spots, cold spots distribution, cold spots

around the main hot spot, and cyclic behaviors of hot spot expansion[46]. The same phenomenon was observed in the experimental results, especially for the porous structures and the hybrid graphene/SWCNTs heating surface (Figs. 2-9 and 2-11). The results also indicated that the hot spots are separated until CHF occurred. These results supported the mechanisms of the hot/dry spot model that CHF can be enhanced when the hot spots are not gathered and irreversible hot spots are suppressed. The present experiments of the porous heating surfaces supported the hot/dry spot model, but detail description is difficult because the hot/dry spot model is depended on the boiling observation. Recently, measurements of dry spots using high-speed and high-resolution devices in plate pool boiling conditions to determine the CHF triggering mechanism. Chu et al.[47] visualized the liquid-vapor phase distributions on a heating surface at various heat flux conditions including the CHF region. Measurements of residual dry patches were conducted to find the triggering mechanisms of the CHF. However, the experimental data were limited to find the CHF mechanisms because thermal behavior on the heating surfaces was not conducted. Kim et al.[48] measured the dry fraction area including irreversible dry spot at CHF in pool boiling. The measurement of temperature distribution and phase distributions was conducted through a IR thermometry. They presented a conceptual boiling curve that time average heat flux is the form of the ratio of the nucleate boiling and film boiling heat fluxes. However, it was also difficult to find the precise CHF triggering mechanisms through the dry spot formations. In addition, plate pool boiling experimental facility with synchronized total reflection technique (high-speed camera) and the IR thermometry was used to found the CHF mechanism based on the irreversible dry patch with the temperature distributions with triple-contact-line[49]. The visualization of the boiling measurement and temperature distribution on a heating surface was conducted. They inferred that the CHF triggering mechanism should consider the dynamics of the dry patch and the thermal behavior.

Bubble force balance between momentum changes due to bubble evaporation was proposed by Kandlikar[50]. He proposed the momentum change that was the balance of the surface force at the bottom and the top of the bubble and the gravity force. The model assumed that the heat flux on the heater surface is obtained by the heat transfer rates over the influence area and over the interface area of the average bubble diameter[50]. The bubble diameter was obtained by assuming the half of the RT instability wavelength. The bubble force balance model for the CHF prediction can be calculated as

$$q''_{CHF} = h_{lv}\rho_v^{1/2}\left(\frac{1+\cos\beta}{16}\right)\left[\sigma g\left(\rho_l-\rho_v\right)\right]^{1/4}\left[\frac{2}{\pi}+\frac{\pi}{4}\left(1+\cos\beta\right)\cos\varphi\right]^{1/2} \qquad (2\text{-}17)$$

where β and φ are the bubble receding angle and the heater inclination angle, respectively. The equation indicated that the CHF are varied with the surface wettability. Most of nanofluids studies showed that the CHF improvement can be determined by the surface wettability except for some cases such as Park

et al.[10] and Maeng et al.[51]. However, when the surface showed superhydrophilic which contact angle reached 0°, it is difficult to predict the CHF trends. Ahn et al.[32] showed that the Kandlikar's model could not predict the CHF trend when the nano/microstructures were used.

$$q''_{CHF} = q''_{Kandlikar} + \frac{\varepsilon\delta\rho_l h_{lv} K}{A_{heat}} \frac{\overline{dA_w}}{dt} \qquad (2\text{-}18)$$

where ε, δ, and $A_w$ area the porosity and thickness of the structure and the area wetted by capillary wicking, respectively. Additional consideration of spreading effect was included in the Kandlikar's model. On the other hand, additional parameter on the momentum balance was considered into the Kandlikar's model to analyze the CHF performance with the surface roughness which reflects the ratio of actual heating surface area and projected heating surface area. Quan et al.[52] considered capillary wicking phenomenon created by the surface roughness which can predict the CHF trend based on the surface wettability and the surface roughness.

$$q''_{CHF} = Kh_{lv}\rho_v^{1/2}\left[\sigma g\left(\rho_l - \rho_v\right)\right]^{1/4}$$

$$K = \left(\frac{1+\cos\beta}{16}\right)\left[\frac{2}{\pi}\left(1-\sqrt{\phi_s}\right)^{-1/2}\frac{r+\cos\beta}{1+\cos\beta} + \frac{\pi}{4}\left(1+\cos\beta\right)\cos\varphi\right]^{1/2} \qquad (2\text{-}19)$$

where Φs and r are the solid fraction of the heating surface and the surface roughness, respectively. The model can predict the CHF based on the surface wettability, the surface roughness, or the solid fraction. In addition, additional force term was considered into the bubble force balance[53]. Instead of using surface roughness (actual surface area/projected surface area), the average roughness value ($R_a$) of the heating surfaces obtained by the measurement device. They considered the capillary wicking term in the balance equation and the Ra and the mean spacing of the surface roughness ($S_m$) were considered.

$$q''_{CHF} = Sh_{lv}\rho_v^{1/2}\left[\sigma g\left(\rho_l - \rho_v\right)\right]^{1/4}\left(\frac{1+\cos\beta}{16}\right)\left[\frac{2}{\pi} + \frac{\pi}{4}\left(1+\cos\beta\right)\cos\varphi + \frac{4C\cos\beta}{1+\cos\beta}\left(\frac{R_a}{S_m}\right)\right]^{1/2} \qquad (2\text{-}20)$$

where S and C are the correlation factor for the CHF prediction model. However, these CHF models related to the bubble force balance models are limited to their experimental results. In the present experiments, the main objective was to obtain the CHF enhancement without surface wettability and capillary improvements. This inferred that the bubble force balance model cannot be considered as the

CHF enhancement mechanism.

Table 2-4 lists the evaluation of various CHF models. Various CHF prediction models are introduced and evaluated by the experimental results. The explanation of the CHF enhancement for the porous surfaces and the hybrid graphene/SWCNTs was possible based on several CHF models, but it was difficult to quantify the CHF enhancement ratio. To deal with the problem, the new approach of the CHF enhancement mechanism model based on the hydrodynamic instability theory is proposed in the present study. The classical hydrodynamic instability did not consider the effects of surface characteristics. This indicates that the CHF mechanism model based on the hydrodynamic instability theory can be improved by considering heating surface characteristics. Park et al.[10] and Lee et al.[54] used the hydrodynamic approach on their experimental results and showed that RT instability wavelength measurements through condensation methods can predict the CHF enhancement mechanism. In addition, Park and Bang[11] correlated their measurement RT instability wavelengths and CHF results to explain the CHF enhancement mechanism based on the hydrodynamic instability approach. Fig. 2-20 shows the results of the RT instability measurement results provided by Park and Bang[11]. But the experimental correlation is not suitable because the measurement of the RT instability wavelengths was conducted in R-123 refrigerant, while the CHF enhancement data were measured in water as the working fluid. This means that additional experiment studies should be performed to develop the CHF model based on the hydrodynamic instability approach. Therefore, a revisiting study to find the relation between the RT instability wavelength and the CHF values under various experimental conditions was performed. In addition, surface patterning studies to evaluate the RT instability wavelengths in plate pool boiling were performed. These experimental studies will be described in the chapter 3. Based on the experimental works related to the hydrodynamic instability theory, the modified hydrodynamic instability theory model that consider the effect of surface characteristics is proposed in the chapter 4 and the validation of the proposed model is performed based on the existed experimental results.

Table 2-2. CHF results and enhancement ratio according to various heating surfaces

| Heater | CHF ($kW/m^2$) | Enhancement ratio (%) |
|---|---|---|
| Bare ITO | 120.7 | - |
| Porous SiC | 190.7 | 58.0 |
| Porous graphene | 229.2 | 89.9 |
| Nonporous SiC | 139.6 | 15.7 |
| Nonporous graphene (RTA) | 131.2 | 8.69 |
| Single-layered graphene (CVD) | 130.5 | 8.12 |
| SWCNTs | 123.0 | 1.91 |
| Graphene/SWCNTs | 141.6 | 17.3 |

Table 2-3. CHF mechanisms based on surface characteristics

| Surface Parameters | Characteristics (Effects) | Quantification |
|---|---|---|
| Wettability | • Wetting and rewetting zone on the heating surface<br>• Surface–liquid interaction | Contact angle |
| Capillarity | • Liquid supply to dry patch on the heating surface induced by capillary action | Capillary height or length |
| Roughness | • Active nucleation sites<br>• Active boiling center<br>• Influence on wettability | Surface's vertical deviation |
| Porosity | • Nucleate site density<br>• Role of transport liquid between nucleate sites<br>• Additional thermal resistance | Void fraction |
| Permeability | • Criterion of the ability for vapors or fluids to flow into the surface structure based on pore properties | Effective area |
| Thermal Effusivity | • Measures the rate of heat absorption<br>• Higher effusivity heating material can increase the amount of the phase change of the fluid from liquid to vapor. | Thermal effusivity |

Table 2-4. Evaluation of various CHF models

| CHF Theory | | Description | Prediction eq. | Major parameters |
|---|---|---|---|---|
| Hydrodynamic Instability | Zuber (1959)<br>(Infinite heating surface) | ✓ Velocity in the vapor jets issuing from the surface reaches a critical velocity<br>✓ Critical velocity is the velocity at which vapor jets become Kelvin-Helmholtz unstable | $q''_{CHF} = \frac{\pi}{24}\rho_v^{1/2} h_{lv} \sqrt[4]{\sigma g(\rho_l - \rho_v)}$ | ✓ Critical vapor velocity<br>✓ KH & RT instability wavelengths |
| | Lienhard and Dhir (1973)<br>(Heating surface effect) | ✓ Extend the hydrodynamic instability theory in finite heating surfaces | $\frac{q''_{CHF}}{q''_{CHF,Z}} = f(L')$ | ✓ Heater size effects<br>✓ RT instability wavelength |
| | Liter and Kaviany (2001)<br>(Porous heating surface) | ✓ Modulation wavelength based on deposition of particles on heating surfaces | $q''_{CHF} = q''_{CHF,Z} \times \left(\frac{9}{2\pi}\frac{\lambda_{RT,c}}{\lambda_m}\right)^{1/2} = \frac{\pi}{8} h_{lv}\left(\frac{\sigma\rho_v}{\lambda_m}\right)^{1/2}$ | ✓ Modulation wavelength |
| | Lee and Lee (2014)<br>(Narrow slit) | ✓ Prediction and measurement of RT instability wavelength and critical vapor velocity | $q''_{CHF} = 1.383\eta(w' f(w'))^{-1/4} q''_{CHF,Z}$ | ✓ RT instability wavelength<br>✓ Critical bubble velocity |
| Macrolayer Dryout | Hamura and Katto (1983) | ✓ A thin liquid film including vapor stems is left stable on the surface with a certain thickness<br>✓ Disappearance of liquid film during a hovering period | $q''_{CHF} = \frac{\delta_e \rho_l h_{lv}}{\tau_d}\frac{A_h - A_v}{A_h}$ | ✓ KH instability wavelength |
| | Sadasivan et al. (1992) | ✓ Propose an equivalent liquid thickness of microlayer | $q''_{CHF} = \frac{\delta_e \rho_l h_{lv}}{\tau_d}\ \delta_e = r_b\left[\cos\theta - \frac{\pi}{12}(3\cos\theta - \cos^3\theta)\right]$ | ✓ Equivalent thickness<br>✓ Surface wettability |
| Bubble force balance | Kandlikar (2001) | ✓ Balance of the surface force at the bottom and the top of the bubble and the gravity force | $q''_{CHF} = q''_{CHF,Z}\frac{24}{\pi}\left(\frac{1+\cos\beta}{16}\right)\left[\frac{2}{\pi} + \frac{\pi}{4}(1+\cos\beta)\cos\phi\right]^{1/2}$ | ✓ Surface wettability<br>✓ RT instability wavelength |
| | Quan et al. (2014) | ✓ Solid fraction was considered in RT instability wavelength<br>✓ Surface roughness was considered in bubble force balance | $q''_{CHF} = q''_{CHF,Z}\frac{24}{\pi}\left(\frac{1+\cos\beta}{16}\right) \times \left[\frac{2}{\pi}\left(1-\sqrt{\phi_s}\right)^{-1/2}\frac{r+\cos\beta}{1+\cos\beta} + \frac{\pi}{4}\left(1-\sqrt{\phi_s}\right)^{1/2}(1+\cos\beta)\cos\phi\right]^{1/2}$ | ✓ Surface wettability<br>✓ Roughness<br>✓ Solid fraction |
| Bubble Interaction | Rohsenow and Griffith (1955) | ✓ Bubbles coalescence because of a large number of bubbles and departure frequency at high heat fluxes<br>✓ Irreversible bubble formation | $q''_{CHF} = \frac{\pi}{6} C_q C_{vb}(fD_b)\rho_v h_{lv}$ | ✓ Bubble departure diameter<br>✓ Frequency |
| | Kolev (1994) | ✓ Shear force effect generated by the interaction of the growing and departing bubbles on heating surfaces | $q'' \propto N_A^{1/4}\Delta T^2\left(1 + 0.3\frac{\Delta\tau_w}{\Delta\tau_d}\right)^{-1/2}$ | ✓ Nucleate site density<br>✓ Surface wettability |
| Hot/dry Spot | Ha and No (1998) | ✓ A random array of active sites and a unit shell of a radius around an arbitrarily selected active site<br>✓ Critical site number is five | $q'' = q_b \bar{N}(1 - P(n \geq n_c))$ | ✓ Nucleate site density<br>✓ Poission distribution |
| | Theofanous et al. (2006) | ✓ Microhydrodynamics of the solid-liquid-vapor line at the boundary of a hot/dry spot<br>✓ Irreversible hot spots are created and bring temperature excursion | $q''_{CHF,z} = k^{-1/2}\rho_v^{1/2} h_{lv}\sqrt[4]{\sigma g(\rho_l - \rho_v)}\sqrt{\frac{\rho_l + \rho_v}{\rho_l}}$ | ✓ Solid-liquid-vapor line at the boundary of a hot/dry spot |

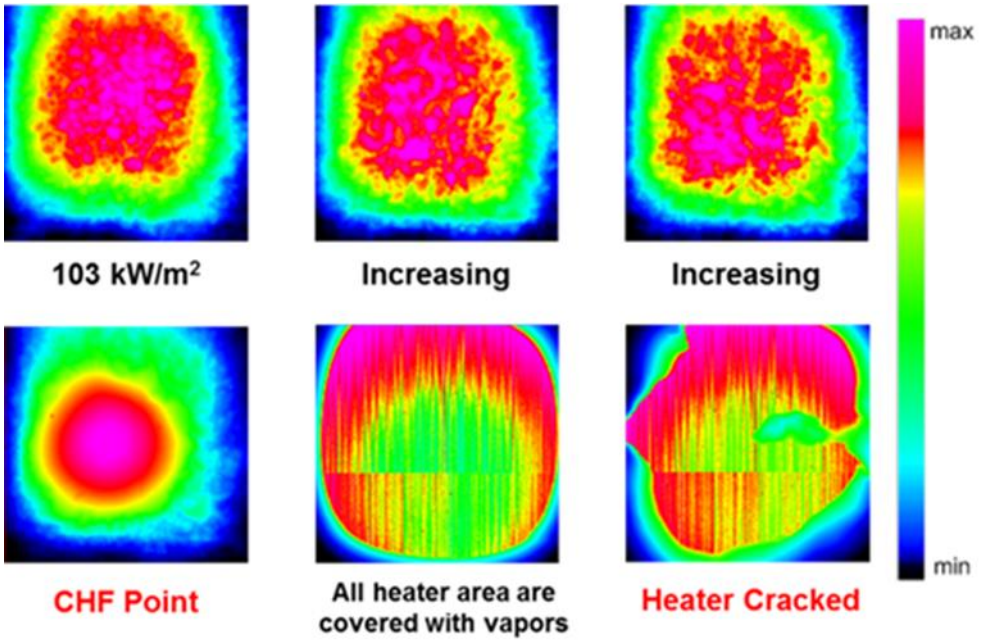


(a)

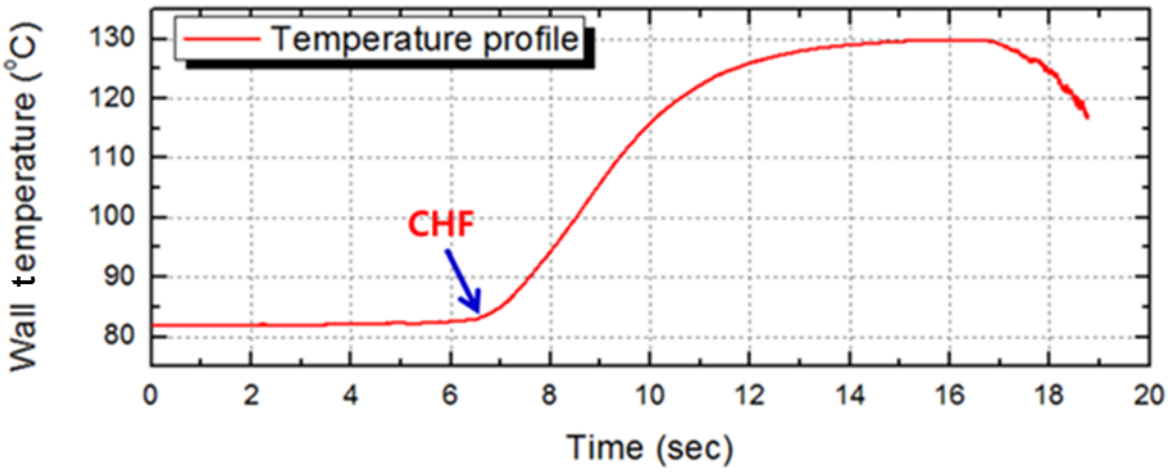


(b)

Fig. 2-7. IR observation at CHF region: (a) heating surface temperature distributions, (b) wall temperature profiles

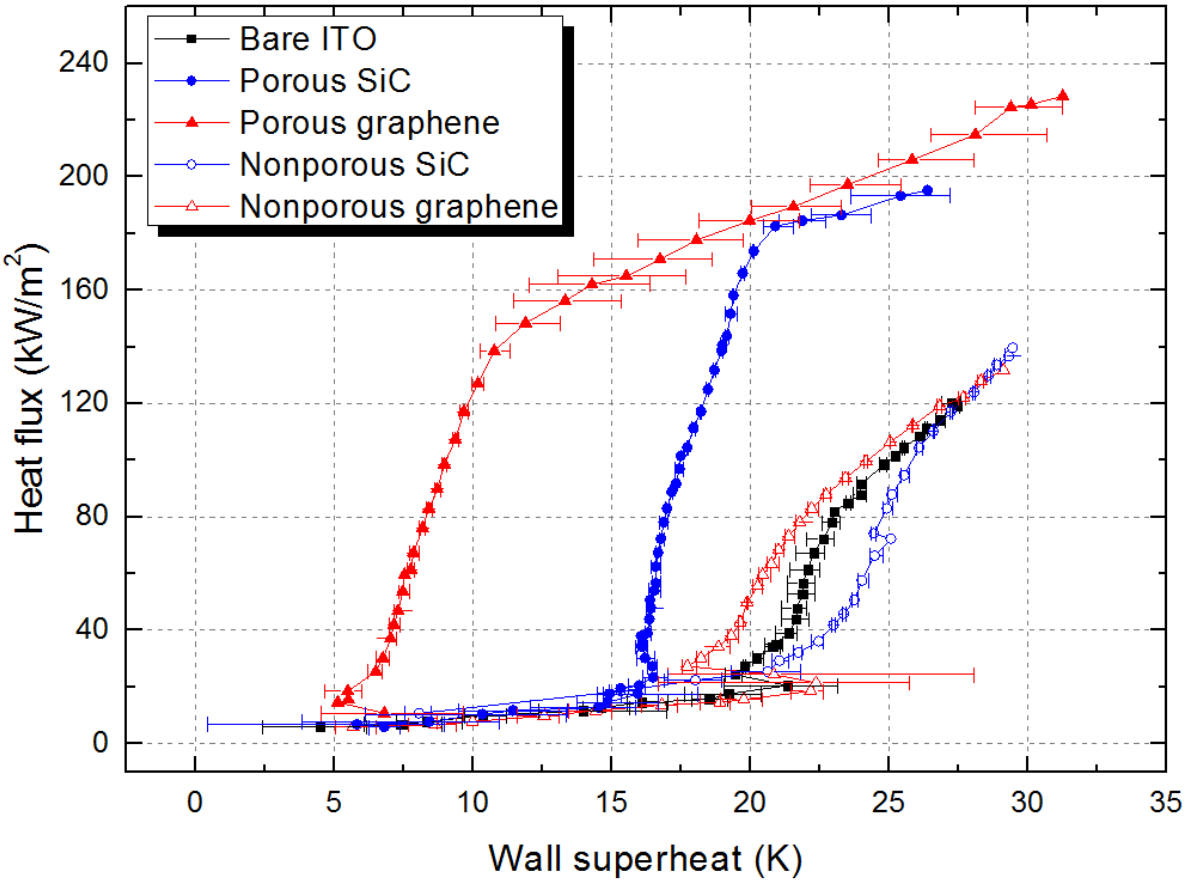


Fig. 2-8. Boiling curves for various heating surfaces

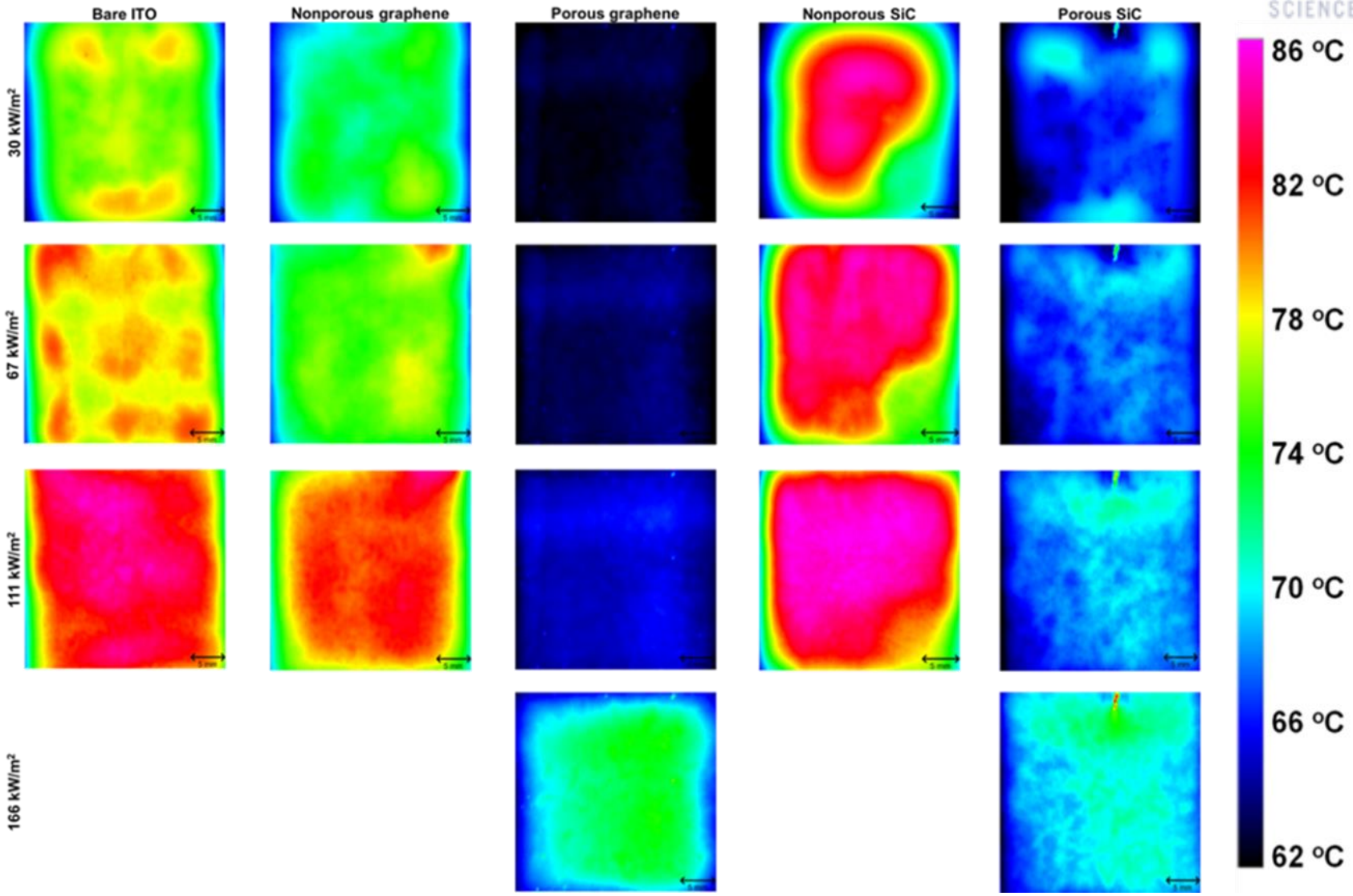


Fig. 2-9. Temperature fields of various heating surfaces under different heat fluxes

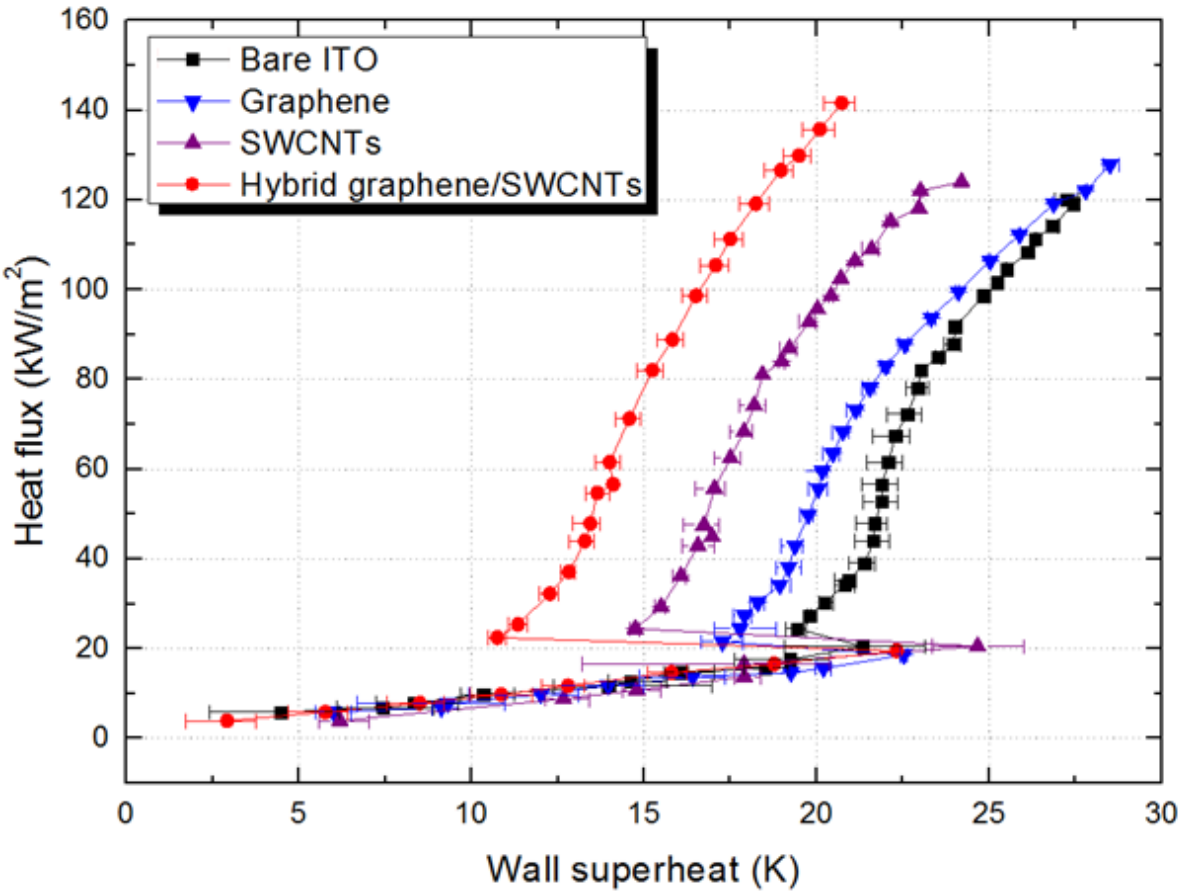


Fig. 2-10. Boiling curves for bare ITO, graphene, SWCNTs, and hybrid graphene/SWCNTs heating surfaces

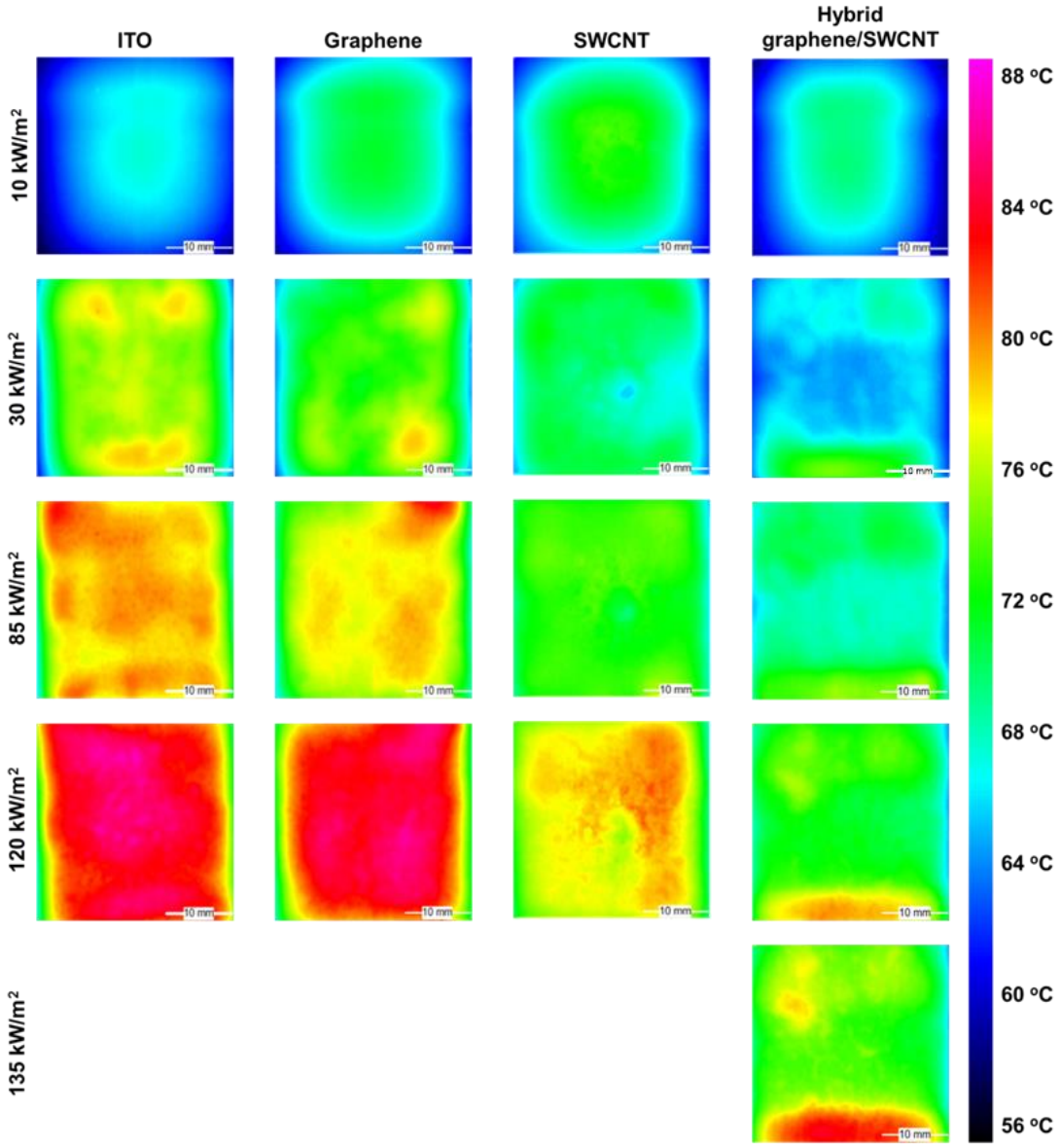


Fig. 2-11. Temperature distributions for bare ITO, graphene, SWCNTs, and hybrid graphene/SWNCTs heating surfaces at various heat flux conditions

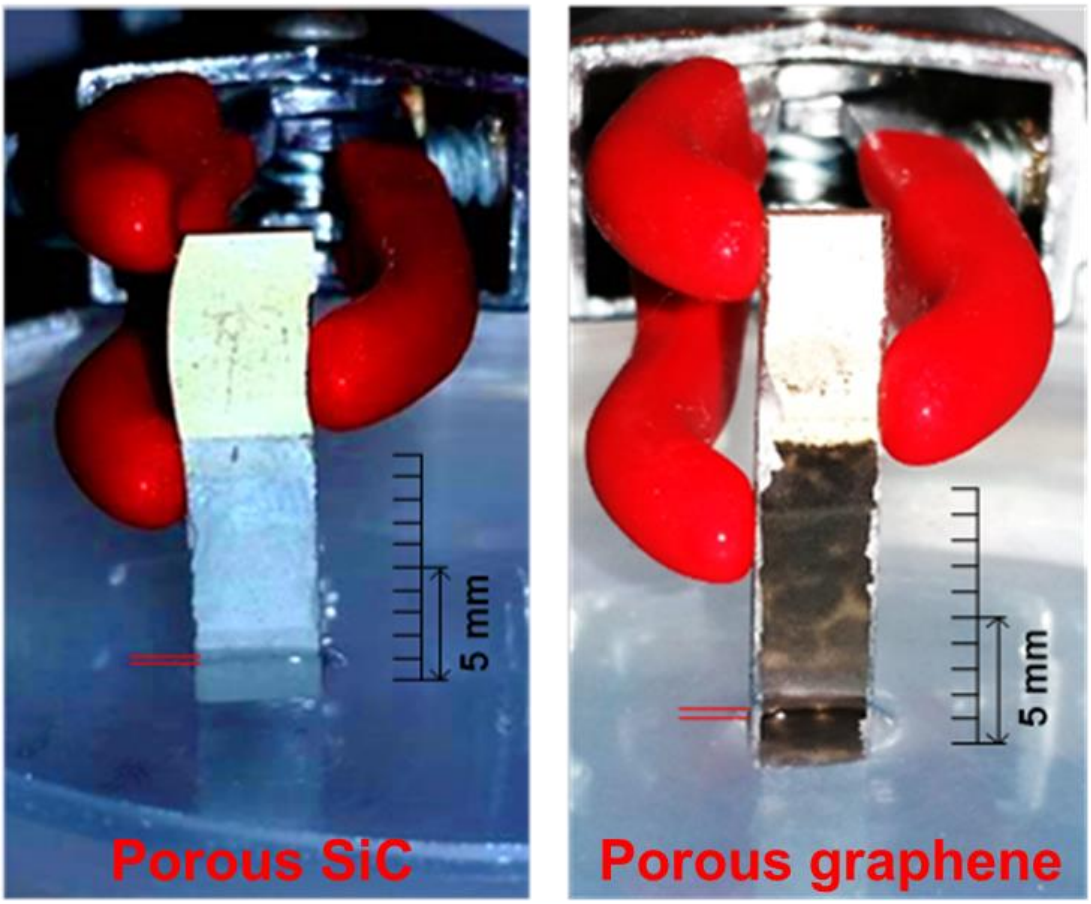


Fig. 2-12. Capillary height measurements for porous heating surfaces

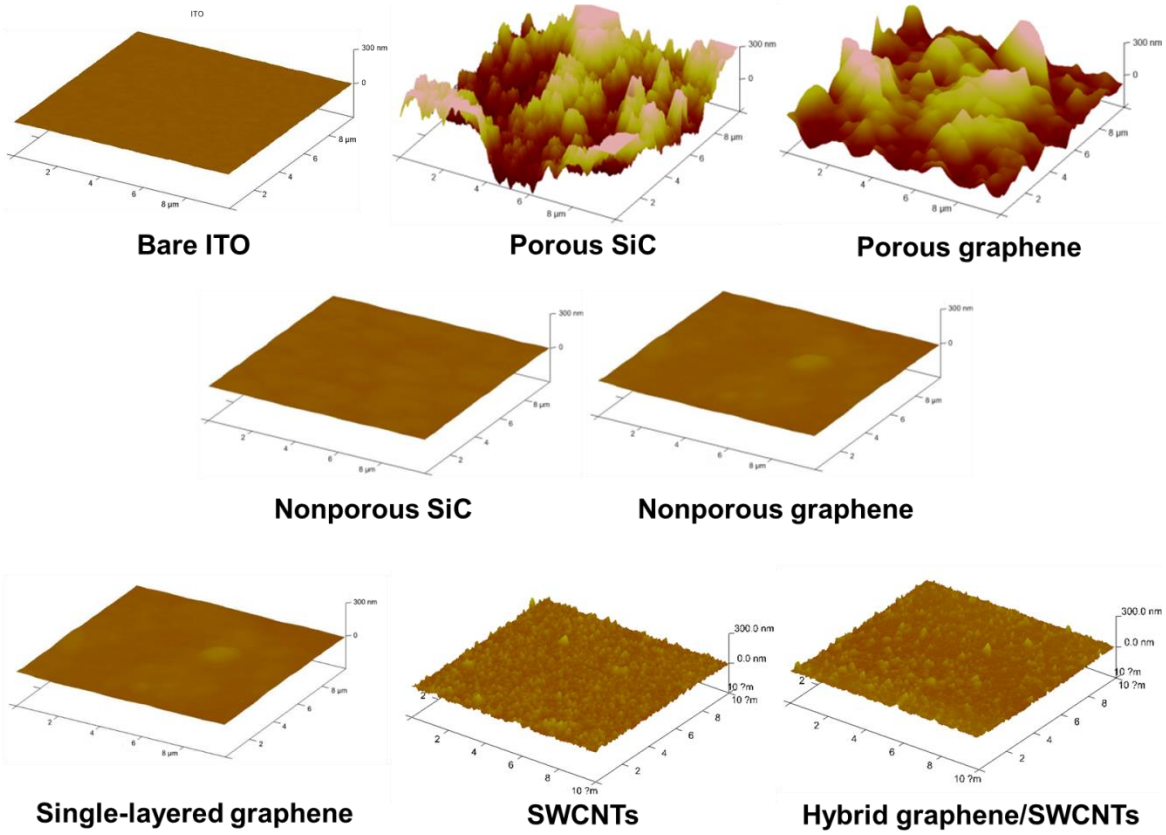


Fig. 2-13. AFM images for various heating surfaces

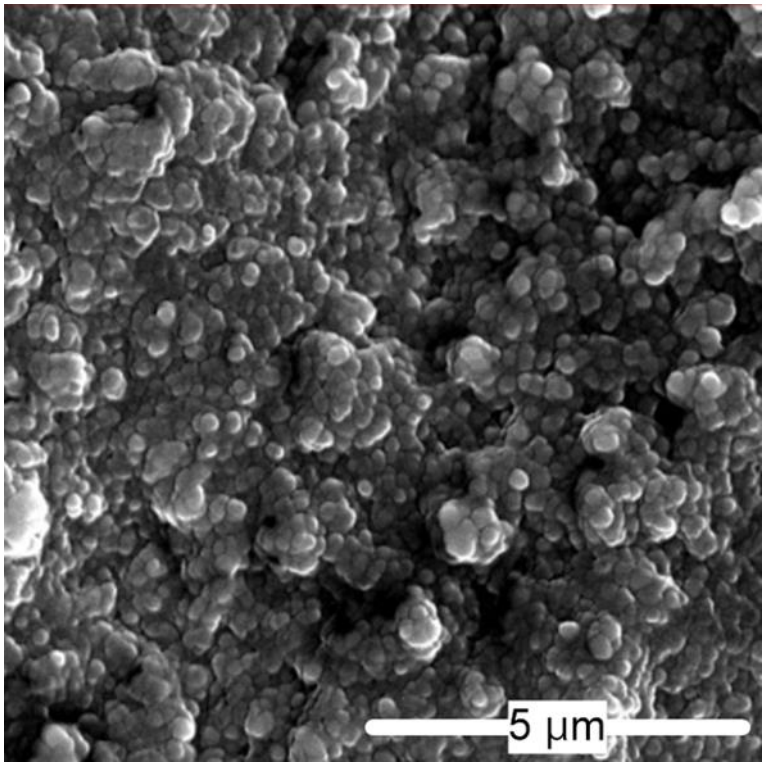


(a)

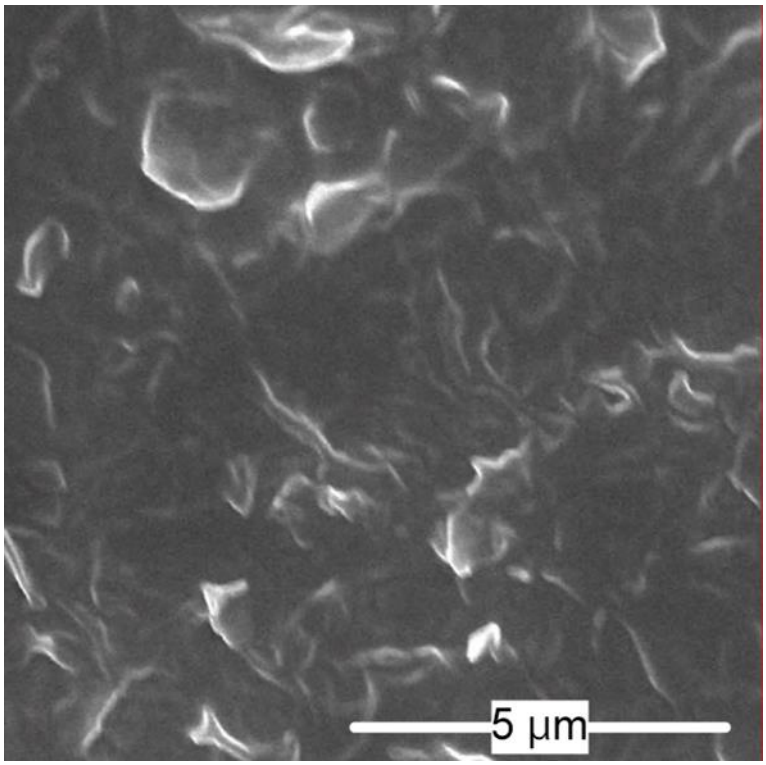


(b)

Fig. 2-14. Magnification heating surface images of (a) porous SIC, (b) porous graphene surfaces

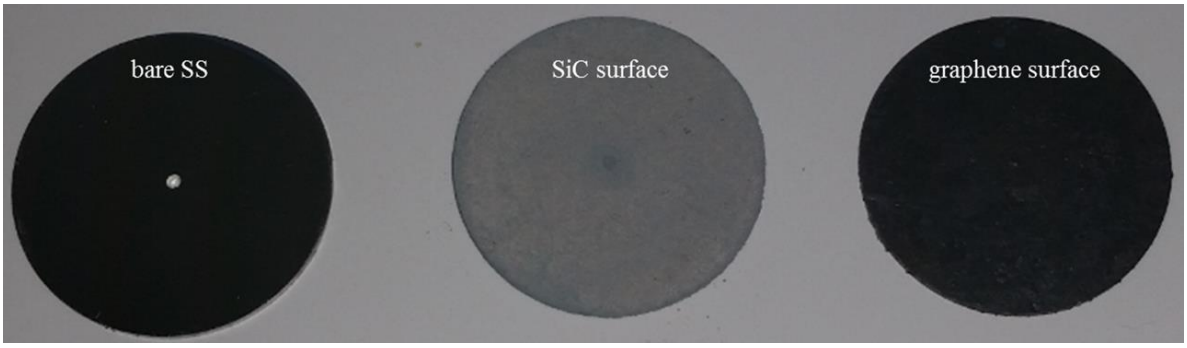


(a)

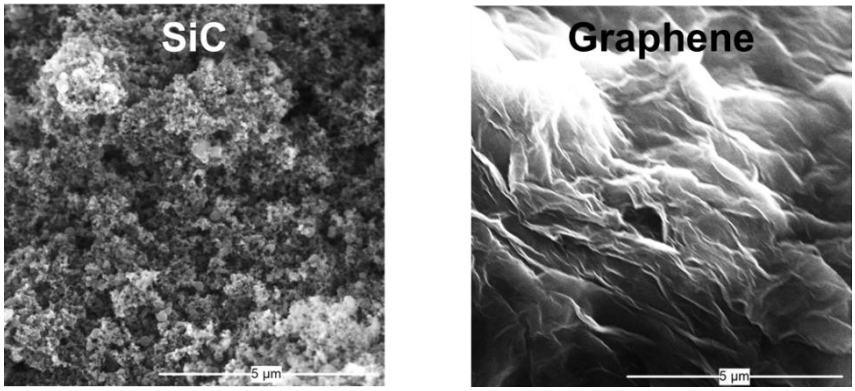


(b)

Fig. 2-15. Permeability analysis: (a) measurement samples, (b) SEM images of porous heating surfaces

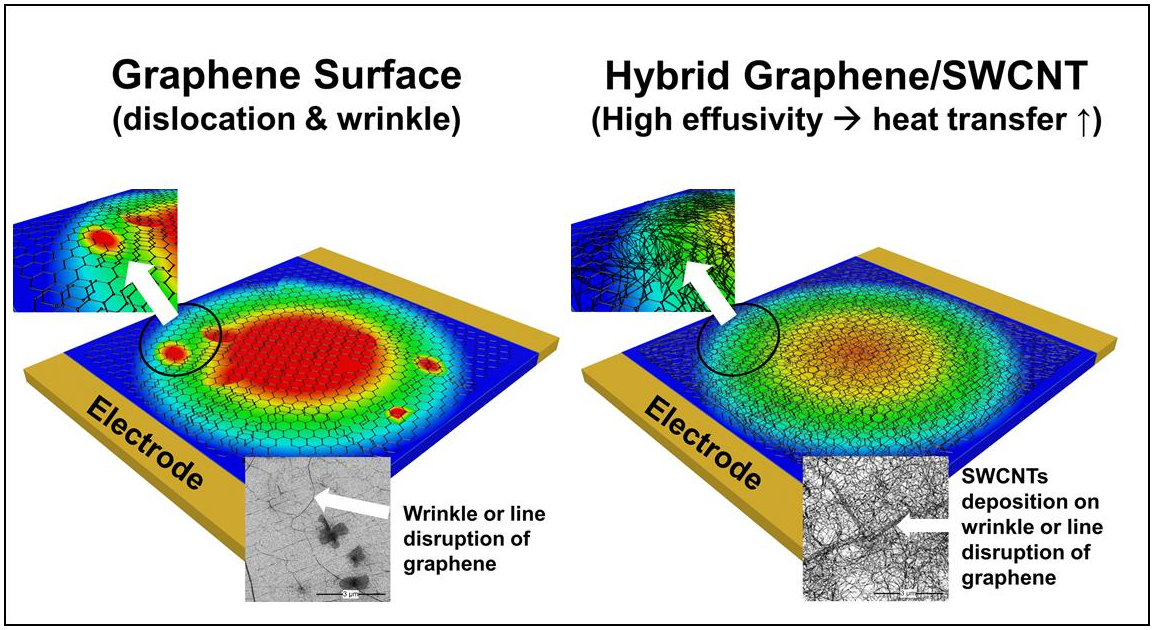


Fig. 2-16. Illustration of thermal transport phenomenon on graphene and hybrid graphene/SWCNTs heating surfaces

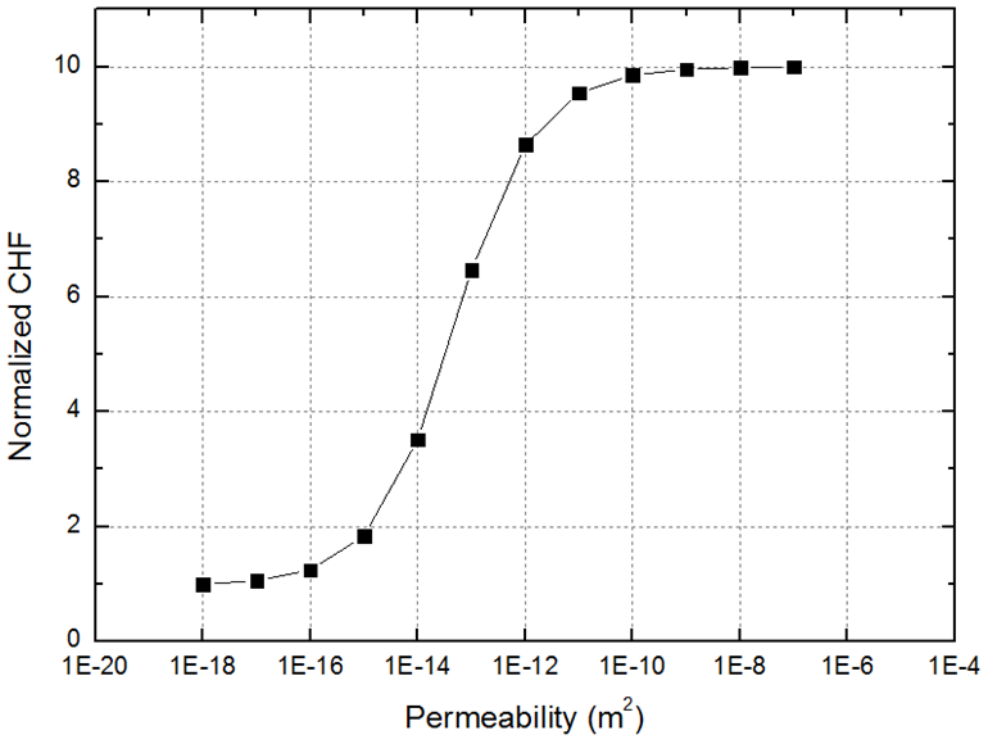


(a)

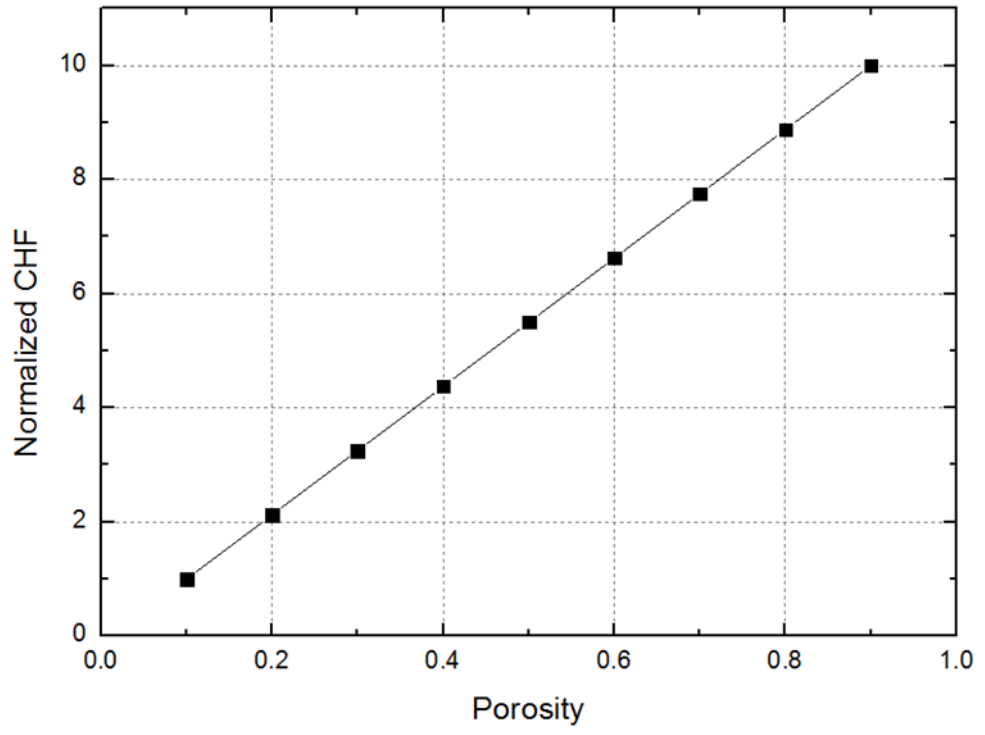


(b)

Fig. 2-17. Sensitivity analysis of (a) permeability, (b) porosity

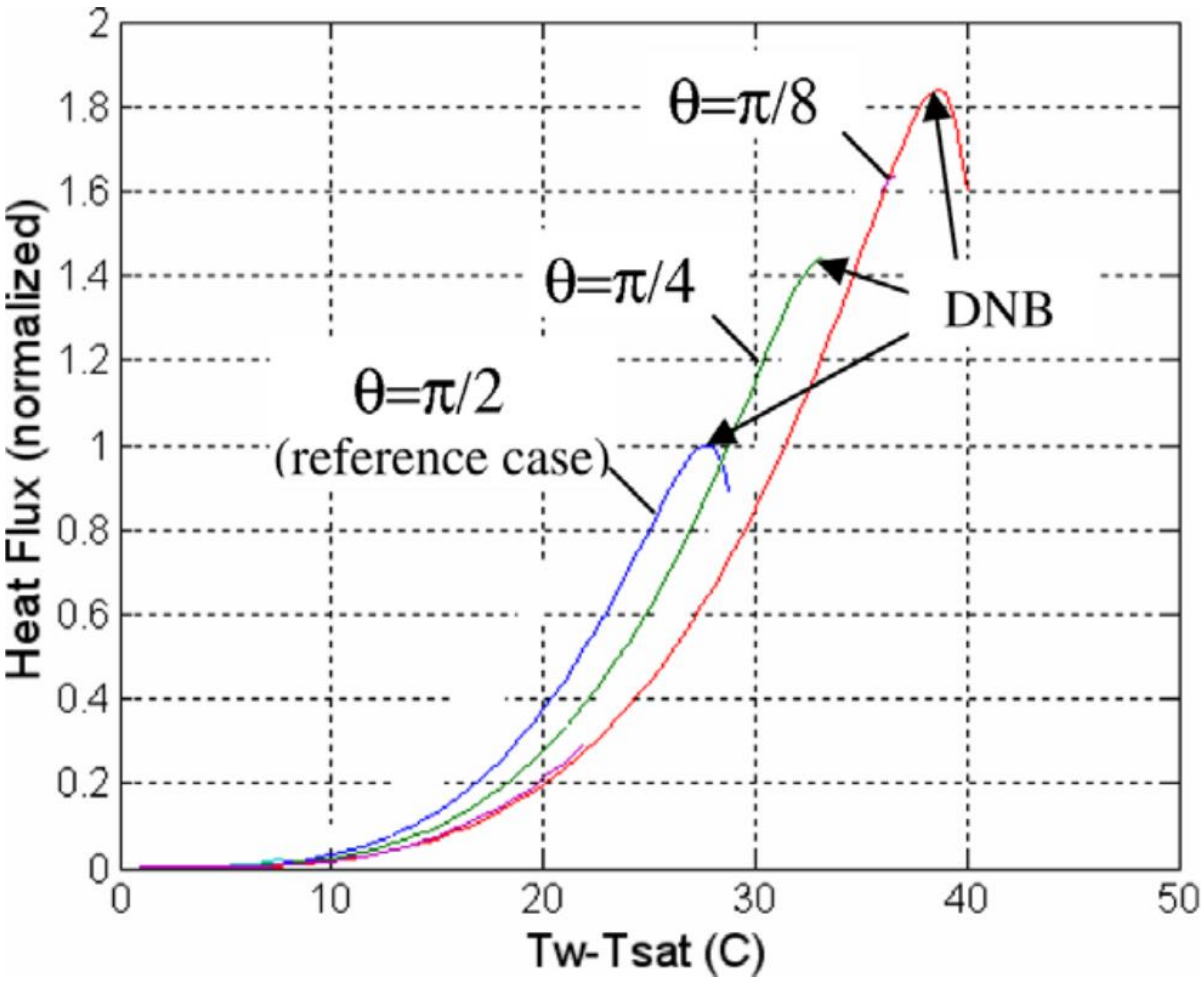


Fig. 2-18. Boiling curves based on bubble interaction thoery[5]

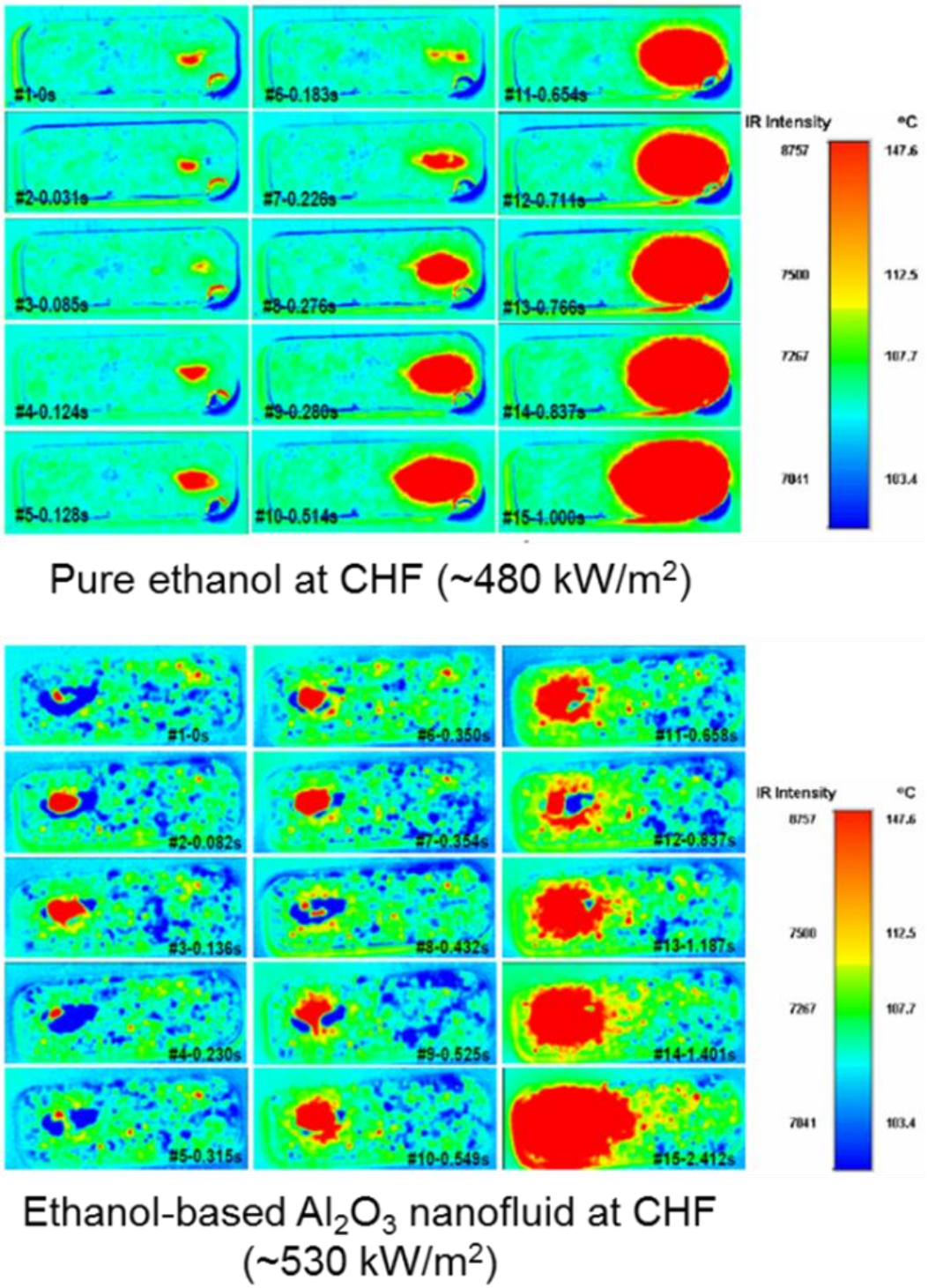


Fig. 2-19. IR observation of heating surfaces with pure ethanol and ethanol-based Al2O3 nanofluid[46]

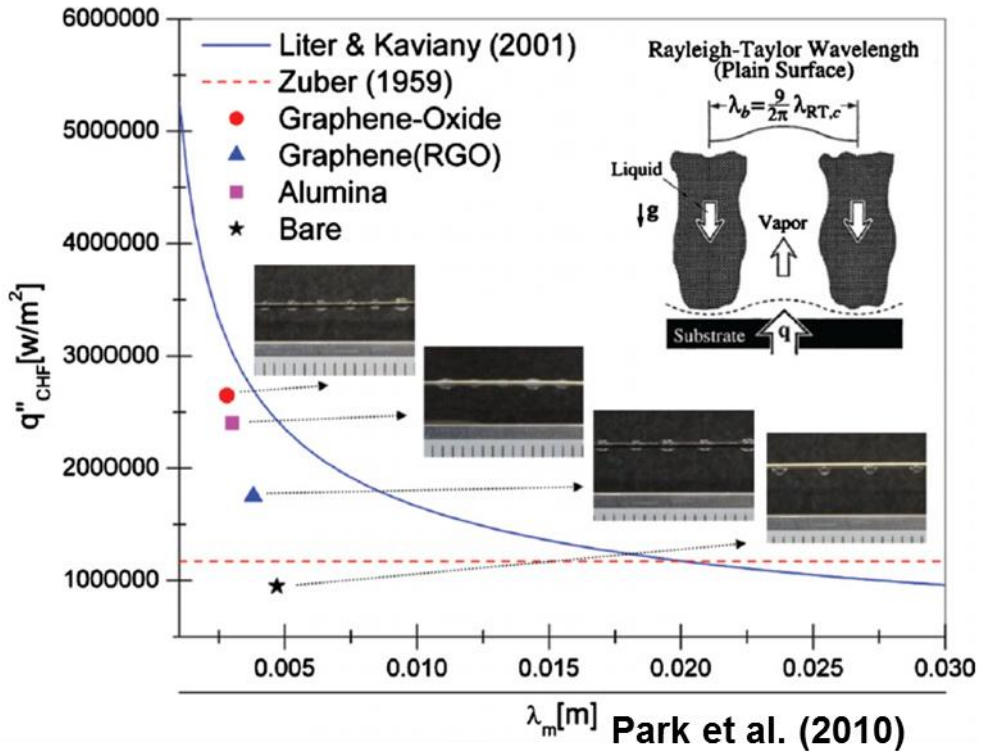


(a)

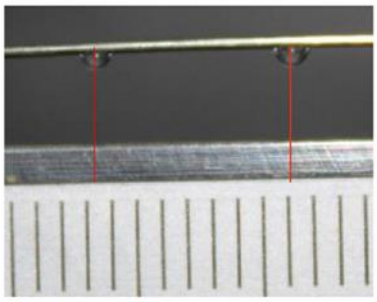

Bare surface

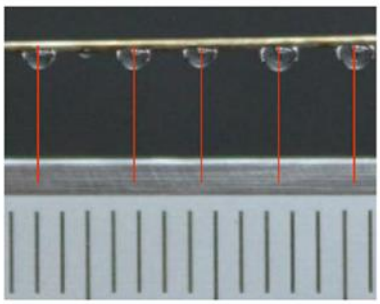

CuO-coated surface
(one-step method)

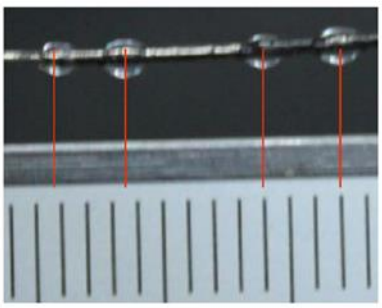

CuO-coated surface
(two-step method)

**Lee et al. (2012)**

(b)

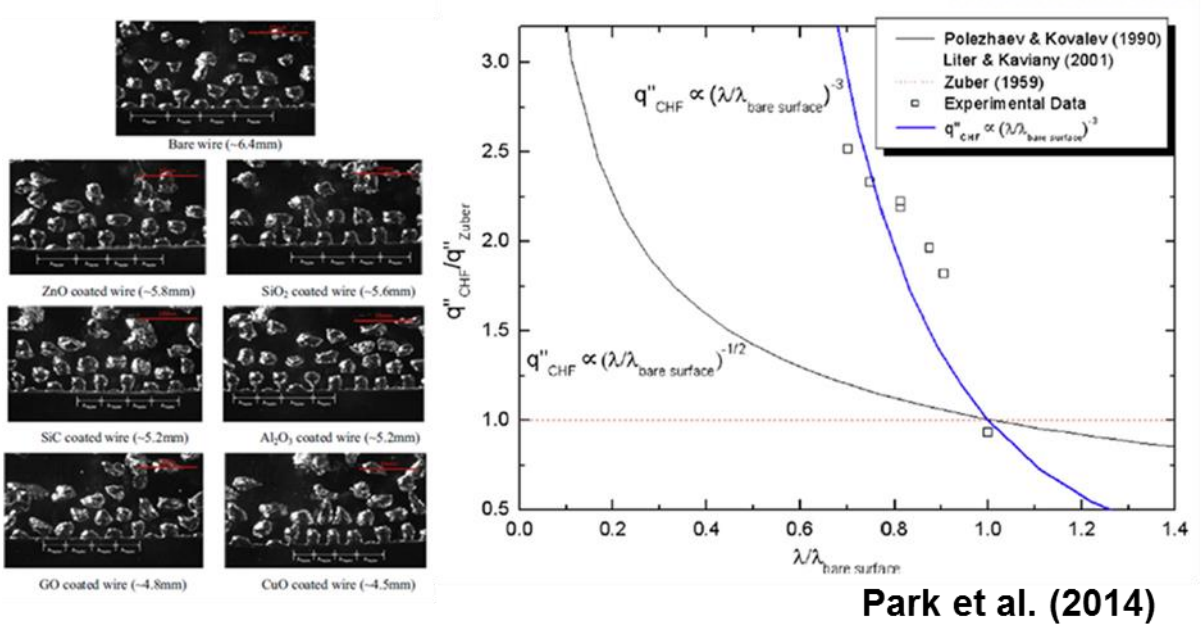


(c)

Fig. 2-20. CHF enhancement mechanism study based on modulation wavelength[9,54,11]

## 2.4 Conclusions

The CHF enhancement studies were performed in the plate pool boiling under various heating surfaces: bare ITO, porous SiC and graphene, nonporous SiC and graphene, single-layered graphene, SWCNTs, and hybrid graphene/SWCNTs. FC-72 refrigerant was used as the working fluid to suppress the effects of surface wettability and capillarity. The analysis of the surface parameters was examined based on the experimental results and various CHF prediction models were considered to predict the CHF results.

(1) The CHF value of the bare ITO surface was measured as 120.7 kW/m$^2$, which was similar value compared to the Zuber's hydrodynamic instability model. For the porous SiC and graphene heating surfaces, the CHF was enhanced up to 58% and 90%, respectively, than that of the bare ITO heating surface. On the other hand, the nonporous heating surfaces of SiC and graphene did not show the superior CHF enhancement.

(2) The hybrid graphene/SWCNTs heating surface could bring the most enhanced CHF and HTC compared to the bare ITO, single-layered graphene, and SWCNTs heating surfaces. The enhancement can be described by the superior thermal properties of the hybrid heating surface by connecting the wrinkles or the dislocation lines of the graphene with the SWCNTs.

(3) The analyses of the surface parameters that could influence on the CHF performance were conducted; surface wettability, capillarity, roughness, porosity, permeability, and thermal effusivity parameters were examined. The main purpose of the pool boiling CHF tests was to suppress the surface wettability by using the low surface tension working fluid. This means that the wettability was not considered as one of the major parameter in the CHF enhancement. The surface capillarity characteristics were examined only for the porous heating surfaces because there would be a liquid transport area in the heating structures. The measurement revealed that the surface capillarity did not influence on the CHF performance. The surface roughness for the porous heating surfaces was higher than other heating surfaces: the surface roughness may control the boiling performance. The porosity and the permeability were quantified through the measurement devices and the results showed that the porous graphene heating surface had higher porosity and permeability values compared to the porous SiC heating surface. The experimental results supported the measurement results of the porosity and permeability, but detailed quantification was impossible because the prediction CHF models, which considered those of surface parameters, limited to the millimeter- or micro-scale pore structures. The thermal effusivity test with the hybrid graphene/SWCNTs surface was examined and the results indicated that the higher thermal effusivity brought the CHF improvement by dissipating the hot or dry spots to the surrounding with the help of superior thermal properties.

(4) Various kinds of CHF models were evaluated to find the accurate model that could support the

experimental results. However, it was difficult to quantify the CHF enhancement ratio with comparison of existing CHF models. Instead of the existing CHF models, modified hydrodynamic approach for the CHF prediction was proposed. The detailed description for supporting the modified hydrodynamic approach will be described in the chapter 3 and 4.

# Chapter 3. CHF EXPERIMENTS BASED ON HYDRODYNAMIC INSTABILITY THEORY

## 3.1 Introduction

In this chapter, experimental works related to the CHF model based on the hydrodynamic instability theory were studied. The hydrodynamic instability model illustrated that critical vapor velocity determined the CHF region and the KH instability wavelength was a criterion for determining the critical vapor velocity. CHF studies related to the hydrodynamic instability theories have focused on the RT instability wavelengths and developing prediction models based on the change of the RT instability wavelengths. The measurement of the change of the RT instability wavelengths was conducted in a wire pool boiling and a plate pool boiling facilities to consider the RT instability wavelength as the CHF enhancement parameter. The experimental results indicated that the effect of surface characteristics should consider in the RT instability wavelength to predict the CHF trends.

## 3.2 Experimental Setup

The experiments for the validation of the hydrodynamic instability theory were conducted in two experimental facilities: pressurized wire pool boiling and plate pool boiling facilities. For the pressurized wire pool boiling facility, RT instability wavelengths were measured in various wire diameters and pressures for providing the background of the modified hydrodynamic CHF model. In the plate pool boiling facility, the patterned Pt heating surfaces for the RT instability wavelength measurements under various CHF results were performed.

### 3.2.1 Pressurized wire pool boiling facility

Fig. 3-1(a) exhibits a schematic diagram of the pressurized wire pool boiling apparatus. Boiling vessel and the pressurizer are installed in the facility. Boiling occurred in the boiling vessel and the pressurizer provides the desired system pressure during the experiments. The boiling vessel has dimensions of 250 mm × 200 mm with a height of 200 mm. The outer diameter and height of the pressurizer are 165.2 and 300 mm, respectively. An $N_2$ gas container is connected to the pressurizer for the controlling the system pressure. The design limit of the pressure and the temperature in the boiling vessel and the pressurizer is 20 bar and 200 °C, respectively. The desired temperature of the facility was controlled by the PID controller. For the pressure control, backpressure regulators were connected in the boiling vessel and the pressurizer, respectively. Boiling observations in the boiling vessel was provided through the visualization ports. In addition, there is a visualization window in the pressurizer to support that the working fluid is filled in the boiling vessel.

In the experiment, various diameters of Ni-Cr wire were used and the wire connected with the DC power supply (150V, 35A). Fig. 3-1(b) exhibits the detailed description of the wire connection to the copper electrodes. To connect the electrodes and the wire, there was a hole on the electrodes and a bolt. The test specimen of Ni-Cr wire was 110 mm length. To measure the current, the standard resistance was used. The DAS recorded the applied voltage and current during the experiment. In addition, the temperature in the boiling vessel and pressurizer were monitored by the DAS. The heat flux of the wire was calculated using the following equation:

$$q'' = \frac{VI}{\pi DL} \qquad (3\text{-}1)$$

where q″ is the heat flux, V is the voltage, I is the current, D is the wire diameter, and L is the length of the wire specimen.

As a working fluid, R-123 refrigerant was selected because the boiling point is low compared to FC-72 and water (27.6 °C). This means that it was easy for maintaining the saturation state of the R-123 even at high pressures, compared to the water. In addition, the test specimen was not damaged or burnout even though the CHF appeared. Various diameters of Ni-Cr wire were considered: 0.3, 0.5, and 0.7 mm. At atmosphere pressure, three kinds of different diameters were used in the experiment. In addition, the diameter of 0.5 mm wire was used in various pressures to measure the RT instability wavelength with respect to CHF results.

The applied heat flux on the wire was controlled by the voltage control. When there was a significant margin to the CHF, the heat flux was controlled at ~20 (kW/m$^2$)/min. When the CHF is approached, the heat flux was controlled at ~5 (kW/m$^2$)/min. After the transition process from the nucleate boiling to stable film boiling, HSV captured the RT instability wavelengths. The heat flux was then decreased until the MHF point was reached. HSV recorded boiling occurrence at the MHF point. The uncertainty of the diameter and length of the Ni–Cr wire was ±1%. The uncertainty of the voltage and current is ±1% and ±1%, respectively. The uncertainty of the heat flux was ±1.7%, which was calculated using the following equation:

$$\frac{\Delta q''}{q''} = \sqrt{\left(\frac{\Delta V}{V}\right)^2 + \left(\frac{\Delta I}{I}\right)^2 + \left(\frac{\Delta(\pi DL)}{(\pi DL)}\right)^2} \qquad (3\text{-}2)$$

Fig. 3-2 exhibits the experimental setup with the HSV. The record rate of the HSV was 500 fps. The calibration of the HSV was simultaneous obtained with a calibration sheet that was located on the visualization port. The average distance of the vapor columns assumed as the RT instability wavelength and several images were considered to get the average RT instability wavelength.

### 3.2.3 Patterned plate heating surfaces

CHF enhancement through the patterned Pt surfaces was examined in the plate pool boiling experiment. The RT instability wavelength observations for various heating surface conditions were used to investigate the relationship of the RT instability wavelength with the CHF results. The surface modification was conducted on the direct Pt heating surface.

Heater surface fabrication procedure for the Pt heating surfaces was shown in Fig. 3-3(a). The test heater was composed of the Si wafer substrate with the thickness of 500 μm. The size of the Si wafer for the heater was 30 mm × 30 mm. 100 nm-thick oxidation layer was deposited on the Si substrate for the passivation of the test sample. A Cr of 20 nm thin film was used as the adhesion layer between the Si substrate and the Pt layer. Then, the heating material of Pt layer was deposited on the substrate via an electron-beam (E-beam) evaporator with having an area and a thickness of 30 mm × 20 mm and 100 nm, respectively. The specific patterns were formed by photolithography techniques with photoresist. The electrodes with having an area of 5 mm × 20 mm were deposited at the end of the Pt layer through E-beam evaporator with adhesion Cr layer. Therefore, the actual heating surface area used in the pool boiling experiment was 20 mm × 20 mm.

As heating surfaces, four kinds of heating modification were considered: plain, 9 holes, 49 holes, and 169 holes. The patterned surfaces were fabricated by inductively coupled plasma reactive ion etching (ICP-RIE) process. With the ICP-RIE, the patterning depth of 50 nm was etched. The diameter of patterned surface for 9 holes, 49 holes, and 169 holes was 3, 1.5, and 0.75 mm, respectively. Pitch per diameter ratio was the same as 2 for every heating surface. The area enhancement due to the patterned surfaces was not considered because the maximum area enhancement ratio for the 169 holes heating surface was less than 0.001%. Fig. 3-3(b) shows heating surface magnification images obtained. As shown in Fig. 3-3(b), the plain Pt heating surface revealed that it has no microcavities; nanosmooth heating surfaces.

A preliminary heating test of the heating surfaces was conducted to show the effect of the patterned heating surfaces at low heat flux regions. Fig. 3-4 shows temperature fields for the heating surfaces at a certain heat flux (40 $kW/m^2$): Fig. 3-4(a) exhibits the temperature distributions on the heating surfaces and Fig. 3-4(b) shows boiling occurrences at that heat flux. As shown in Fig. 3(a), distinct temperature fields on the patterned heating surfaces were found. Higher temperature fields existed at the patterned heating surfaces, compared to the plain heating surface. In addition, HSV results indicated that boiling was concentrated on the patterned heating surfaces.

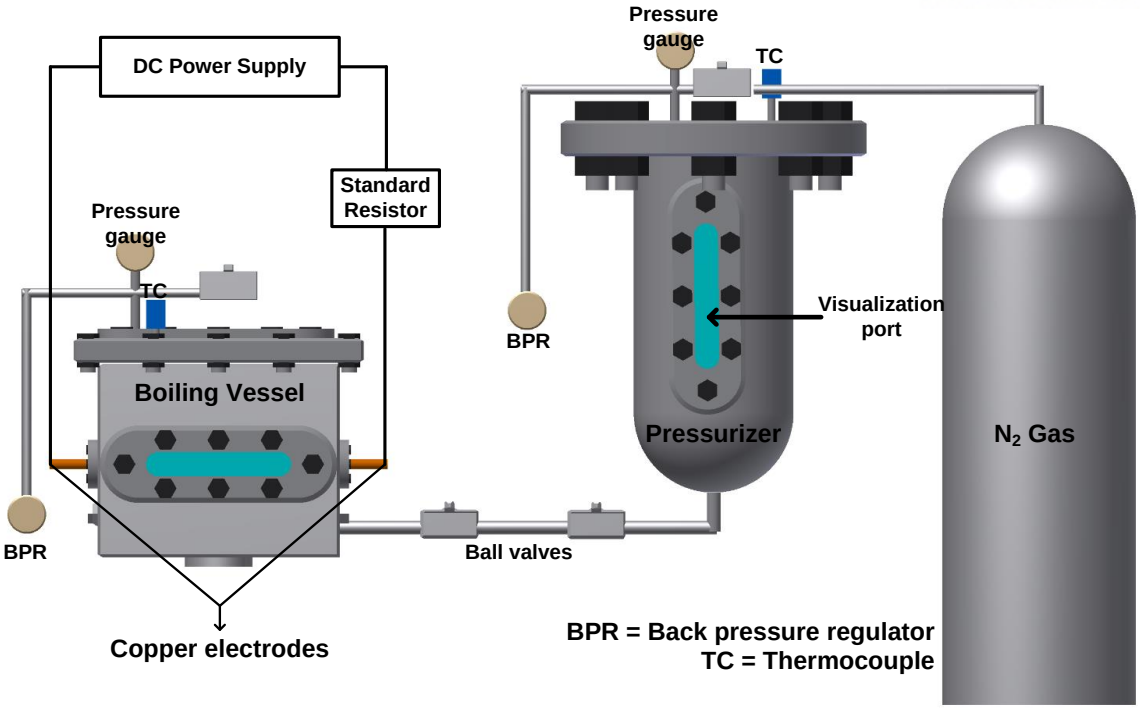


(a)

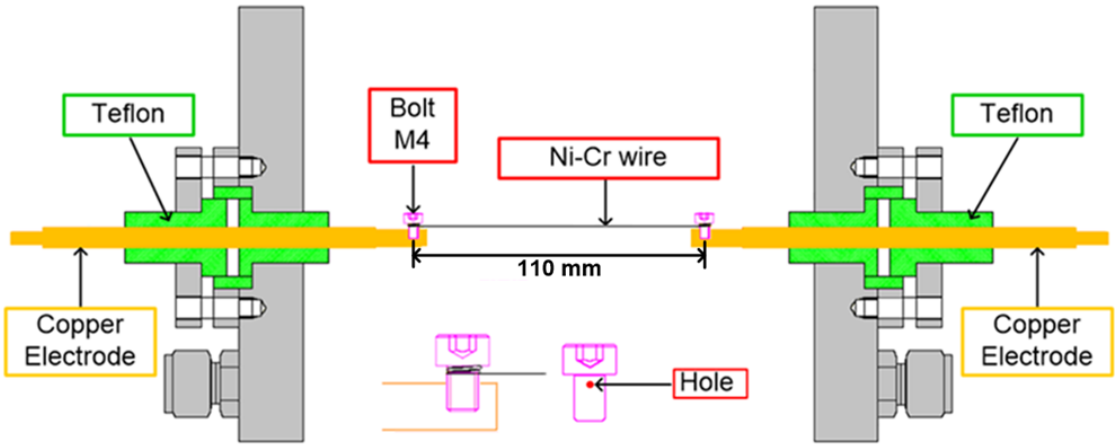


(b)

Fig. 3-1. Pressurized wire pool boiling facility: (a) schematic diagram, (b) connection of wire on copper electrodes

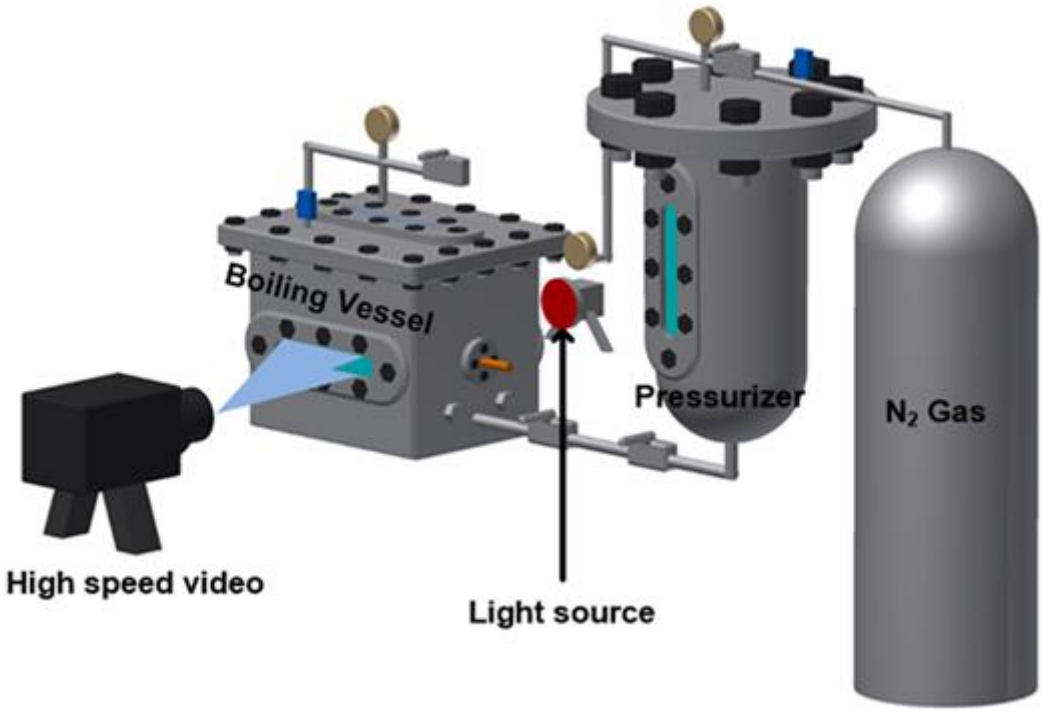


Fig. 3-2. Setup for RT instability measurements through the HSV

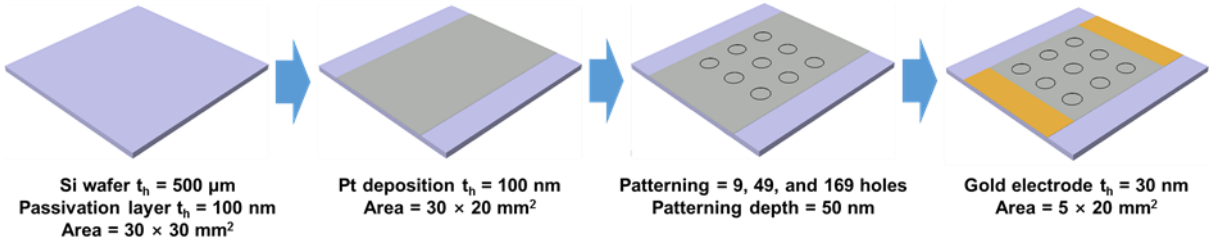


(a)

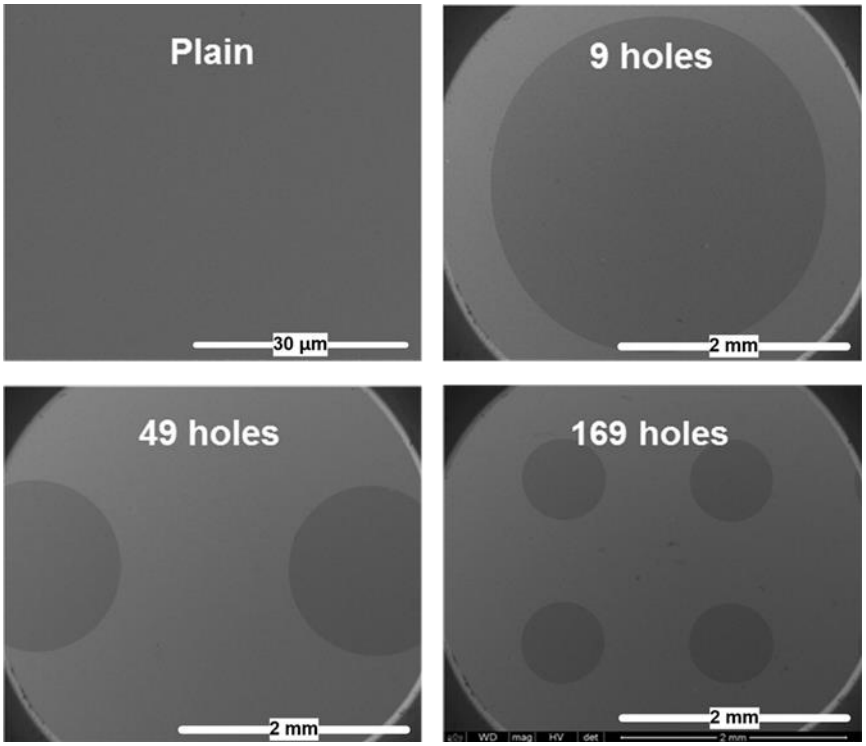


(b)

Fig. 3-3. Patterned Pt surface fabrication: (a) procedure of the patterned Pt samples, (b) surface images through SEM

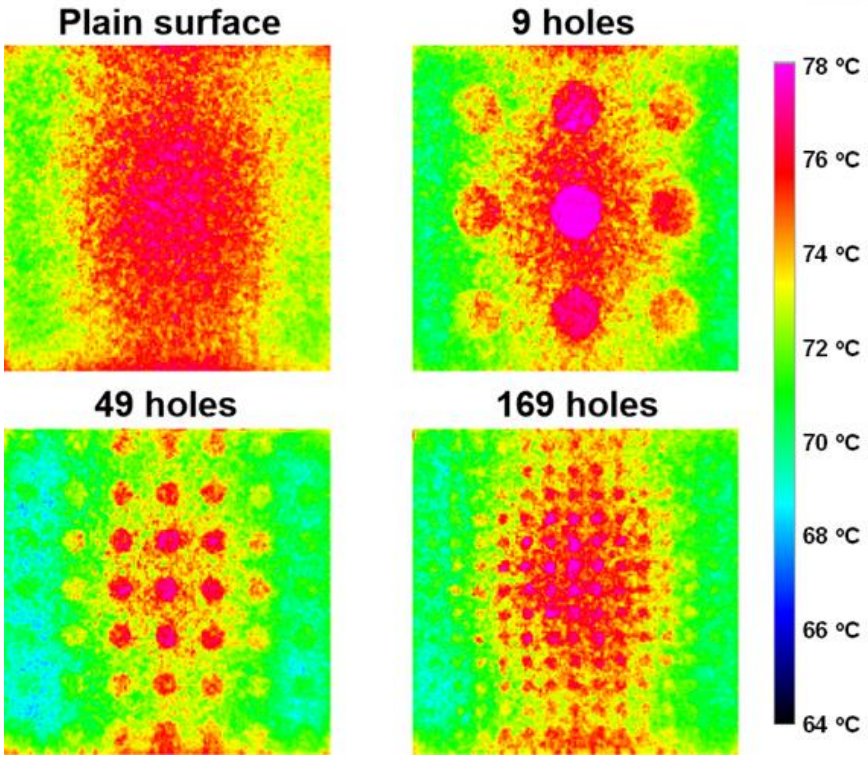


(a)

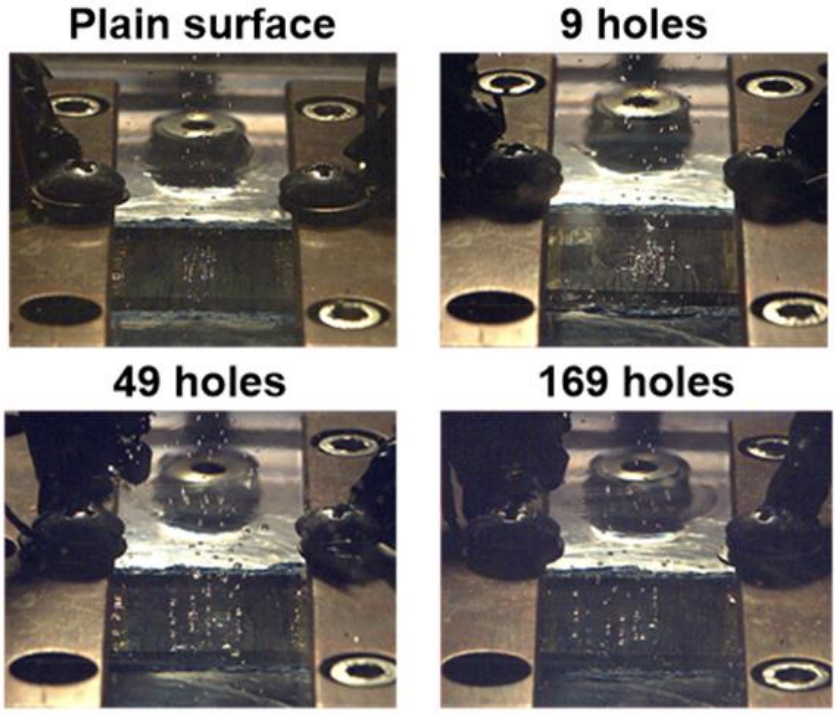


(b)

Fig. 3-4. Patterned Pt surface (a) temperature fields at a certain heat flux, (b) boiling observation images using HSV

### 3.3 Results and Discussion

The experimental results are divided into two parts for the wire pool boiling experiments: (1) the effect of heater diameters and (2) the system pressures effects on the test specimen to find the connection between the RT instability wavelengths and the CHF results. Measurements of the RT instability wavelength and variations in the RT instability wavelength with changes in the CHF, MHF, and heater surface diameters were evaluated. To ensure the reliability of the experimental results, three specimens were used for each test condition. Fig. 3-5 exhibits the typical wire pool boiling results at the nucleate boiling, CHF, film boiling, and MHF regions.

Three kinds of wire specimens were used to determine that RT instability wavelength is influenced by the heater diameters. The CHF values were measured as 202.42, 191.8, and 249.19 kW/m$^2$ for the 0.3, 0.5, and 0.7 mm diameter, respectively. On the other hand, the prediction model based on the hydrodynamic instability theory was 216.04 kW/m$^2$. The CHF results were similar to the calculated value, but the average distance of the RT instability wavelengths was different. Fig. 3-6 is the experimental results for the 0.3, 0.5, and 0.7 mm wire diameters. Table 3-2 lists the CHF and MHF results according to the heater diameters. The results indicated that there was an influence of the heater diameters on RT instability wavelength. Lienhard and Wong[55] proposed a model with considering the effect of heater diameters on RT instability wavelength. This means that further consideration should be conducted in various heating conditions. In addition, pressure system pressures were considered into the study to observe the RT instability wavelengths. The wire diameter of 0.5 mm was used because the 0.3 mm wire diameter did not endure the high heat flux conditions and the analysis of the 0.7 mm wire diameter was not ideal because the formation of the RT instability was not balanced.

A 0.5 mm wire diameter was used for the analysis of the RT instability wavelengths according to CHF results. Various kinds of pressures were considered: 1, 3, 5, 7, and 9 bar. Table 3-3 lists the results of the CHF and MHF. Fig. 3-7 shows the CHF and MHF based on the system pressures. The average CHF values at 1, 3, 5, 7, 9 bar were 197.4, 433.2, 493.9, 555.4, and 625.8 kW/m$^2$, respectively. The measured MHF values for each system pressure were 107.4, 163.5, 222.6, and 247.9 kW/m$^2$, respectively. As shown in Fig. 3-7, the CHF and MHF values were increased as the loaded system pressures. RT instability observations under various conditions were illustrated in Fig. 3-8. The bubble diameter was changed according to the loaded pressure. As the bubble departure diameter decreased, the wavelength also decreased to compensate for the heat transfer rate; this increased the departure bubble ratio of the heater surface with latent heat transport. The HSV images were used to analyze the relation between the RT instability wavelength and the CHF and MHF. Based on the experimental tests, there were the relation between the RT instability wavelengths and the CHF or MHF performances.

To analyze a trend of the RT instability observations with the CHF and the MHF results, the measured RT instability wavelength results were plotted. To determine the RT instability wavelengths, the average

distance of the vapor columns was considered and several images were used. Based on the measurement of RT instability wavelength, the maximum mean absolute error (MAE) and root-mean-square (RMS) error for a certain experimental case were 16.7 and 12.1 %, respectively. Except for the case, MAE and RMS error for the average distance of the vapor columns (RT instability wavelength) were less than 10 %. In addition, several experimental data were examined to provide normal distributions of the RT instability data. Fig. 3-9 exhibits normal distributions of the measured RT instability wavelengths. The standard deviation was decreased as the average RT instability wavelength was decreased. This inferred that the reliability of the average RT instability wavelength increased as the RT instability wavelength decreased.

As shown in Fig. 3-10, the CHF and MHF increased as the RT instability wavelength decreased and vice versa. This means that actual measurement of the RT instability wavelength is a valid approach for the CHF prediction. To evaluate the experimental data, the modified hydrodynamic concept of modulation wavelength was used. In the chapter 1, the modulation wavelength was predicted by the heating surface structure characteristics, but the measured RT instability wavelengths were used in the present wire pool boiling experiments.

$$q''_{CHF,h} = \frac{\pi}{8} h_{fg} \left( \frac{\sigma \rho_g}{\lambda_m} \right)^{1/2} \qquad (3\text{-}11)$$

where $\lambda_m$ is the measured RT instability wavelengths in the present study. Fig. 3-11 exhibits the modified hydrodynamics approach model and experimental results. The experimental CHF results and predicted CHF values were similar tendencies and values. This means that the change in CHF values can be explained by the change in the RT instability wavelength at the film boiling region. Based on the experimental results, RT instability wavelengths are the valid method for predicting the CHF results; the RT instability can be considered in the critical vapor velocity which determines the CHF. It inferred that the RT instability wavelength can be correlated with the critical vapor velocity; the assumption of the hydrodynamic instability theory is proven.

The two-dimensional RT instability measurements were also conducted in the plate pool boiling with the patterned Pt heating surfaces. Four kinds of heating surfaces were prepared in the pool boiling experiment. Boiling curves for all heating surfaces with various patterned conditions are shown in Fig. 3-12. For the plain heating surface, the average CHF value was 146.1 kW/m$^2$. For the hydrodynamic instability CHF model, the predicted CHF value of FC-72 was 148.2 kW/m$^2$. Based on the prediction model, the reliability of the experimental procedure was confirmed. The effect of patterned heating surfaces was observed in the CHF performance. The CHF of the 9 holes, 49 holes, and 169 holes heating surfaces were 158.2 kW/m$^2$, 165.4 kW/m$^2$, and 173.1 kW/m$^2$, respectively. The CHF enhancement ratio compared to the plain Pt heating surface was 8.3%, 13.2%, and 18.5% for the 9 holes, 49 holes, and

169 holes heating surfaces, respectively. As shown in Fig. 3-12, boiling heat transfer performance was almost same for every heating surface. The highest HTCs were observed at near CHF points: 5.75, 5.85, 6.18, and 6.45 kW/m$^2$ K for the plain, 9 holes, 49 holes, and 169 holes heating surfaces. To investigate the boiling performance on the heating surfaces, HSV was used to capture the bubble generation at 50, 75, and 100 kW/m$^2$ for the plain, 9 holes, 49 holes, and 169 holes heating surfaces. The capture speed of the HSV was set to 2000 fps. Fig. 3-13 exhibits the bubble generations on all heating surfaces. The bubble generation at different heating surfaces showed similar performance. The captured images supported that the HTCs at nucleate boiling region were almost same for every heating surface. Previous studies related to the HTC enhancement mentioned that the HTC improvement could be explained by the change of surface characteristics compared to the bare surface[13,53,56]. The well-known prediction model for the boiling heat transfer from thermo-phyical properties and wall superheat with surface materials was proposed by Rohsenow[23].

$$\frac{C_{pl}\Delta T}{h_{lv}} = C_{sf}\left\{\frac{q''}{h_{lv}\mu_l}\left[\frac{\sigma}{g\left(\rho_l-\rho_v\right)}\right]^{1/2}\right\}^m\left(\frac{C_{pl}\mu_l}{k_l}\right)^n \qquad (3\text{-}12)$$

where $C_{pl}$ is the liquid specific heat, $h_{lg}$ is the latent heat, $C_{sf}$ is the surface fluid combination, $\mu_l$ is the dynamic viscosity, $k_l$ is the liquid conductivity, and m and n are the exponents of the correlation. The parameter of the $C_{sf}$ is related to the surface characteristics. Ho et al.[56] used micro-fin and micro-cavity surfaces to enhance boiling performance and they correlated the value of $C_{sf}$ with the surface roughness factor, which is derived by the ratio of actual heating surface and projected area. In addition, the average roughness value was considered into $C_{sf}$ to predict the boiling performance under roughness-controlled heating surfaces[53]. In the present study, however, surface characteristics such as surface roughness and deposition of highly-conductive material were not considered. This means that HTC of various patterned surfaces should be similar for all heating conditions.

The RT instability wavelength measurements were performed to find the relation with the CHF results. Fig. 3-14 exhibits the measurement of the RT instability wavelength at CHF region for all heating surfaces. As shown in Fig. 3-14, the CHF increased as the RT instability wavelength decreased and vice versa. The measurement results indicated that the change of the RT instability wavelength supported the CHF performance. This means that the change of the RT instability wavelength influences on the critical vapor velocity. This inferred that CHF can be influenced by the RT instability wavelength.

The critical and the most dangerous RT instability wavelength of the working fluid are 4.9 and 8.5 mm, respectively. In the present study, we assumed that the KH instability wavelength is related to the RT instability wavelength. If the patterned surface changed the RT instability wavelength based on the

heater geometry, the RT instability wavelength of the 9 holes heating surface would be changed and following relation could be predicted.

$$n = a\left(\lambda_{RT} / \lambda_{\mathrm{mod}}\right)^{0.5} \qquad (3\text{-}13)$$

where n is the change of CHF ratio and a is the fitting constants. When the fitting constant has a value of 1, the CHF enhancement ratio for the 9 holes, 49 holes, and 169 holes heating surfaces is 4.08, 15.5, and 28.1%, respectively. The modified hydrodynamic approach showed similar trend that of the experimental results. Therefore, the modified hydrodynamic instability model based on the change of the RT instability observation on flat heater can predict the change of the CHF performance. Based on the experimental studies, the hydrodynamic instability theory should consider the effect of surface characteristics in the RT instability wavelength to predict the CHF enhancement mechanisms.

Table 3-1. CHF and MHF values according to heater diameters

| Specimen (diameter) | 0.3 mm | | 0.5 mm | | 0.7 mm | |
|---|---|---|---|---|---|---|
| | CHF | MHF | CHF | MHF | CHF | MHF |
| # 1 ($kW/m^2$) | 216.32 | 84.78 | 181.7 | 104.5 | 251.18 | 122.91 |
| # 2 ($kW/m^2$) | 208.07 | 88.35 | 197.3 | 101.4 | 233.12 | 128.42 |
| # 3 ($kW/m^2$) | 182.88 | 85.99 | 196.5 | 122.3 | 263.26 | 124.18 |
| Average | 202.42 | 86.37 | 191.8 | 109.4 | 249.19 | 125.17 |

Table 3-2. CHF and MHF results under different system pressures for the diameter of 0.5 mm Ni-Cr wire

| System pressure | 1 bar | | 3 bar | | 5 bar | | 7 bar | | 9 bar | |
|---|---|---|---|---|---|---|---|---|---|---|
| | CHF | MHF | CHF | MHF | CHF | MHF | CHF | MHF | CHF | MHF |
| # 1 (kW/m$^2$) | 181.7 | 104.5 | 403.6 | 159.5 | 492.9 | 175.2 | 515.5 | 230.2 | 644 | 230.1 |
| # 2 (kW/m$^2$) | 197.3 | 101.4 | 447.3 | 156.5 | 474.2 | 174.6 | 557.1 | 216.9 | 642 | 221.1 |
| # 3 (kW/m$^2$) | 196.5 | 122.3 | 435.6 | 171.1 | 494.3 | 180.9 | 579.2 | 218.8 | 578.7 | 277.9 |
| #4 (kW/m$^2$) | 214.2 | 101.2 | 446.1 | 166.9 | 514.2 | 178.1 | 569.7 | 224.6 | 638.4 | 262.7 |
| Average | 197.4 | 107.4 | 433.2 | 163.5 | 493.9 | 177.2 | 555.4 | 222.6 | 625.8 | 247.9 |

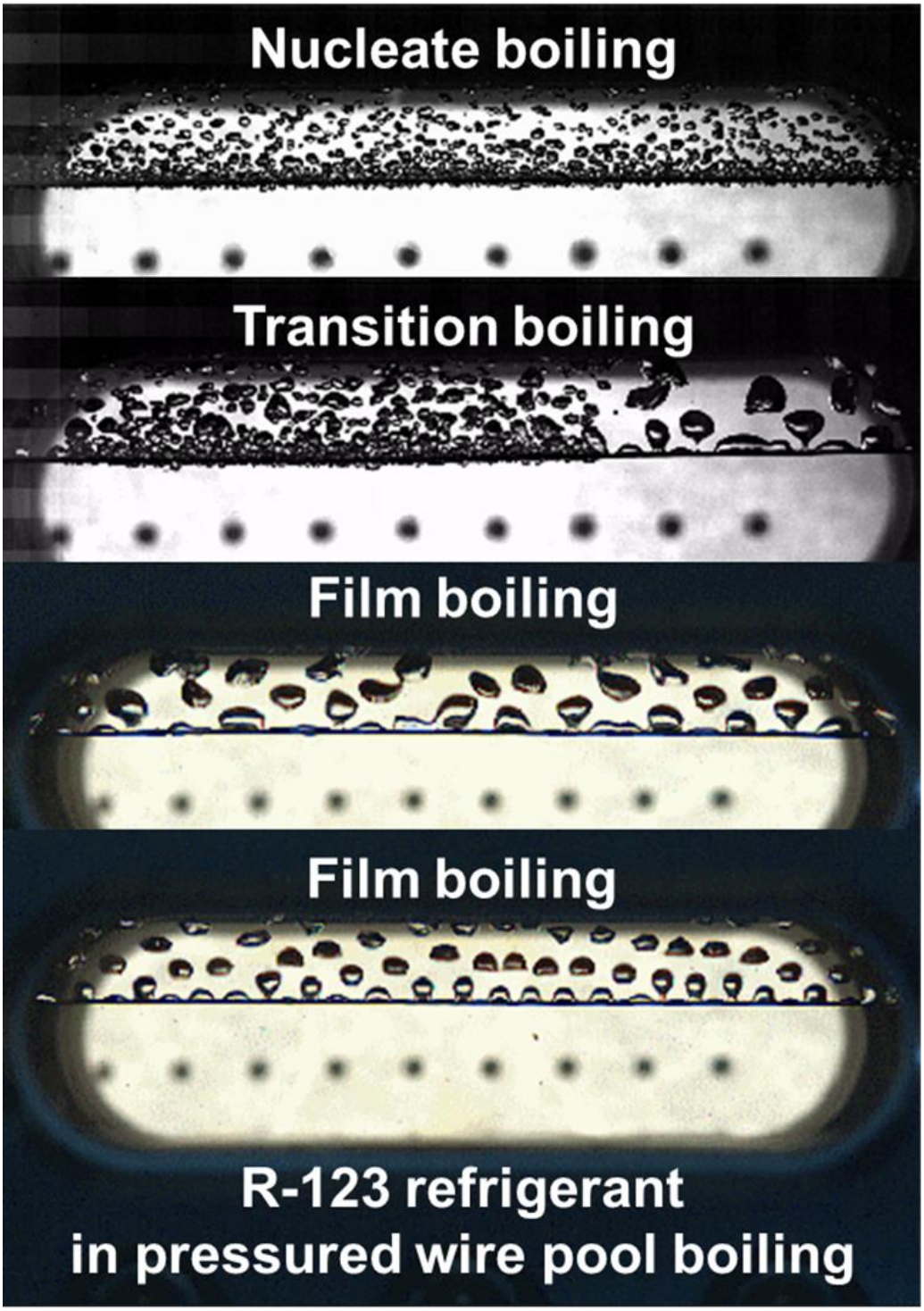


Fig. 3-5. Typical boiling observations

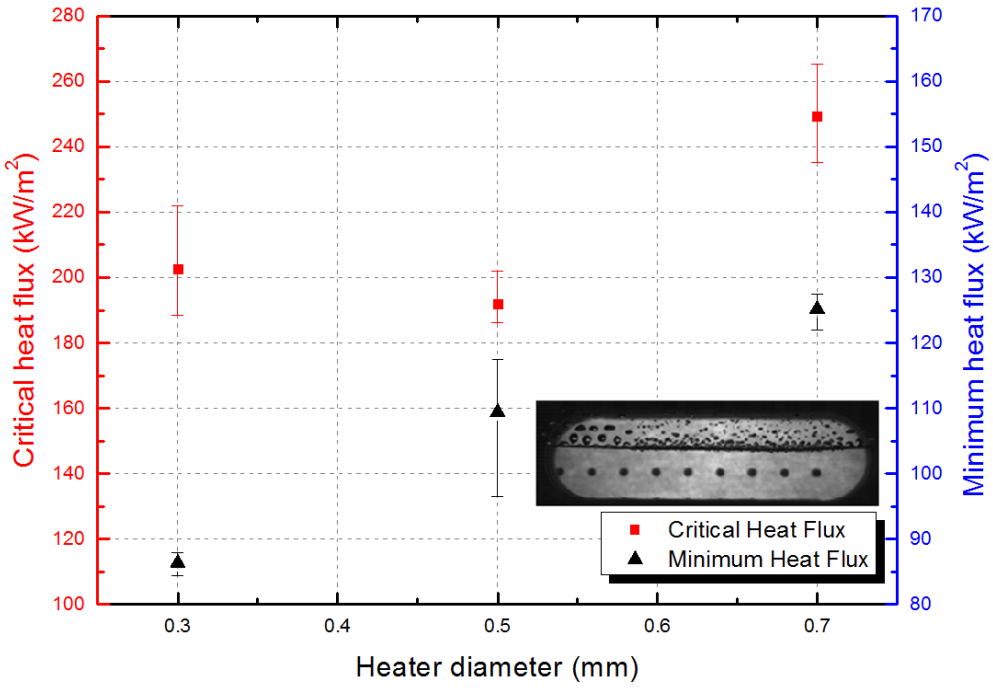


(a)

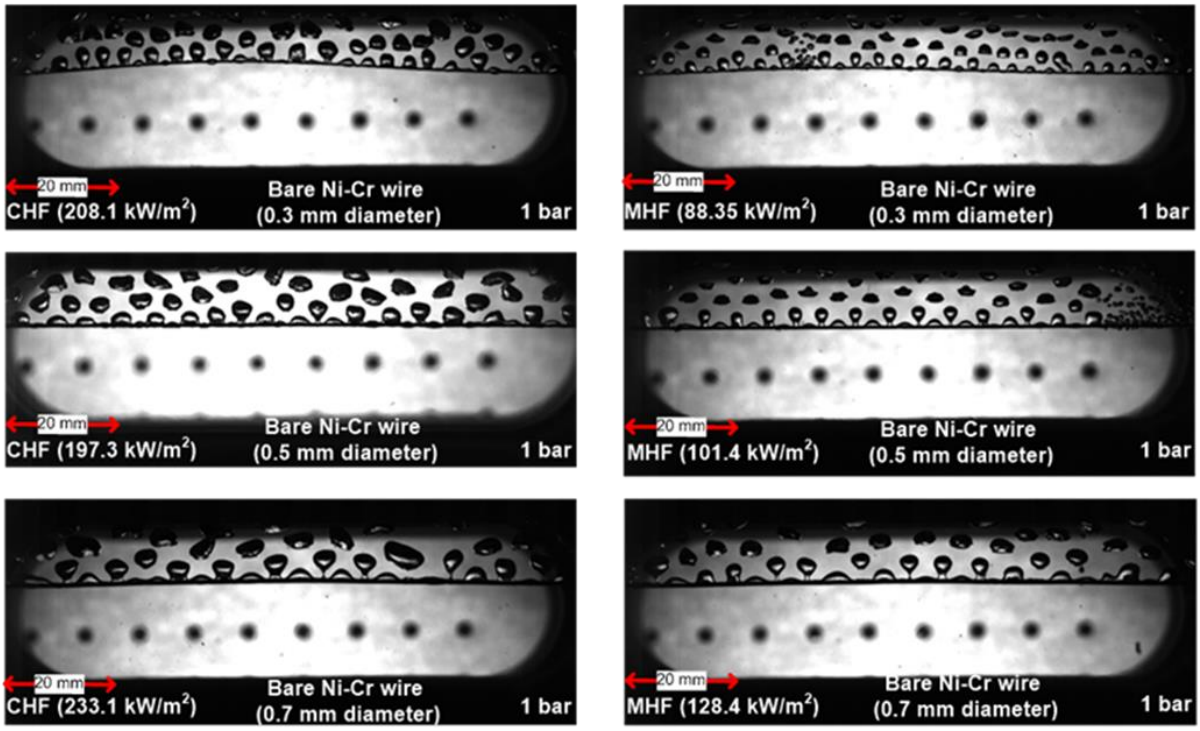


(b)

Fig. 3-6. Experimental results with various wire diameters: (a) CHF and MHF, (b) RT instability observations

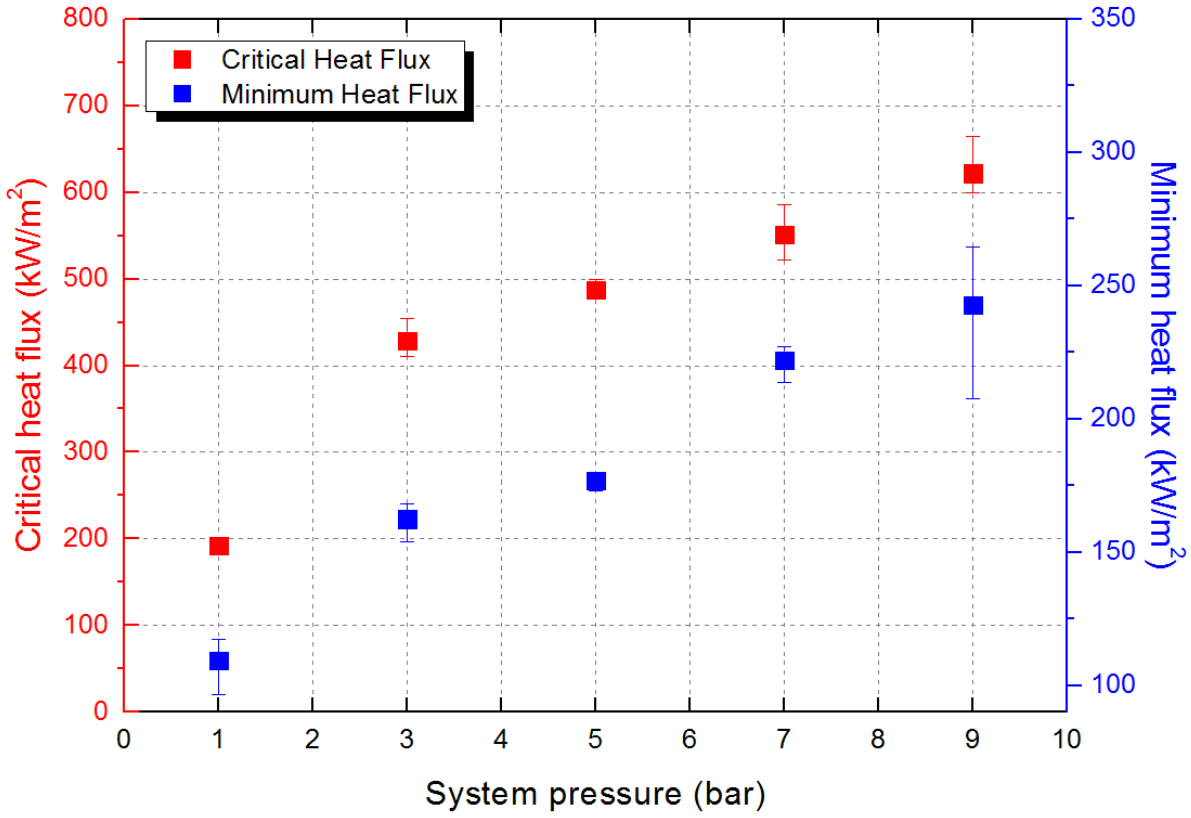


Fig. 3-7. CHF and MHF results for the 0.5 mm wire diameter


Fig. 3-8. Observation of RT instability wavelength at the points of CHF and MHF under various pressures

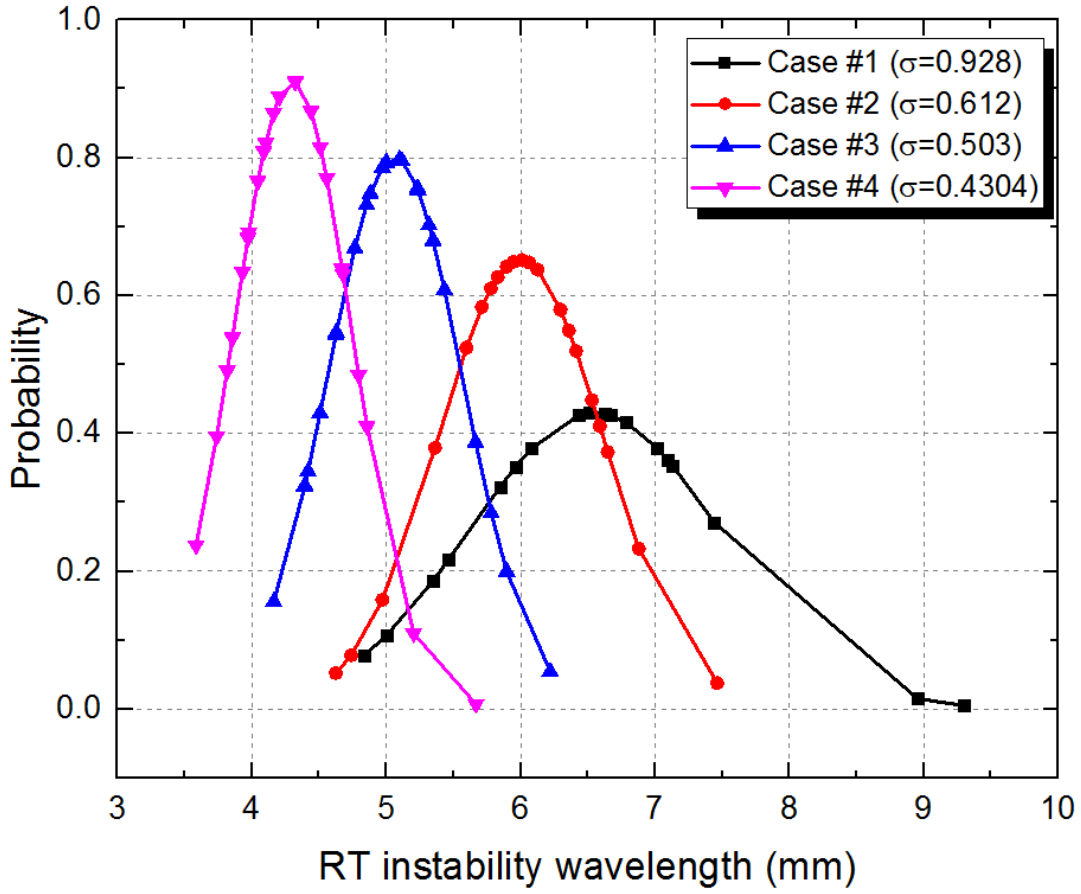


Fig. 3-9. Normal distributions of measured RT instability wavelengths

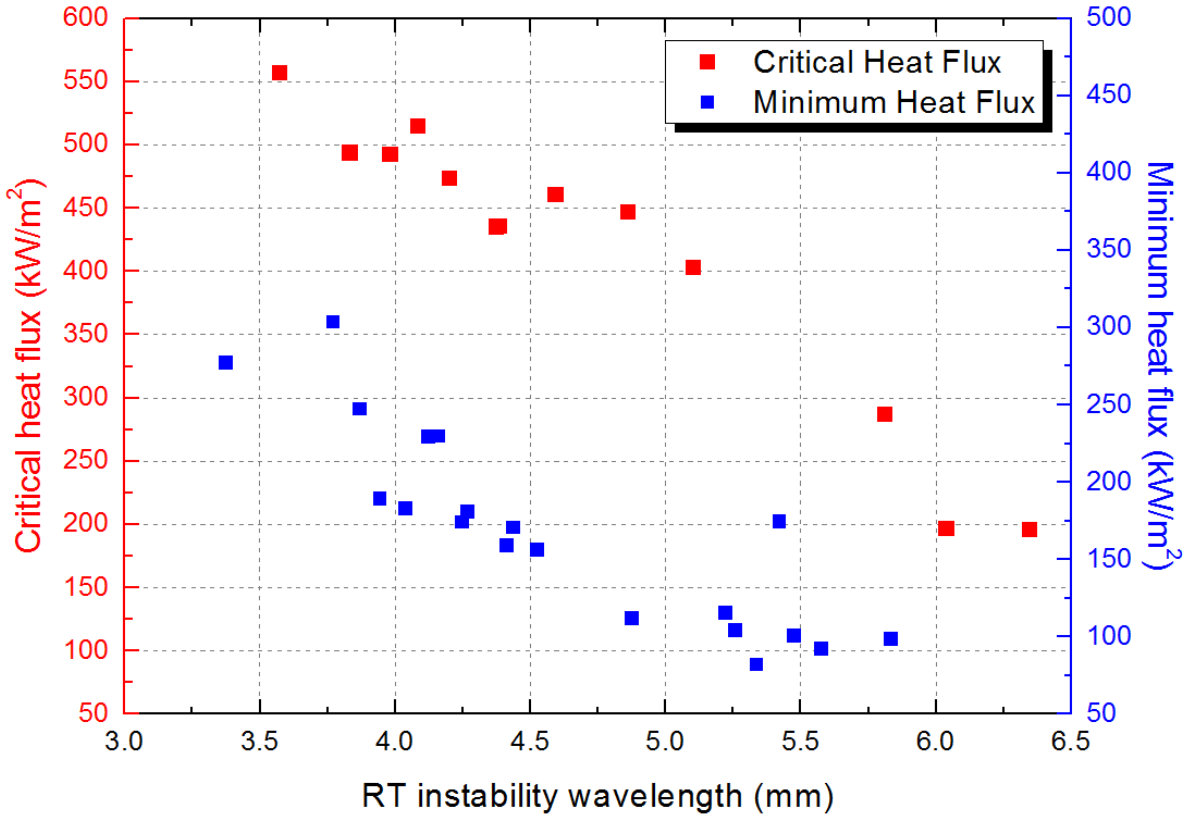


Fig. 3-9. CHF and MHF trends according to measured RT instability wavelengths

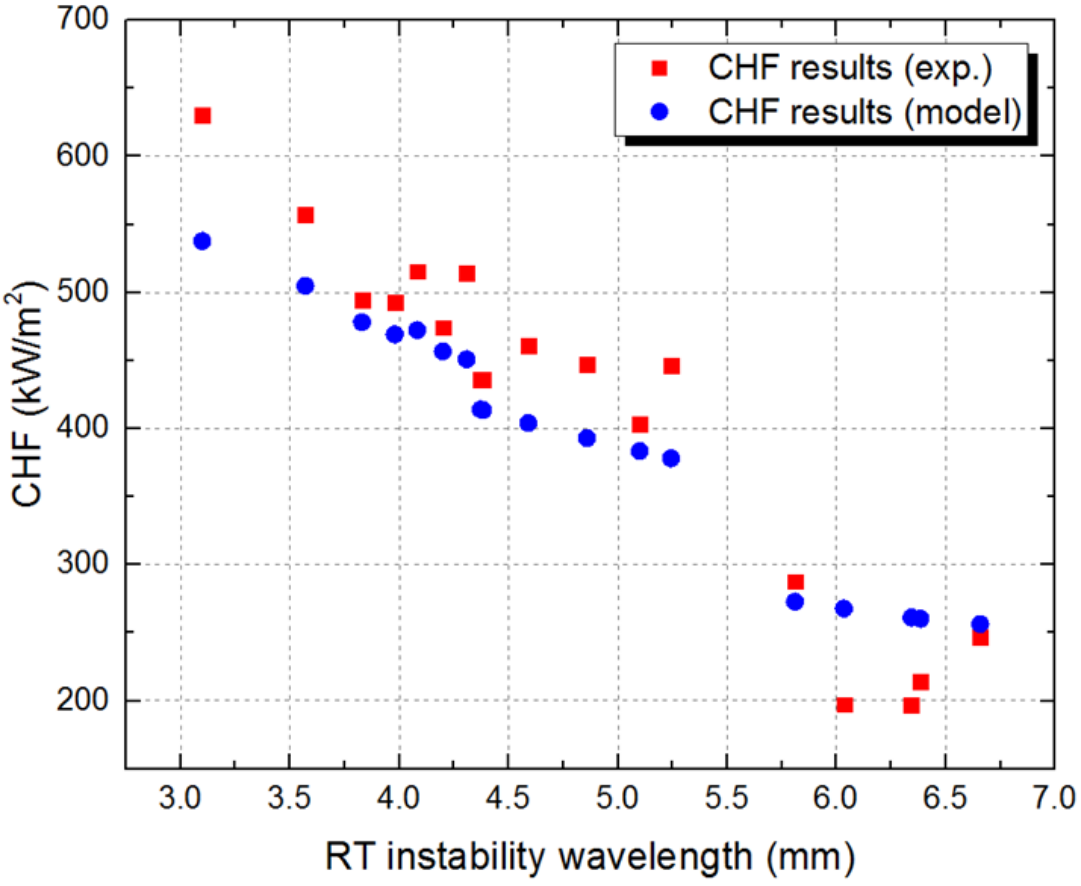


Fig. 3-10. The modified hydrodynamic instability model and the experimental results based on the measured RT instability wavelengths

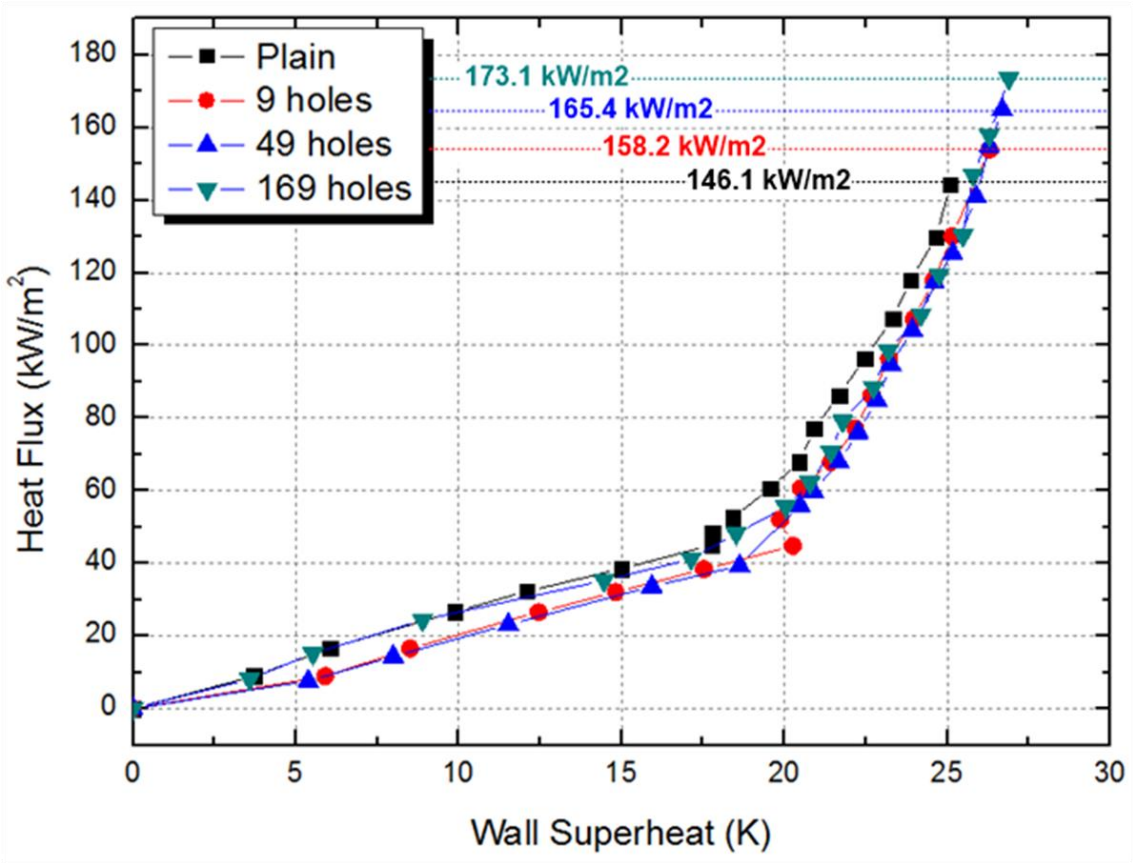


Fig. 3-11. Boiling curves for plain, 9-hole, 49-hole, and 169-hole Pt heating surfaces

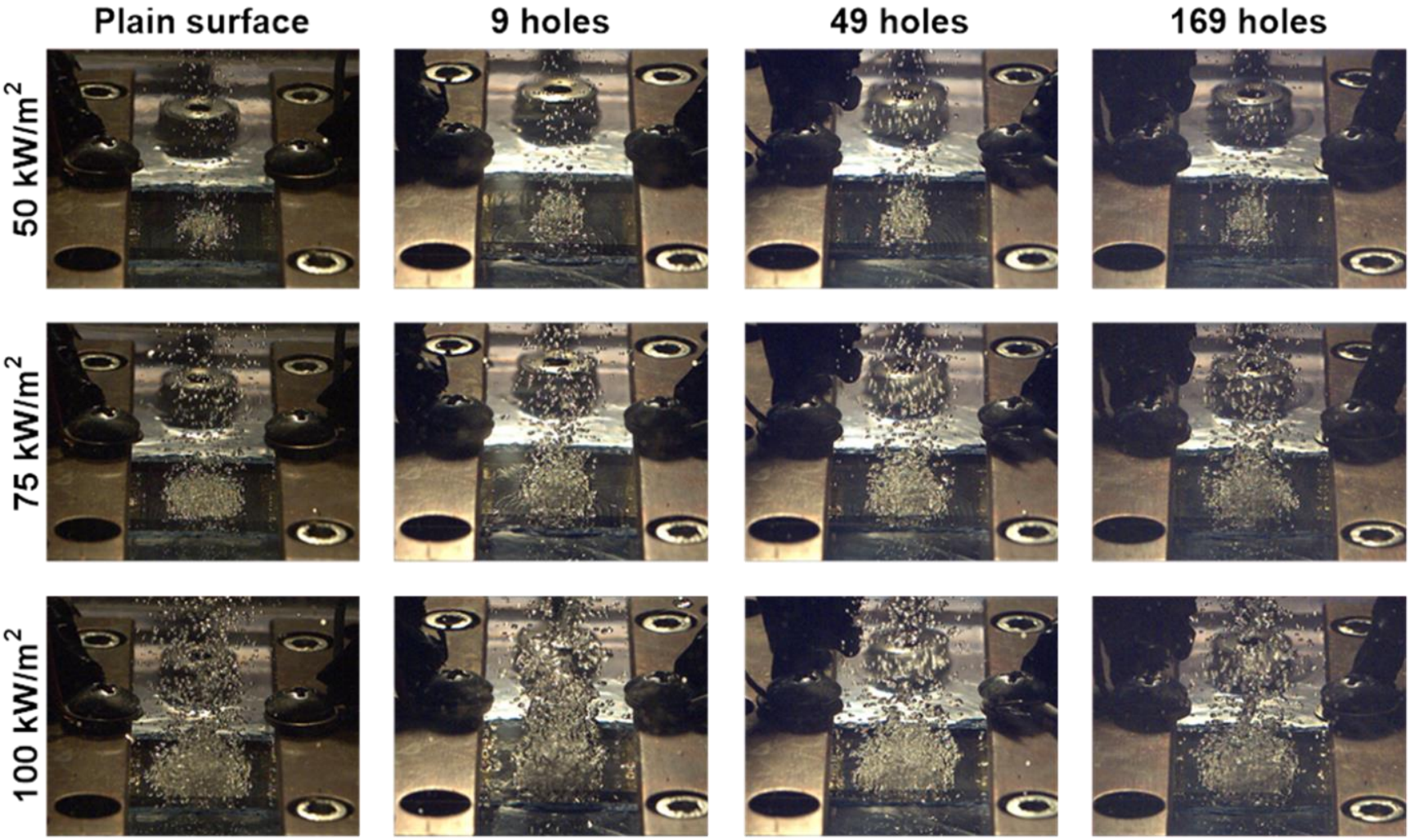


Fig. 3-12. Boiling observations at various heating surfaces with various heat flux conditions

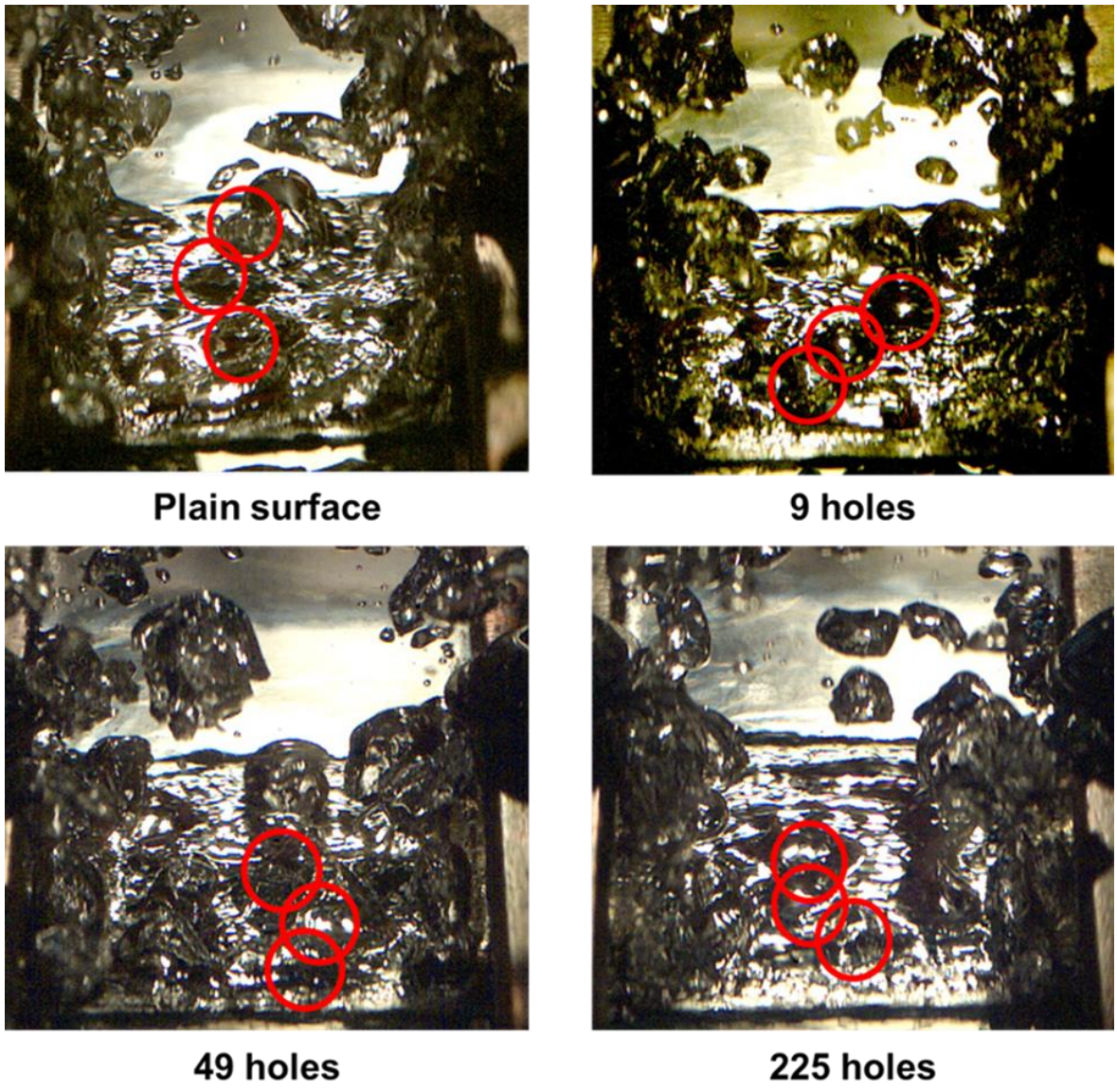


Fig. 3-13. RT instability observations at CHF regions

### 3.4 Conclusions

The experiments related to the hydrodynamic instability theory for the CHF prediction model were examined in various experimental conditions to find the appropriate way for developing the CHF enhancement mechanism model based on the hydrodynamic instability approach. The pressurized wire pool boiling experiments were performed to find the relation between the RT instability wavelength and the CHF, and the patterned Pt heating surfaces were conducted to show the change of the CHF results based on the change of the RT instability wavelengths. Following conclusions were obtained.

(1) The pressurized wire pool boiling facilities with various heater diameters and system pressures were considered to show the effect of surface characteristics on the CHF performance. For the effect of heater diameters, the RT instability wavelength was changed even though the CHF performance was similar measured by the diameter of 0.3, 0.5, and 0.7 mm Ni-Cr wire heating surface. The various system pressures were applied on the wire pool boiling with the diameter of 0.5 mm to show the tendency of the measured RT instability wavelengths with the CHF results: the CHF was increased when the RT instability wavelength was decreased, vice versa. The measured RT instability wavelengths were considered as the modulation wavelengths of the modified hydrodynamic approach model and the results showed that the change in CHF values can be explained by the change in the RT instability wavelength.

(2) The patterned Pt heating surfaces were examined in the plate pool boiling facility to show the CHF enhancement trend with the RT instability wavelengths. Because the patterning depth was 50 nm, the CHF enhancement for the 9 holes, 49 holes, and 225 holes heating surfaces was obtained as 8.3%, 13.2%, and 18.5%, compared to the plain heating surface, respectively. The measurement of the RT instability wavelengths at the CHF region indicated that the wavelengths were decreased when the CHF values were increased. This means that the change of the RT instability wavelengths was also valid in the plate pool boiling facility. The tendency of the CHF results based on the surface patterning distance was proposed.

The main conclusion from the experiments was to find the relation between the RT instability wavelength and the CHF performance. The results indicated that the RT instability wavelength should consider the surface characteristics such as using the surface curvature function in the prediction of the RT instability wavelength because the change of the RT instability wavelengths can accommodate all heating surface parametersIn the next chapter, therefore, the change of the RT instability wavelength will be discussed. Previous studies related to the CHF models based on the hydrodynamic instability theory were mentioned to show the difference between the existed CHF models and the proposed CHF model. Based on the proposed CHF model, validation procedure is conducted by using the existing experimental data with the effect of the measured RT instability wavelengths and the surface roughness factors.

# Chapter 4. MODIFIED HYDRODYNAMIC INSTABILITY CHF PREDICTION MODEL

## 4.1 Introduction

There have been a lot of research related to the CHF prediction models because the accurate prediction models could provide safety margin of power devices. For nuclear reactors, the operating safety margin of the nuclear reactors can be enhanced by eliminating an uncertainty range of the CHF prediction. Therefore, various kinds of CHF models with several prediction theories have been proposed such as hydrodynamic instability, macrolayer dryout, hot/dry spot, bubble interaction, bubble force balance, etc. Among the prediction models, the hydrodynamic instability theory has been widely used in industrial and research fields because the model was simplified to the working fluid properties. However, the accuracy of the hydrodynamic instability theory was decreased due to the CHF enhancement studies, which considered the effect of the surface modifications. This means that the hydrodynamic instability theory proposed by Zuber[22] did not consider any heating surface characteristics. He only considered the ideal case: infinite heating surface without any cavities. Based on the infinite heating surface condition, the relation between the RT and KH instability wavelengths was assumed and the CHF prediction model was developed. To deal with the surface characteristics, various experimental and prediction studies have been performed to consider the surface effects on the hydrodynamic instability theory. But the modified models were mostly limited to their experimental results. In this chapter, therefore, various kinds of CHF prediction models were introduced with the modified methods to improve the CHF prediction models. In addition, the modified hydrodynamic instability CHF model was proposed based on the change of RT instability wavelength; the change of the RT instability wavelengths influences on the critical vapor velocity. To validate the present model, the measured data obtained from the present experiments and the literatures were used.

## 4.2 Reviews of Hydrodynamic Instability Theory CHF Models

The CHF prediction model based on the hydrodynamic instability was proposed by Zuber[22]. When an applied heat flux on heating surface was increased with vigorous boiling, the liquid could not penetrate into the heating surface due to the aggressive vapor formation. He elucidated the CHF phenomenon as the result of the critical vapor velocity. The CHF model is derived from the point of vapor generation on a heating surface.

$$q \equiv m_v h_{lv} \qquad (4\text{-}1)$$

where $m_v$ and $h_{lv}$ are vapor mass velocity and latent heat of a working fluid. Because the vapors are

generated at a certain area on the heating surface, the CHF can be calculated by using the vapor velocity and density, latent heat, and the ratio of the vapor generation area (vapor columns) compared to the heating surface.

$$q''_{CHF} \equiv u_{v,c}\rho_v h_{lv}\frac{A_v}{A_h} \qquad (4\text{-}2)$$

where $u_{v,c}$, $\rho_v$, and $A_v/A_h$ are the critical vapor velocity, vapor density, and the area ratio of the vapor columns compared to the hole heating surface. The area of the vapor was defined by the vapor column formation on the heating surface at film boiling region because the observation of the vapor area ratio at the nucleate boiling is difficult due to the vigorous boiling occurrence. The area of the vapor column was calculated by the concept of the RT instability wavelength which was influenced by the density difference between the liquid and the vapor phases. Fig. 4-1 illustrates the RT instability wavelength on a heating surface. The diameter of the vapor column was assumed as the half of the RT instability wavelength, thus the area ratio of the vapor columns on the heating surface is

$$\frac{A_v}{A_h} = \frac{\pi\left(\lambda_{RT}/4\right)^2}{\lambda_{RT}^2} = \frac{\pi}{16} \qquad (4\text{-}3)$$

$$q''_{CHF} \equiv u_{v,c}\rho_v h_{lv}\frac{A_v}{A_h} = \frac{\pi}{16}u_{v,c}\rho_v h_{lv} \qquad (4\text{-}4)$$

As Eq. 4-4 shows, the CHF phenomenon can be determined by the critical vapor velocity by assuming the vapor column diameter as the half of the RT instability wavelength. The critical vapor velocity can be determined by the interfacial phenomenon driven by the velocity difference between the liquid and vapor. This means that KH instability wavelength reflected the critical vapor velocity. If the KH instability wavelength is decreased, the critical vapor velocity will increase, vice versa. The relation of the KH instability and the critical vapor velocity can be derived from the interfacial instability phenomenon.

$$u_{v,c} = \sqrt{\frac{2\pi\sigma}{\rho_v\lambda_{KH}}}\sqrt{\frac{\rho_l+\rho_v}{\rho_l}} \qquad (4\text{-}5)$$

In the hydrodynamic instability theory proposed by Zuber, the KH instability was considered as the RT instability. The concept of the KH instability wavelength was derived from the liquid drop experiment

with a certain hole. The ideal condition was assumed for measuring the KH instability wavelength. If the hole was modified, the KH instability wavelength will be changed based on the modified the hole. This inferred that the critical vapor velocity can be influenced by the surface modifications. Instead of measuring the KH instability wavelength, Zuber used the RT instability wavelength instead of the KH instability wavelength. By considering the KH instability is a function of RT instability wavelength, the classical CHF prediction model with the hydrodynamic instability approach is

$$q''_{CHF} = \frac{\pi}{24}\rho_v^{1/2} h_{lv} \sqrt[4]{\sigma g\left(\rho_l - \rho_v\right)} \qquad (4\text{-}6)$$

Based on the above CHF prediction model, various kinds of CHF models to predict the experimental results have been proposed.

Lienhard and Dhir[57] considered the infinite heating surface and small size of heating surface with various shapes. For the infinite and the finite heating surfaces, most dangerous wavelength was considered as the RT instability wavelength. For heating size effect, they argued that the variation heating size can affect the CHF via reducing the number of vapor columns presented on the heating surface. As the number of vapor columns is confined by the size of the heating surface, the area ratio would be modified. The KH instability wavelength for the infinite and the finite heating surfaces was assumed as the most dangerous RT instability and the circumference of the heating surfaces, respectively.

$$q''_{CHF} = 0.149\rho_v^{1/2} h_{lv} \sqrt[4]{\sigma g\left(\rho_l - \rho_v\right)} \quad \text{(infinite heating condition)} \qquad (4\text{-}7)$$

$$q''_{CHF} = 1.14 \times q_{CHF,Z} \times \left(\frac{N_j \times \lambda_D}{A_h}\right) \quad \text{(finite heating condition)} \qquad (4\text{-}8)$$

Liter and Kaviany[9] manufactured porous heating surfaces by controlling distance of the deposition modulation wavelength: modulation wavelength is determined by the heating surface conditions. The modulation wavelength changes the RT instability wavelength, thus the CHF can be changed by the modulation wavelength. Based on the modulation wavelength, the KH instability wavelength was also introduced by the geometrically determined wavelength.

$$\lambda_{KH} = 2\pi a\lambda_m = 9a\lambda_{RT,c} \qquad (4\text{-}9)$$

where a, $\lambda_m$ and $\lambda_{RT,c}$ are the constant, modulation wavelength by the heater geometry, and critical RT instability wavelength. By comparing the Zuber's model, the CHF prediction model by the modulation

porous heating surfaces can be derived as

$$\frac{q''_{CHF,h}}{(\pi/24)h_{lv}\rho_v^{1/2}\sqrt[4]{\sigma g(\rho_l-\rho_v)}}=\left(\frac{9}{2\pi}\frac{\lambda_{RT,c}}{\lambda_m}\right)^{1/2} \quad (4\text{-}10)$$

$$q''_{CHF,h}=\frac{\pi}{8}h_{lv}\left(\frac{\sigma\rho_v}{\lambda_m}\right)^{1/2} \quad (4\text{-}11)$$

Lu et al.[58-59] used microstructure surfaces to show the CHF enhancement which was attributed by the change of heating surfaces. Because the heating sizes were infinite conditions, the KH instability was considered as the function of the size of heating surfaces. To predict their experimental results with the hydrodynamic instability approach, the area ratio of vapor column was supposed to the fitting constant. In addition, Lee and Lee[60] used small size of PCB heaters where the prediction model proposed by Lienhard and Dhir[57] could not predict the experimental range. They considered that RT instability could be changed by the heating size conditions and KH instability wavelength was the same as the model proposed.

$$\frac{q''_{CHF}}{q''_{CHF,Z}}=\frac{24}{\pi}\eta\sqrt{\frac{2\pi\Lambda}{2\sqrt{0.155\pi w\lambda_d f(w')}}}\times 0.155=1.383\eta\left(w'f(w')\right)^{-1/4} \quad (4\text{-}12)$$

where η, Λ, w’ are the correcting factor, Laplace length, and the width of thin flat plate heater divided by the Laplace length.

Jun et al.[61] changed the KH instability to predict the experimental CHF results. The experiment was conducted with nano-textured surfaces with various working fluids. Compared to the Zuber’s model, the prediction value was higher than 38.9%.

$$\lambda_{KH}=\frac{3\pi\sigma}{\rho_v u_v^2} \quad (4\text{-}13)$$

$$q''_{CHF}=0.182h_{lv}\rho_v^{1/2}\sqrt[4]{\sigma g(\rho_l-\rho_v)} \quad (4\text{-}14)$$

Park and Bang[11] observed the change of RT instability with the nanoparticle-coated surfaces. Various kinds of nanoparticle-coated surfaces were examined in the wire pool boiling facility with the water and the observation of RT instability wavelengths was measured under the R-123 refrigerant. Based on the change of RT instability wavelengths with respect to CHF results, a correlation was proposed based

on the Zuber's model.

$$q_Z'' : q_{CHF}'' = \left(\frac{\lambda_{th}}{\lambda_{bare}}\right)^n : \left(\frac{\lambda_{th}}{\lambda_m}\right)^n \qquad (4\text{-}15)$$

where $\lambda_{th}$, $\lambda_{bare}$, $\lambda_m$ are theoretical value, measured in bare Ni-Cr wire surface, and measured the change of the RT instability wavelengths, respectively. But the correlation by measuring the RT instability wavelengths under the R-123 refrigerant is not applicable in other studies because the CHF enhancement results were obtained by using the water.

Because the hydrodynamic instability theory did not consider the effect of viscous of the working fluid, there was a study to show the influence of the RT instability for thin viscous gas films on the CHF and MHF performances[62]. Based on stability analysis, the most dangerous wavelength was modified.

$$\lambda_d = \sqrt{2}\lambda_c = 2\sqrt{2}\pi\left[\sigma/\left(g\Delta\rho\right)\right]^{1/2} \qquad (4\text{-}16)$$

$$q_{CHF}'' = 0.165\frac{\left(16-\pi\right)\rho_v}{\pi\rho_l + \left(16-\pi\right)\rho_v}\rho_v^{1/2}h_{lv}\sqrt[4]{\sigma g\Delta\rho}\left(1+\rho_v/\rho_l\right)^{-1/2} \qquad (4\text{-}17)$$

$$q_{CHF}'' = 0.271\rho_l^{1/2}h_{lv}\sqrt[4]{\sigma g\Delta\rho}\left(1+\rho_v/\rho_l\right)^{1/4}\left(\rho_v/\rho_l\right)^{1/10} \qquad (4\text{-}18)$$

If the viscosity effect is neglected for thin gas films, the most dangerous wavelength and the most rapid growth rate are incorrectly predicted. But the viscosity effect on the instability wavelength is only influenced on the most dangerous RT instability wavelength. This means that there would be no effect on the CHF performance when the critical RT instability wavelength is suggested as the vapor column spacing.

The bubble force balance model introduced by the Kandlikar[50] is similar to the hydrodynamic instability theory because the RT instability wavelength was used with positioning of the bubbles on a heating surface. This means that the additional surface parameter of wettability was considered in the bubble force balance model compared to the Zuber's model. The heat flux on the heating surface was determined by the ratio of heat flux of evaporation of the average bubble height and bubble interface divided by influence area.

$$q'' = \frac{q_I''\cdot\left(D_{avg}/2\right)\left(1+\cos\beta\right)\cdot\left(\pi D_{avg}/2\right)}{\pi/4\left(2D_b\right)^2} = \frac{1+\cos\beta}{16}q_I'' \qquad (4\text{-}19)$$

$$q_l'' = \rho_v^{1/2} h_{lv} \left( \frac{\sigma(1+\cos\beta)}{H_b} + \frac{1}{2} g(\rho_l - \rho_v) H_b \cos\phi \right) \quad (4\text{-}20)$$

$$q_{CHF}'' = h_{lv} \rho_v^{1/2} \left( \frac{1+\cos\beta}{16} \right) \left[ \frac{2}{\pi} + \frac{\pi}{4}(1+\cos\beta)\cos\phi \right]^{1/2} \left[ \sigma g(\rho_l - \rho_v) \right]^{1/4} \quad (4\text{-}21)$$

where $q_l''$, $D_{avg}$, $D_b$, $H_b$, $\beta$, $\Phi$, are the heat flux due to the evaporation, bubble average diameter, bubble influence diameter, bubble height, receding angle, and heater orientation angle, respectively. Based on the Kandlikar's model, the CHF enhancement model was proposed when the heating surface exhibited superhydrophilic surfaces[63].

$$q_{CHF}'' = h_{lv} \rho_v^{1/2} \left( \frac{1+\cos\theta}{16} \right) \left[ \frac{2}{\pi} \frac{1+r\cos\beta}{1+\cos\theta} + \frac{\pi}{4}(1+\cos\theta)\cos\phi \right]^{1/2} \left[ \sigma g(\rho_l - \rho_v) \right]^{1/4} \quad (4\text{-}22)$$

The model used the apparent contact angle as well as receding angle to consider the hydrophilicity at the static contact angel measurement. The CHF results of micropillar heating surfaces were well predicted by the modified CHF model and additional experiments with the hierarchically structured surfaces were performed to support the proposed CHF model[64]. Quan et al.[52] suggested a model based on the change of surface roughness in the bubble force balance model by using the effect of critical RT instability wavelength on smooth and rough surfaces. Additional capillary wicking term was considered in the bubble force balance model and the surface roughness term with the solid fraction was considered in the critical RT instability wavelength to show the change of the bubble spacing.

$$q_{CHF}'' = \left( \frac{1+\cos\beta}{16} \right) \left[ \frac{2}{\pi} \left(1-\sqrt{\phi_s}\right)^{-1/2} \frac{r+\cos\beta}{1+\cos\beta} + \frac{\pi}{4} \left(1-\sqrt{\phi_s}\right)^{1/2} (1+\cos\beta)\cos\phi \right]^{1/2} h_{lv} \rho_v^{1/2} \left[ \sigma g(\rho_l - \rho_v) \right]^{1/4} \quad (4\text{-}23)$$

where $\Phi s$ is the solid fraction. This model includes the effect of surface roughness and surface wettability, thus various kinds of experimental results could be predicted. Table 4-1 lists the CHF models based on the hydrodynamic instability theory.

Several kinds of CHF models related to the hydrodynamic instability theories were discussed based on the control parameter of the hydrodynamic instability theory. Table 4-2 shows the control parameters in the hydrodynamic instability CHF model: critical vapor velocity, RT instability wavelength, and the ratio of the vapor column on heating surfaces. The critical vapor velocity was determined by the RT instability wavelength because of the relation of the KH instability wavelength. When the surface characteristics were changed, the RT instability wavelength can be changed which the critical vapor velocity was also changed. Therefore, the effect of surface curvatures on the RT instability wavelength

is discussed and the modified hydrodynamic instability CHF model is proposed by considering the effect of surface roughness and measured RT instability wavelength.

Table. 4-1. CHF models based on hydrodynamic instability theory

| Surface Conditions | Models | Description | Denote |
|---|---|---|---|
| Infinite flat heater | Zuber (1959) | $q''_{CHF,z} = \frac{\pi}{24}\rho_v^{1/2} h_{lv} \sqrt[4]{\sigma g(\rho_l - \rho_v)}$ | $\lambda_{RT,c\ or\ d} = \lambda_{KH}$ with numerical constant |
| | Lienhard and Dhir (1973) | $q''_{CHF} = 1.14 q''_{CHF,z}$ | $\lambda_{RT,D}=\lambda_{KH}$ |
| | Liter and Kavinay (2001) | $q''_{CHF} = q''_{CHF,z} \times \left(\frac{9}{2\pi}\frac{\lambda_{RT,c}}{\lambda_m}\right)^{1/2} = \frac{\pi}{8} h_{lv}\left(\frac{\sigma\rho_v}{\lambda_m}\right)^{1/2}$ | Modulation wavelength |
| | Kandlikar (2002) | $q''_{CHF} = q''_{CHF,z}\frac{24}{\pi}\left(\frac{1+\cos\beta}{16}\right)\left[\frac{2}{\pi}+\frac{\pi}{4}(1+\cos\beta)\cos\phi\right]^{1/2}$ | Wettability effect |
| | Hwang and Kavinay (2006) | Suggest change of wavelength and fraction area covered by vapor | The methods of changing hydrodynamic CHF model |
| | Chu et al. (2012) | $q''_{CHF} = q''_{CHF,z}\frac{24}{\pi}\left(\frac{1+\cos\beta}{16}\right)\left[\frac{2}{\pi}\frac{1+r\cos\theta_{rec}}{1+\cos\beta}+\frac{\pi}{4}(1+\cos\beta)\cos\phi\right]^{1/2}$ | Roughness in bubble force balance |
| | Jun et al. (2013) | $q''_{CHF} = 1.39 q''_{CHF,z}$ | KH instability wavelength change |
| | Quan et al. (2014) | $q''_{CHF} = q''_{CHF,z}\frac{24}{\pi}\left(\frac{1+\cos\beta}{16}\right)\left[\frac{2}{\pi}\left(1-\sqrt{\phi_s}\right)^{-1/2}\frac{r+\cos\beta}{1+\cos\beta}+\frac{\pi}{4}\left(1-\sqrt{\phi_s}\right)^{3/2}(1+\cos\beta)\cos\phi\right]^{1/2}$ | Solid fraction & roughness |
| | Kim et al. (2015) | $q''_{CHF} = 2.06\left(1+\frac{\rho_v}{\rho_l}\right)^{1/4}\left(\frac{\rho_v}{\rho_l}\right)^{1/10}$ | Consider viscous effect |
| Small flat heater | Lienhard and Dhir (1973) | $q''_{CHF} = 1.14\frac{\lambda_{RT}}{A_h} q''_{CHF,z}$ | $10 < L' < 20$ |
| | Lu et al., (2011 & 2015) | $q''_{CHF,z} = \sqrt{\frac{2\pi\sigma}{\rho_v\lambda_{KH}}}\rho_v h_{lv}\frac{A_j}{A_h}$ $\lambda_{KH} = heater\ size$ $A_j/A_h = fitting\ \ factor$ | Small heater size<br>Nanowire & micropillar surface |
| Horizontal cylinder | Lienhard and Dhir (1973) | $\frac{q''_{CHF}}{q''_{CHF,Z}} = 0.94(R')^{-1/4}$ $\frac{q''_{CHF}}{q''_{CHF,Z}} = 0.9$ | $0.15 < R' < 1.2$ & $1.2 < R'$ |
| | Park and Bang (2014) | $q''_{CHF} = \left(\frac{\lambda_{bare}}{\lambda_{th}}\right)^n \propto \left(\frac{\lambda_{th}}{\lambda_m}\right)^n q''_{CHF,z}$ | $R'_{bare} = 1.02$ |
| Small ribbon heater | Lienhard and Dhir (1973) | $q''_{CHF} = 1.18(w')^{-1/4} q''_{CHF,z}$ | $0.15 < w'$ |
| | Lee and Lee (2015) | $q''_{CHF} = 1.383\eta(w' f(w'))^{-1/4} q''_{CHF,z}$ | $w' < 0.15$ |

Table. 4-2. Control parameters in hydrodynamic instability theory

| Parameter | Description |
|---|---|
| $u_v$ | KH instability wavelength is the main parameter |
| $\lambda_{RT}$ | RT instability wavelength can be influenced by the heating surface conditions |
| $A_v/A_h$ | As the ratio of the vapor columns increases, the CHF will be increased |

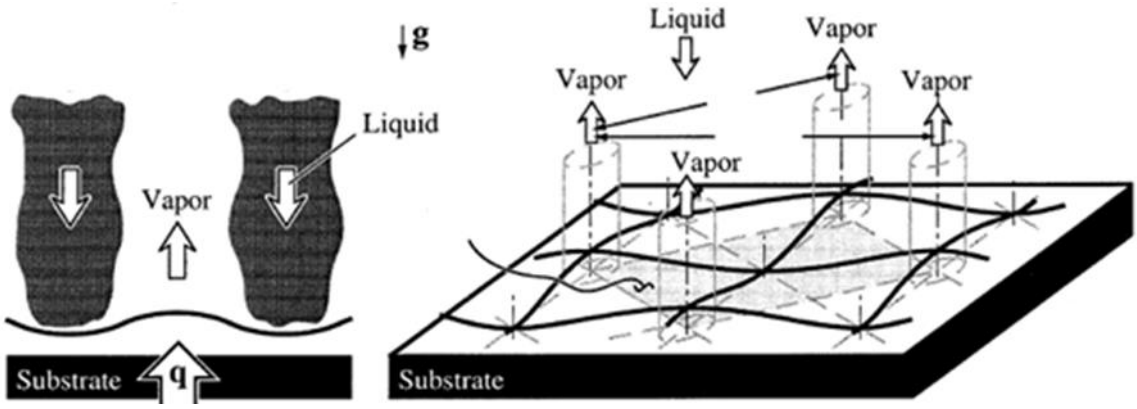


Fig. 4-1. RT instability wavelength on a heating surface[9]

### 4.3 CHF Modeling with Change of RT Instability Wavelength

The hydrodynamic method can be applied to the surface medication heating surfaces which induced the change of CHF prediction values. Eq. 4-2 is the peak heat flux as the latent energy transfer and eq. 4-6 is the CHF model presented by Zuber[22]. The modified CHF model can be obtained by combining eqs. 4-2 and 4-6.

$$\frac{q''_{CHF}}{q''_{CHF,z}} = \frac{u_{v,c} h_{lv} \rho_v \dfrac{A_v}{A_h}}{\dfrac{\pi}{24} \rho_v^{1/2} h_{lv} \sqrt[4]{\sigma g \left(\rho_l - \rho_g\right)}} = \frac{24}{\pi} \frac{A_v}{A_h} \sqrt{\frac{2\pi}{\lambda_{KH} \sqrt{g\left(\rho_l - \rho_g\right)/\sigma}}} \qquad (4\text{-}24)$$

The major influence parameters in eq. (4-24) are the KH instability wavelength and the ratio of the vapor columns on the heating surface. The main concept of the modified hydrodynamic approach is to change the critical vapor velocity: the change of the KH instability or RT instability wavelengths influence on the critical vapor velocity. The wire pool boiling experiments revealed that the change of the RT instability follows the change of the CHF performance. This inferred that the RT instability is the criterion that predicts the CHF. Therefore, the change of the RT instability wavelength due to the surface modifications should be determined. In the present research, the function of surface characteristics is considered in the RT instability wavelength.

$$\lambda_{RT,c} = 2\pi \sqrt{\frac{\sigma}{g\left(\rho_l - \rho_v\right)}} a\left(f\left(k\right)\right)^n \qquad (4\text{-}25)$$

where f(k) is a function of surface characteristics that can influence on the change of the RT instability wavelength. The surface characteristics can be measured RT instability wavelength, surface roughness, etc. By considering the modified RT instability wavelength in eq. 4-24, the modified CHF trend can be obtained.

$$\lambda_{KH} = 2\pi R_v = \frac{\pi}{2} \lambda_{RT,c} = \pi^2 \sqrt{\frac{\sigma}{g\left(\rho_l - \rho_v\right)}} a\left(f\left(k\right)\right)^n \qquad (4\text{-}26)$$

$$\frac{q''_{CHF}}{q''_{CHF,z}} = c\left(f\left(k\right)\right)^{-0.5n} \qquad (4\text{-}27)$$

$$q''_{CHF} = q''_{CHF,z} c\left(f\left(\kappa\right)\right)^{-0.5n} \qquad (4\text{-}28)$$

Based on the modified CHF model, the change of RT instability due to the heater width or the surface characteristics will change the critical vapor velocity: CHF is depended on the change of RT instability wavelength. The modified hydrodynamic CHF model based on the function of surface characteristics will have the form as eq. 4-28. In the present work, the measured RT instability wavelengths and the surface roughness factors were considered in the modified hydrodynamic CHF model.

$$f(\kappa) = \left( \frac{\lambda_{measured}}{\lambda_{RT,c}} \right)^2 \qquad \text{(4-29a)}$$

$$f(\kappa) = \left( \frac{r_p}{r_{ac}} \right) \qquad \text{(4-29b)}$$

### 4.4 Comparison between Modified Hydrodynamic Instability Model and Experimental Data

To compare the modified hydrodynamic CHF model with the existing experimental data, various kinds of experiments were considered. For the RT instability factor in the modified hydrodynamic CHF model, the RT instability factor was defined as eq. 4-29a. The obtained and additional CHF results which considered the effect of the RT instability wavelength were used to validate the modified hydrodynamic CHF model. The experimental data related to the RT instability wavelength factor were 24 including the previous works and the additional experiments with the nanoparticle-deposition surfaces on the Ni-Cr wire surfaces using FC-72 refrigerant. There was a study using various nanoparticle-deposition surfaces on the Ni-Cr wire surfaces to show the CHF enhancement with the effects of the measured RT instability wavelengths[11]. Application of the experimental results was not appropriate because the RT instability observations were conducted in the R-123 refrigerant while the CHF enhancement ratio was obtained using the water. Therefore, the additional experiments were performed by using the various nanoparticle-deposition surfaces in the FC-72 refrigerant. Five kinds of nanoparticles were prepared and the deposition of nanoparticles on the Ni-Cr wire surface was conducted by boiling of 0.01 V% nanofluids at 700 $kW/m^2$ during 15 min. The CHF enhancement ratio of the nanoparticle-coated surfaces was compared to the bare Ni-Cr surface. For the bare Ni-Cr wire surface, the measured CHF was the 162.5 $kW/m^2$. Compared to the Zuber's prediction model (148.15 $kW/m^2$), the reliability of the experimental procedure with the bare Ni-Cr surface was confirmed by comparing the prediction model. For the nanoparticle-coated surfaces, the CHF enhancement ratio for the $Al_2O_3$, ZnO, SiC, CuO, and RGO was 29.7, 32.9, 28.3, 48.6, and 32.5 %, respectively. Compared to the Park and Bang's experimental data [11], the noticeable CHF enhancement was not observed, because the working fluid was different. Table 4-3 lists the CHF enhancement results by the nanoparticle-coated surface with the FC-72 refrigerant and Fig. 4-2 shows the comparison of the CHF enhancement ratio between the present experiment and Park and Bang's experimental data. In addition, the measurement of the RT instability wavelengths under various coated surfaces was performed to get the RT instability wavelength factor for the modified hydrodynamic CHF model. The condensation RT instability measurement was performed because the observation of the RT instability wavelengths at the CHF region was difficult because the vapors were agglomerated together. Fig. 4-3 exhibits the measurement of RT instability wavelengths with condensation method with various nanoparticle-coated surfaces. The average RT instability wavelengths for the bare Ni-Cir, $Al_2O_3$, ZnO, SiC, CuO, and RGO-coated surfaces were 4.923, 3.886, 3.779, 3.08, 3.439, and 3.494 mm, respectively. The RT instability wavelengths were decreased when the CHF enhancements were increased. The observation of the RT instability wavelengths and the CHF results were incorporated into the modified hydrodynamic CHF model for the validation works.

Park et al.[10] performed the wire pool boiling experiments with various nanofluids ($Al_2O_3$, graphene,

and graphene oxide) in water. The significant CHF enhancement was observed in the graphene and graphene oxide nanofluids even though the surface wettability and the capillarity were not improved. They focused on the CHF enhancement mechanism by the modulation wavelength due to the deposition of the nanoparticles on the heating surfaces. The condensation method to measure the change of the RT instability wavelength was performed and they insisted that the modulation of wavelength can sufficiently support the CHF enhancement mechanism[10]. Lee et al.[54] used two kinds of CuO nanofluids: one-step and two-step methods. One-step method means the fabrication of the nanofluid by a pulsed laser ablation and two-step method is the nanoparticles dispersion in the fluid. They found the superior CHF performance in the both CuO nanofluids compared to the bare Ni-Cr surface. Surface wettability, capillarity, and RT instability wavelength were considered as the CHF enhancement reasons, but they insisted that the RT instability wavelength can cover the all CHF enhancement mechanism by referring the results of CHF results with the graphene and graphene-oxide nanofluids[11]. Based on studies, 6 kinds of CHF enhancement results were collected and these experimental data were used in the validation procedure for the modified hydrodynamic CHF model. In chapter 3, there was the study for the CHF results and direct measurement of the RT instability wavelengths under various system pressures and heater diameters to find the relation between the RT instability wavelengths and the CHF performance. The results of the pressurized wire pool boiling experiments were also considered into the validation data for the modified CHF model: the total 28 data were evaluated as the RT instability wavelength factors. Based on eq. 4-29, the function of surface characteristics can be obtained. Fig. 4-4 exhibits the experimental data for the RT instability wavelengths. To find the value of n from the eq. 4-27, data fitting was conducted; the value of n was 0.25. Table 4-4 lists the RT instability factor, CHF experimental results, and CHF prediction values. The maximum deviation between the CHF results and the prediction values was 26.3%. The highest CHF enhancement was observed in the graphene oxide-coated surface with the value of 2.36. The RT instability factor of the graphene oxide coated surface was 28.7 with the CHF prediction value of 2.31. Most of CHF prediction values were similar to the experimental results. Fig. 4-5 indicates the comparison between the experimental CHF results and the prediction CHF values. The mean error (ME), MAE, and RMS error were 5.11, 8.25, and 5.35 %, respectively. Therefore, the prediction of the CHF enhancement with the measured RT instability wavelength is valid.

For the surface function as the roughness factor, it was defined as the ratio of the projected area to the actual surface area as indicated in eq. 4-29b. The total 27 roughness factors obtained from previous studies were considered into the modified CHF model[63-64,67-69]. Chu et al.[63] performed pool boiling experiments under micropillar surfaces fabricated on the Si wafer. Seven kinds of different surface roughness including the plain heating surface were considered by changing the height, diameter, and spacing of the micropillar structures. The surface enlargement ratio was varied from 1 to 5.94 and the CHF enhancement was observed using the water as working fluid. Further experiments were conducted

by using hierarchically structured surfaces on the micropillar surfaces[64]. The deposition of $SiO_2$ nanoparticles on the structured surfaces with an electrophoretic deposition technique was conducted to make the surface increment more than 6, compared to the plain heating surface. The highest surface expansion was 13.3 and this surface showed the highest CHF performance in the study. Wei and Honda[67] considered the effects of the height and thickness of micro-pin structures on boiling heat transfer with various dimensions of the square micro-pin surfaces. The dry etching method was used to fabricate the heating surfaces and the experiments were conducted with various liquid subcooling conditions using the FC-72 refrigerant. Because the modified CHF model considered the experiments at the saturated working fluid condition, the considered experimental results of the paper were the CHF results at the saturated condition. Dhilon et al.[68] fabricated micro/nano surface structures to maximize the CHF by changing the surface enlargement with controlling of the diameter and spacing for the structures. The working fluid was water and various CHF enhancements were observed, depending on the surface structures. Enhanced pool boiling performances were observed in the fabricated surface through femtosecond laser on stainless steel plates using the water as working fluid[69]. A 3D confocal laser scanning microscope was used to quantify the surface area ratio which was the total area of the microstructures divided by the projected area and the experimental results were discussed on the surface characteristics. Table 4-5 shows the surface enlargement, function of surface curvature based on the roughness factor, CHF enhancement, and CHF prediction values based on the modified hydrodynamic approach. The maximum surface enlargement was 13.3 and the following maximum CHF enhancement ratio obtained from the experiment was 2.19. The modified hydrodynamic CHF model with the surface roughness factor showed the maximum CHF enhancement prediction value was 1.91. Fig. 4-6 indicates the comparison between the experimental CHF results and the prediction CHF values. As Fig. 4-6 shows, most of data related to the surface enlargement were fitted in the range from -20% to 20% compared to the modified hydrodynamic CHF model with the surface roughness factor. The ME, MAE, and RMS error were -4.64, 12.6, and 11.9 %, respectively. The comparison results indicate that the modified hydrodynamic CHF model with the surface roughness factor can predict the CHF performance.

Table 4-3. Experimental results for nanoparticle-coated surface in FC-72 refrigerant

| Nanoparticle | CHF ($kW/m^2$) | CHF enhancement ratio |
|---|---|---|
| Bare Ni-Cr wire | 162.5 | |
| $Al_2O_3$ | 210.7 | 29.7% |
| ZnO | 215.9 | 32.9% |
| SiC | 208.6 | 28.3% |
| CuO | 241.5 | 48.6% |
| RGO | 215.4 | 32.5% |
| CHF prediction value (Zuber's model) = 148.15 $kW/m^2$ | | |

Table 4-4. CHF trends according to RT instability wavelength factor

| CHF validation through RT instability wavelength actor | | | | | | |
|---|---|---|---|---|---|---|
| Papers | RT instability factor | CHF experimental results (Enhancement ratio) | CHF prediction results (Enhancement ratio) | Deviation (%) | MAE (%) | RMS (%) |
| Park et al.. (2010) | 28.7 | 2.36 | 2.31 | 1.96 | 10.4 | 4.06 |
| | 24.1 | 2.15 | 2.21 | 2.93 | | |
| | 15.8 | 1.58 | 1.99 | 26.3 | | |
| Lee et al. (2012) | 24.2 | 2.06 | 2.22 | 7.67 | 9.88 | 1.45 |
| | 17.6 | 2.33 | 2.05 | 12.1 | | |
| Nanoparticle -coated exp. | 4.76 | 1.27 | 1.47 | 16.3 | 14.7 | 5.48 |
| | 5.03 | 1.33 | 1.49 | 12.6 | | |
| | 7.58 | 1.41 | 1.65 | 17.7 | | |
| | 6.08 | 1.49 | 1.57 | 5.39 | | |
| | 5.89 | 1.283 | 1.56 | 21.4 | | |
| PWPBF exp. | 2.83 | 1.14 | 1.29 | 13.2 | 5.26 | 1.15 |
| | 3.63 | 1.48 | 1.38 | 6.76 | | |
| | 3.84 | 1.33 | 1.40 | 5.26 | | |
| | 4.23 | 1.48 | 1.43 | 3.38 | | |
| | 5.19 | 1.44 | 1.51 | 4.86 | | |
| | 5.22 | 1.45 | 1.51 | 4.14 | | |
| | 4.04 | 1.36 | 1.42 | 4.41 | | |
| | 4.58 | 1.52 | 1.46 | 3.95 | | |
| | 4.82 | 1.39 | 1.48 | 6.47 | | |
| | 5.37 | 1.45 | 1.52 | 4.82 | | |
| | 5.80 | 1.46 | 1.55 | 6.16 | | |
| | 4.46 | 1.44 | 1.45 | 0.69 | | |
| | 5.13 | 1.56 | 1.51 | 3.21 | | |
| | 6.81 | 1.72 | 1.61 | 6.39 | | |

Table 4-5. CHF trends according to surface roughness factor

| CHF validation through surface roughness factor | | | | | | |
|---|---|---|---|---|---|---|
| Papers | Surface enlargement | CHF experimental results (Enhancement ratio) | CHF prediction results (Enhancement ratio) | Deviation (%) | MAE (%) | RMS (%) |
| Chu et al. (2012) | 1.79 | 1.25 | 1.16 | 8.44 | 2.89 | 0.373 |
| | 2.58 | 1.28 | 1.27 | 0.86 | | |
| | 3.19 | 1.34 | 1.34 | 0.43 | | |
| | 3.47 | 1.44 | 1.36 | 5.95 | | |
| | 5.39 | 1.56 | 1.52 | 2.77 | | |
| | 5.94 | 1.58 | 1.56 | 1.84 | | |
| Chu et al. (2013) | 3.8 | 1.66 | 1.40 | 19.1 | 12.4 | 4.47 |
| | 7.2 | 1.74 | 1.64 | 6.37 | | |
| | 8.9 | 2.08 | 1.73 | 20.4 | | |
| | 4.8 | 1.70 | 1.48 | 15.1 | | |
| | 9.2 | 2.05 | 1.74 | 18.3 | | |
| | 12.4 | 2.04 | 1.88 | 8.68 | | |
| | 13.3 | 2.19 | 1.91 | 15.1 | | |
| Wei and Honda (2003) | 2.18 | 1.21 | 1.66 | 36.5 | 17.2 | 10.2 |
| | 3 | 1.31 | 1.54 | 17.3 | | |
| | 4.98 | 1.49 | 1.74 | 16.8 | | |
| | 5.31 | 1.52 | 1.62 | 6.89 | | |
| | 6.39 | 1.59 | 1.93 | 21.4 | | |
| | 7.65 | 1.66 | 1.72 | 3.38 | | |
| Dhilon et al. (2015) | 1.01 | 1.03 | 1.02 | 2.57 | 16.4 | 9.42 |
| | 1.04 | 1.25 | 1.01 | 23.8 | | |
| | 1.04 | 1.34 | 1.01 | 32.7 | | |
| | 1.11 | 1.43 | 1.02 | 39.4 | | |
| | 1.38 | 1.38 | 1.08 | 27.9 | | |
| | 1.40 | 1.25 | 1.08 | 15.0 | | |
| | 1.43 | 1.16 | 1.09 | 6.28 | | |
| Kruse et al. (2015) | 3.85 | 1.40 | 1.27 | 9.33 | 9.28 | 9.28 |

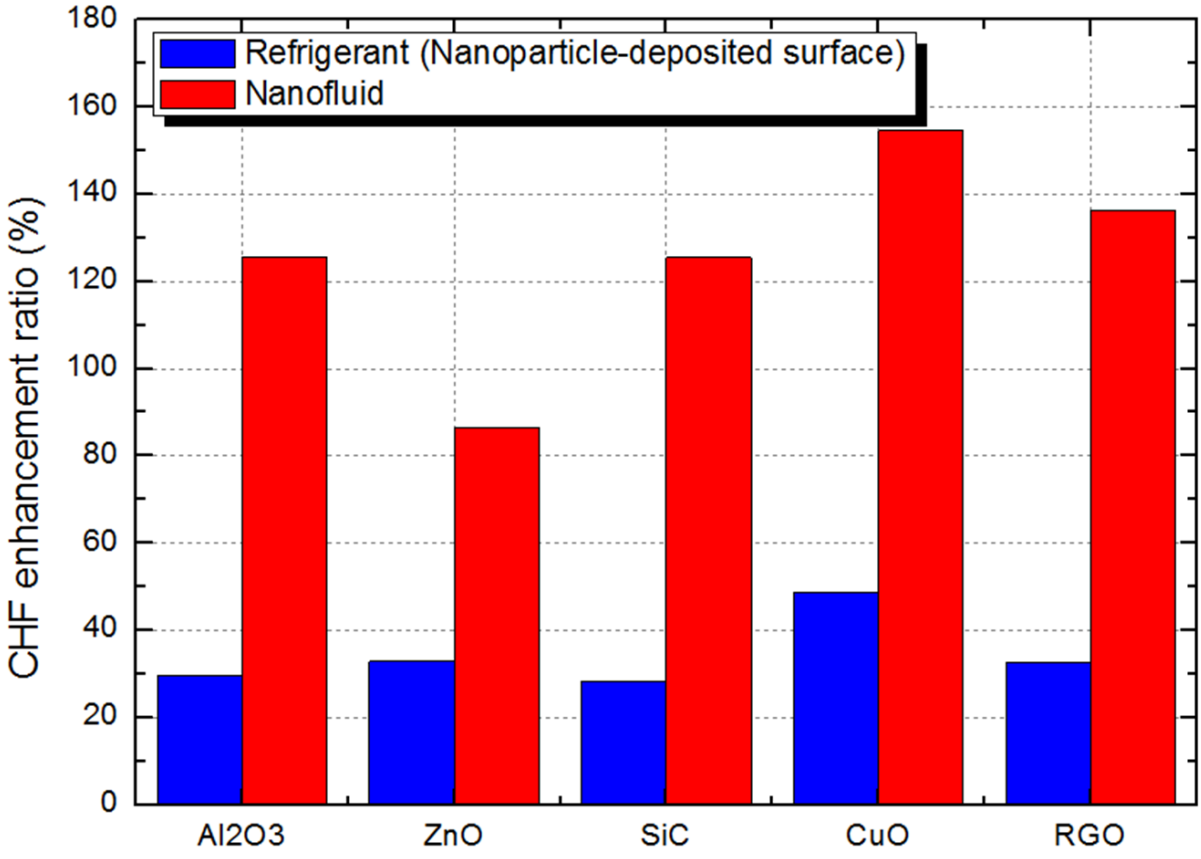


Fig. 4-2. Comparison of the CHF enhancement ratio (present experiments and literature[11])

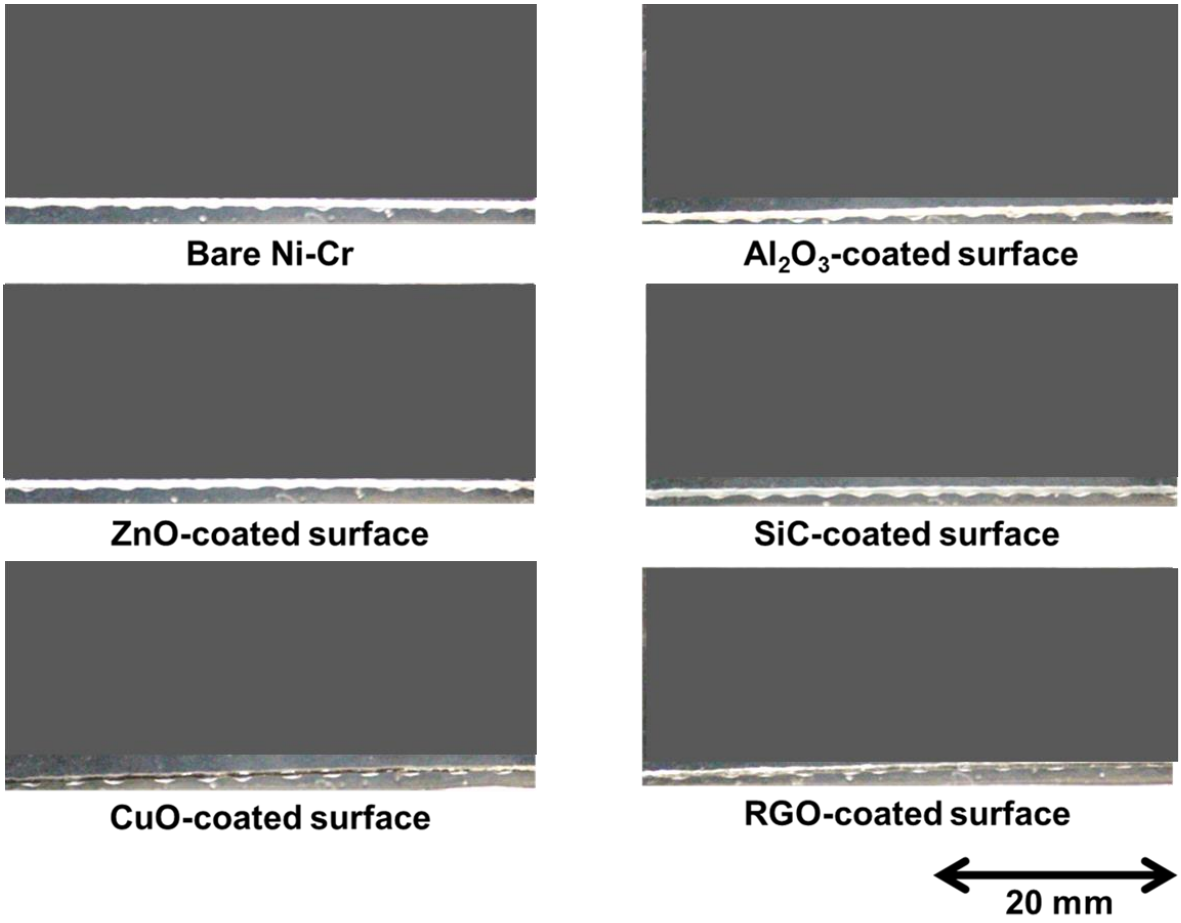


Fig. 4-3. Measurement of RT instability wavelengths with condensation method with various nanoparticle-coated surfaces

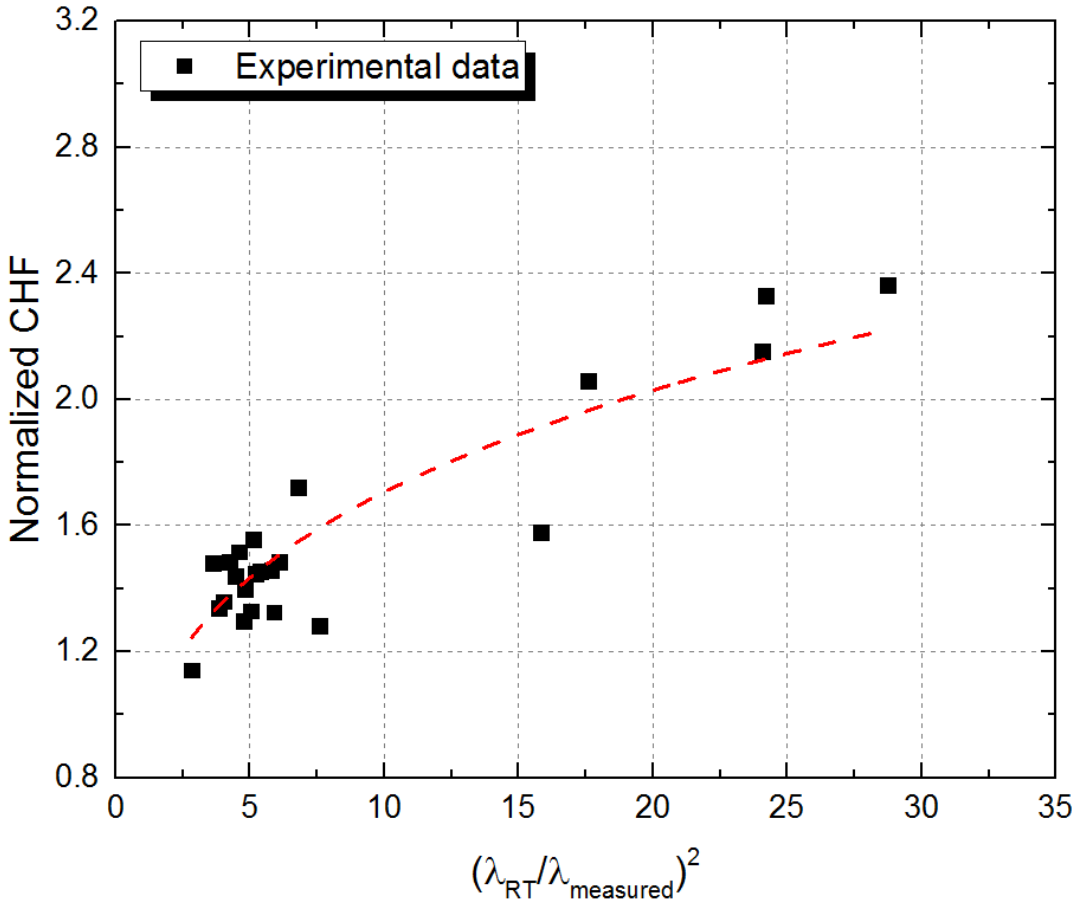


Fig. 4-4. Experimental data for RT instability wavelengths

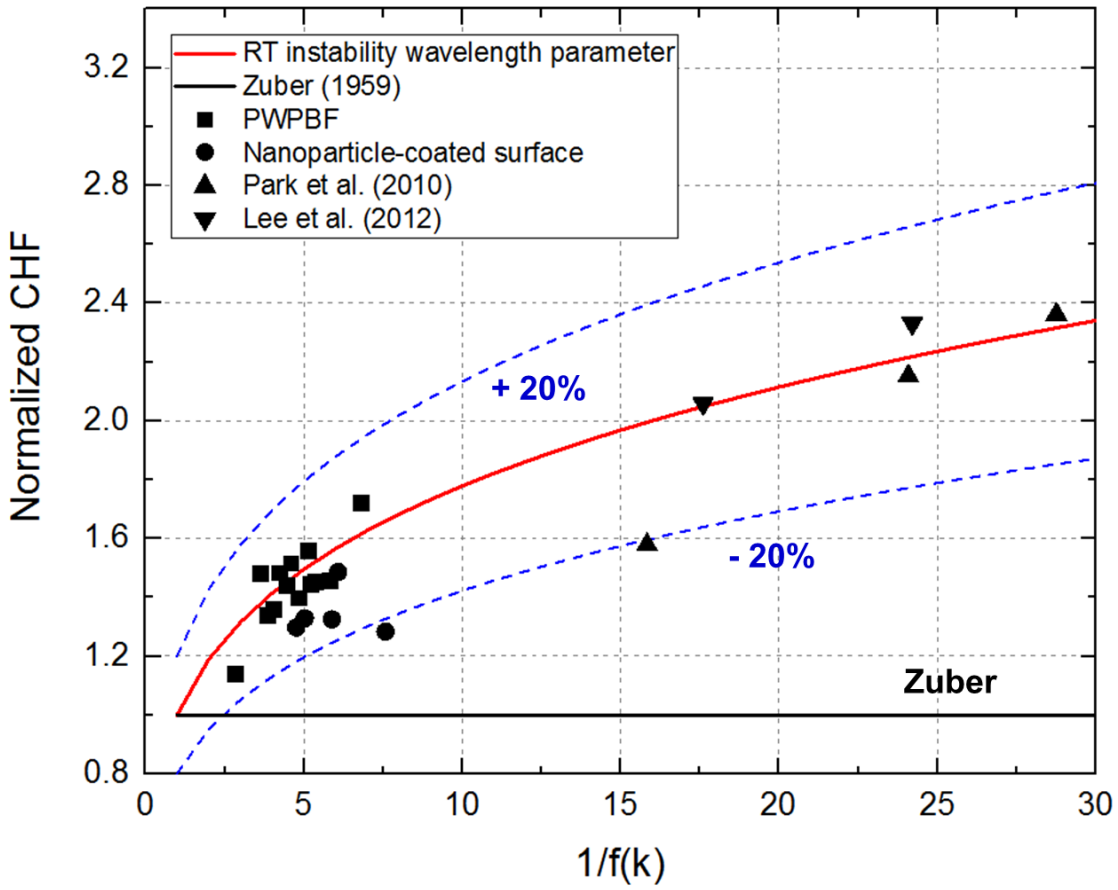


Fig. 4-5. Comparison between the experimental CHF results and the prediction CHF values (RT instability wavelength factor)

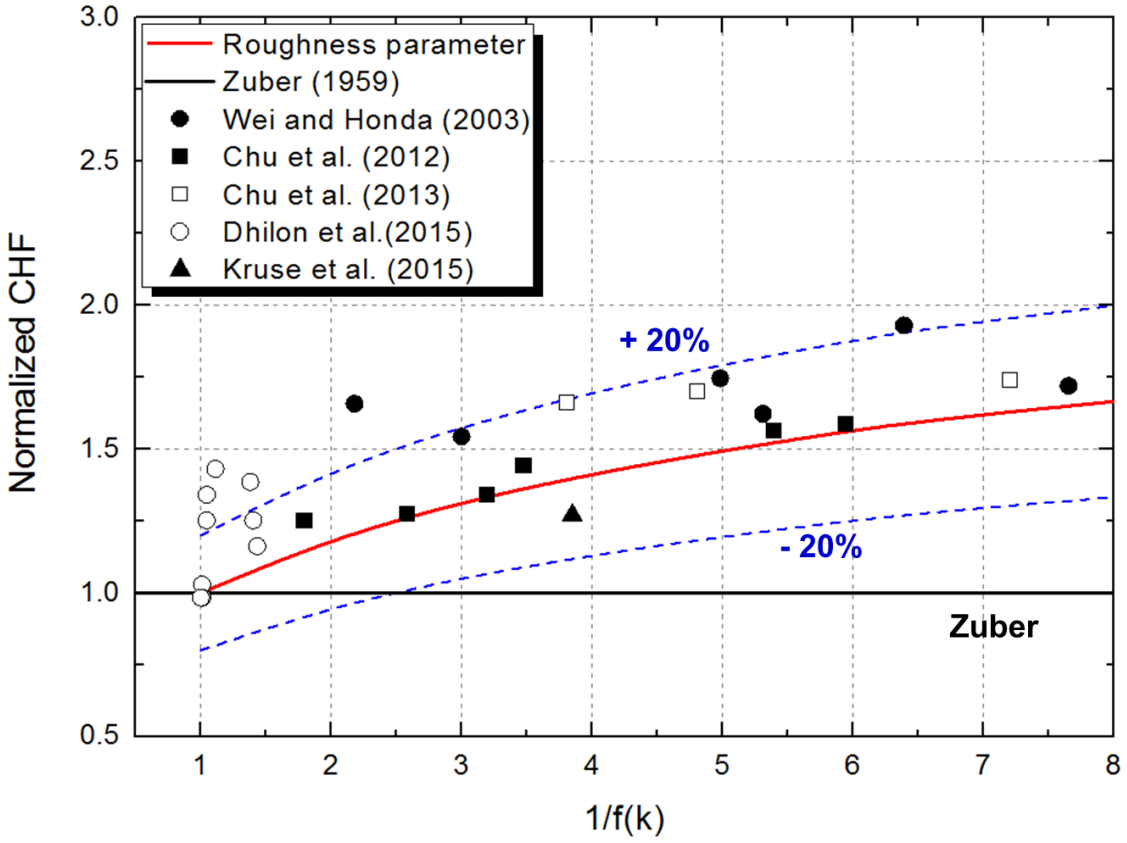


Fig. 4-6. Comparison between the experimental CHF results and the prediction CHF values (surface roughness factor)

### 4.5 Conclusions

The modified hydrodynamic instability CHF prediction model was proposed by considering the effects of surface characteristics on the pressure balance of the wavy interface. Reviews of CHF models based on hydrodynamic instability theory were discussed and the originality of the modified CHF model was proposed. The derivation of the CHF model with considering the surface curvature functions was conducted and the validation of procedure with existing CHF results which considered surface roughness and RT instability wavelength factors. Following conclusions were obtained.

(1) The modified CHF model with the change of pressure balance at the interface by using the surface curvature function was discussed. Two kinds of surface characteristics were considered: surface roughness and RT instability wavelength factors. For the surface roughness factor, it was defined by the ratio of the projected area divided by the actual surface area. In addition, the RT instability wavelength factor was considered as the measured RT instability wavelengths on various heating conditions. The CHF trends according to the surface roughness and RT instability wavelength factors were obtained.

(2) For the surface roughness factor, various kinds of experimental results were considered into the validation procedure of the modified hydrodynamic CHF model. The experimental data were obtained from several literatures. Surface modification techniques were employed to control the surface enlargement ratio compared to the plain heating surfaces. The surface enlargement ration was ranged from 1 to 13.3, and the maximum CHF enhancement ratio was obtained as 2.19. By comparing the prediction CHF values with the experimental results, the modified CHF model with the surface roughness factor is valid in the pool boiling experiments.

(3) For the RT instability wavelength factor, various deposition of nanoparticle-coated surfaces were considered with various working fluids and RT instability wavelength measurements under different pressures and heater diameters were conducted in pressurized wire pool boiling facility. The RT instability results for the nanoparticle-coated surfaces were performed by the condensation method using the water and the FC-72 refrigerant. For the pressurized wire pool boiling, the RT instability wavelengths were confirmed as the CHF variation parameter and the different heater diameters indicated that the CHF prediction model based on hydrodynamic instability theory should consider the heater surface characteristics. Various conditions of RT instability factor were employed to validate the modified CHF model: the maximum of the RT instability factor and the CHF enhancement results was 7.38 and 2.36 respectively. Most of experimental data were fitted to the modified hydrodynamic CHF model within ± 20%. The results indicated that the RT instability wavelength factor as the parameter of the modified CHF model was validated.

# Chapter 5. CONCLUSIONS AND RECOMMENDATIONS

## 5.1 Conclusions

### 5.1.1 Pool boiling CHF enhancement experiments

Porous and nonporous heating surfaces were examined in the pool boiling experiments with the FC-72 refrigerant to suppress the wettability effect. In addition, hybrid graphene/SWCNTs heating surface was used to show the effect of improved thermal conductivity on the boiling performance. The experimental results indicated that porous heating structures were the main mechanism on the CHF performance due to the porosity and the permeability effects. For the thermal effusivity effect, hybrid graphene/SWCNTs surface showed the best performance compared to the bare ITO, graphene, and SWCNTs heating surfaces. The improved CHF can be explained by several surface parameters, but it is hard to quantify the CHF performance based on the surface parameters. Therefore, several CHF models were discussed to support the experimental results and the hydrodynamic instability theory was determined as the mechanism model.

### 5.1.2. CHF experiments based on hydrodynamic instability theory

The pressurized wire pool boiling and patterned Pt surfaces were conducted to show the relation between the RT instability wavelength and the CHF results. The results insisted that the RT instability wavelength should consider the surface characteristics to support the CHF variations.

### 5.1.3 Modified hydrodynamic instability CHF prediction model

Modified hydrodynamic instability CHF model was developed based on the change of the RT instability wavelength with the surface characteristics. The surface characteristics were considered as the surface function. As the surface function, measured RT instability wavelength and surface roughness factors were examined for the validation of the model. The results indicated that the surface roughness factor and the RT instability wavelength factor as the parameter of the modified CHF model were valid in the present work.

## 5.2 Recommendations

The CHF enhancement due to the surface modifications can be predicted by the modified hydrodynamic CHF model. In nuclear conditions, there would be chalk river unidentified deposits

(CRUD) formation on fuel rods during reactor operation. Typically, CRUD deposition on fuel rods can be regarded as the negative effects on operating conditions. But the CRUD deposition layer has naturally porous structure with hydrophilic characteristics, which the deposition characteristics are similar to the deposition of nanoparticles on heating surfaces. Therefore, CRUD quantification experiments are possible through the deposition of nanoparticles and the modified hydrodynamic CHF model can predict those of deposition characteristics by controlling the surface parameters. In addition, the surface modification techniques can be applied on the cladding surfaces because the modified CHF model can support the CHF enhancement results.

**References**


1. You, S.M.; Kim, J.H.; Kim, K.H. Effect of nanoparticles on critical heat flux of water in pool boiling heat transfer. Appl. Phys. Lett. 2003, 83, 3374.
2. Vassallo, P.; Kumar, R.; D'Amico, S. Pool boiling heat transfer experiments in silica–water nano-fluids. Int J Heat Mass Transf. 2004, 47, 407-411
3. Bang, I.C.; Chang, S.H. Boiling Heat Transfer Performance and Phenomena of Al2O3-water Nano-fluids. Int. J. Heat Mass Transf. 2005, 48, 2407-2419.
4. Kim, S.J.; Bang, I.C.; Buongiorno, J.; Hu, L.W. Effects of Nanoparticle Deposition on Surface Wettability Influencing Boiling Heat Transfer in Nanofluids. Appl. Phys. Lett. 2006, 89, 153107.
5. Kim, S.J.; Bang, I.C.; Buongiorno, J.; Hu, L.W. Surface wettability change during pool boiling of nanofluids its effect on critical heat flux. Int. J. Heat Mass Transf. 2007, 50, 4105-4116.
6. Kim, H.; Kim, M. Experimental study of the characteristics and mechanism of pool boiling CHF enhancement using nanofluids. Heat Mass Transf. 2009, 45, 991-998.
7. Geradi, C.; Buongiorno, J.; Hu, L.; McKrell, T. Infrared thermometry study of nanofluid pool boiling phenomena. Nanoscale Res. Lett. 2011, 6, 232.
8. Polezhaev, Y.V.; Kovalev, S.A. Modelling heat transfer with boiling on porous structures. Thermal Engineering. 1990, 37, 617-620.
9. Liter, C.S.; Kaviany, M. Pool-boiling CHF Enhancement by Modulated Porous-layer Coating: Theory and Experiment. Int. J. Heat Mass Transfer, 2001, 44, 4287-4311.
10. Park, S.D.; Lee, S.W.; Kang, S.; Bang, I.C.; Kim, J.H.; Shin, H.S.; Lee, D.W.; Lee D.W. Effects of Nanofluids Containing Graphene/Graphene-oxide Nanosheets on Critical Heat Flux. Appl. Phys. Lett. 2010, 97, 023103.
11. Park, S.D.; Bang, I.C. Experimental Study of a Universal CHF Enhancement Mechanism in Nanofluids Using Hydrodynamic Instability. Int. J. Heat Mass Transf. 2014, 70, 844-850.
12. Seo, H.; Chu, J.H.; Kwon, S.; Bang, I.C. Pool boiling CHF of reduced graphene oxide, graphene, and SiC-coated surfaces under highly wettable FC-72. Int. J. Heat Mass Transf. 2015, 82, 490-502.
13. Amiri, A.; Shanbedi, M.; Amiri, H.; Heris, S.Z.; Kazi, S.N.; Chew, B.T.; Eshghi, H. Pool boiling heat transfer of CNT/water nanofluids. Appl. Therm. Eng. 2014, 71, 450-459.
14. Seo, H.; Yun, H.D.; Kwon, S.; Bang, I.C. Hybrid Graphene and Single-Walled Carbon Nanotube Films for Enhanced Phase-Change Heat Transfer. Nano Lett. 2016, 16, 932-938.
15. Jones, B.J.; McHale, J.P.; Garimella, S.V. The Influence of Surface Roughness on Nucleate Pool Boiling Heat Transfer. J. Heat Transf.-Trans. ASME. 2009, 131, 121009.
16. Das, A.K.; Das, P.K.; Saha, P. Performance of different structured surfaces in nucleate pool boiling. Appl. Therm. Eng. 2009, 29, 3643–3653.

17. Hosseini, R.; Gholaminejad, A.; Nabil M. Concerning the effect of surface material on nucleate boiling heat transfer of R-113. J. Electron. Cooling Thermal Control. 2011, 1, 22–27.
18. Patil, C.M.; Kandlikar, S.G. Pool boiling enhancement through microporous coatings selectively electrodeposited on fin tops of open microchannels. Int. J. Heat Mass Transf. 2014, 79, 816-828.
19. Choi, J.; NO, H.C.; Yeo, D.Y. Analysis of CHF enhancement by heater surface fin structure ranging from micrometer-fin scale to centimeter-fin scale. Proceedings of ICAPP. 2013, KF113.
20. Wang, T.; Jian, Y.; Jiang, H.; Guo, C.; Guo, C.; Tang, T.; Rong, L. Surface with recoverable mini structures made of shape-memory alloys for adaptive-control of boiling heat transfer. Appl. Phys. Lett. 2015, 107, 023904.
21. Choi, S.U.S.; Eastman, J.A. Enhancing thermal conductivity of fluids with nanoparticles. in: The Proceedings of the 1995 ASME International Mechanical Engineering Congress and Exposition. San Francisco, USA, ASME, FED 231/MD66: 99–105
22. Zuber, N. Hydrodynamic aspects of boiling heat transfer. Ph.D. Thesis, Univ. of California, 1959.
23. Rohsenow, W.M. A Method of correlating heat transfer data for surface boiling of liquids. Trans. ASME. 1952, 74, 969-976
24. Jung, J.A.; Kim, S.H.; Shin, S.H.; Bang, I.C.; Kim, J.H. Feasibility Study of Fuel Cladding Performance for Application in Ultra-long Cycle Fast Reactor. J. Nucl. Mater. 2013, 440, 596-605.
25. Lee, S.W.; Park, S.D.; Kang, S.; Bang, I.C.; Kim, J.H. Investigation of viscosity and thermal conductivity of SiC nanofluids for heat transfer applications. Int. J. Heat Mass Transf. 2011, 54, 433-438.
26. Novoselov, K.S.; Geim, A.K.; Morozov, S.V.; Jiang, D.; Zhang, Y.; Dubonos, S.V.; Grigorieva, L.V.; Firsov, A.A. Electric field effect in atomically thin carbon films. Science 2004, 306, 666−669.
27. Geim, A.K.; Novoselov, K.S. The rise of graphene. Nat. Mater. 2007, 6, 183−191.
28. Balandin, A.A.; Ghosh, S.; Bao, W.; Calizo, I.; Teweldebrhan, D.; Miao, F.; Lau, C.N. Superior Thermal Conductivity of Single-Layer Graphene. Nano Lett. 2008, 8, 902−907
29. Toh, S.Y.; Loh, K.S.; Kamarudin, S.K.; Daud, W.R.W.; Graphene production via electrochemical reduction of graphene oxide: Synthesis and characterization. Chem. Eng. J. 2014, 251, 422-434.
30. Chu, J.H.; Kwak, J.; Kwon, T.; Park, S.; Go, H.; Kim, S.Y.; Park, K.; Kang, S.; Kwon, S. Facile Synthesis of Few-Layer Graphene with a Controllable Thickness Using Rapid Thermal Annealing. Appl. Mater. Interfaces. 2012, 4, 1777-1782.
31. Kim, H.D.; Kim, M.H. Effect of nanoparticle deposition on capillary wicking that influences the critical heat flux in nanofluids. Appl. Phys. Lett. 2007, 91, 014104.
32. Ahn, H.S.; Jo, H.J.; Kang, S.H.; Kim, M.H. Effect of liquid spreading due to nano/microstructures on the critical heat flux during pool boiling. Appl Phy Lett. 2011, 98, 071908K.
33. Park, S.D.; Moon, S.B.; Bang, I.C. Effects of thickness of boiling-induced nanoparticle deposition on the saturation of critical heat flux enhancement. Int. J. Heat Mass Transf. 2014, 78, 506-514.

34. Golobic, I.; Bergles, A.E. Effects of heater-side factors on the saturated pool boiling critical heat flux. Exp. Thermal Fluid Sci. 1997, 15, 43-51.
35. Saylor, J.R. An Experimental Study of the Size Effect in Pool Boiling Critical Heat Flux on Square Surfaces. M.S Thesis, Univ. of Minnesota, 1989.
36. Cossali, G. E.; Marengo, M.; Santini, M. Effects of wall effusivity on secondary droplet atomisation from single and multiple drop impact onto heated surfaces. In: Proceedings of ILASS-Europe'05, 2005, Orelean, France.
37. Cossali, G. E.; Marengo, M.; Santini, M.; Fest, S. Effect of wall effusivity on thermally induced secondary atomization of single drop impacting onto a tilted surface. In: Proceedings of ICLASS-2006, 2006, Kyoto, Japan.
38. Bombardieri, C.; Manfletti, C. Influence of wall material on nucleate pool boiling of liquid nitrogen. Int. J. Heat Mass Transf. 2016, 94, 1−8.
39. Chen, R.; Lu, M.; Srinivasan, V.; Wang, Z.; Cho, H.H.; Majumdar, A. Nanowires for Enhanced Boiling Heat Transfer, Nano Lett. 2009, 9, 548-553.
40. Sadasivan, P.; Chappidi, R.P.; Unal, C.; Nelson, R.A.; Possible mechanisms of macrolayer formation. Int. Comm. Heat Mass Transf. 1992, 19, 801-815.
41. Rohsenow, W. M.; Griffith, P. Correlation of maximum heat flux data for boiling of saturated liquids. Cambridge, Mass.: Massachusetts Institute of Technology, Division of Industrial Cooperation, 1955.
42. Kolev, N.I. How can we predict nucleate boiling? Exp. Therm. Fluid. Sci. 1995, 10, 370-378
43. Theofanous, T.G.; Tu, J.P.; Dinh, A.T.; Dinh, T.N. The boiling crisis phenomenon: Part I: nucleation and nucleate boiling heat transfer. Exp. Therm. Fluid Sci. 2002, 26, 775-792.
44. Theofanous, T.G.; Dinh, T.N.; Tu, J.P.; Dinh, A.T. The boiling crisis phenomenon part II: dryout dynamics and burnout. Exp. Therm. Fluid. Sci. 2002, 26, 793-810
45. Theofanous, T.G.; Dhin, T.N. High heat flux boiling and burnout as a microphysical phenomena: mouting evidence and opportunities. Multiphase Science and Technology. 2006, 18, 251-276.
46. Bang, I.C.; Buongiorno, J.; Hu, L.W.; Wang, H. Measurement of key pool boiling parameters in nanofluids for nuclear applications. JSME J. Power Energy Sys. 2008, 2, 340-351.
47. Chu, I,; NO, H.C,; Song, C,; Euh, D.J. Observation of critical heat flux mechanism in horizontal pool boiling of saturated water. Nucl. Eng. Des. 2014, 279, 189-199.
48. Kim, D.E,; Song, J,; Kim, H. Simultaneous observation of dynamics and thermal evolution of irreversible dry spot at critical heat flux in pool boiling. Int. J. Heat Mass Transf. 2016, 99, 409−424.
49. Jung, S.; Kim, H. Observation of triggering mechanism of critical heat flux during pool boiling of water. The Tenth Korea-Japan Symposium on Nuclear Thermal Hydraulics and Safety. N10E1006.
50. Kandlikar, S.G. A Theoretical Model to Predict Pool Boiling CHF Incorporating Effects of Contact Angle and Orientation. J Heat Transfer. 2001, 123, 1071-1079.

51. Maeng, Y.H.; Song, S.L.; Lee, J.Y. Unaffectedness of improved wettability on critical heat flux enhancement with TiO2 sputtered surface. Appl. Phys. Lett. 2016, 100, 074101.
52. Quan, X.; Dong, L.; Cheng, P. A CHF model for saturated pool boiling on a heated surface with micro/nano-scale structures. Int. J. Heat. Mass. Transf. 2014, 76, 452-458.
53. Kim, J.; Jun, S.; Laksnarain, R.; You, S.M. Effect of surface roughness on pool boiling heat transfer at a heated surface having moderate wettability. Int. J. Heat Mass Transf, 2016, 101, 992-1002.
54. Lee, S.W.; Park, S.D.; Bang, I.C. Critical heat flux for CuO nanofluid fabricated by pulsed laser ablation differentiating deposition characteristics. Int. J. Heat Mass Transf. 2012, 55, 6908-6915.
55. Lienhard, J.H.; Wong, P.T.Y. The dominant unstable wavelength and minimum heat flux during film boiling on a horizontal cylinder. J. Heat Transfer. 1964, 86, 220-225.
56. Ho, J.Y.; Wong, K.K.; Leong, K.C. Saturated pool boiling of FC-72 from enhanced surfaces produced by selective laser melting. Int. J. Heat Mass Transf. 2016, 99, 107-121.
57. Lienhard, J.H.; Dhir, V.K. On the prediction of the minimum pool boiling heat flux. J. Heat Transf.-Trans. ASME. 1980, 102, 457-460.
58. Lu, M.; Chen, R.; Srinivasan, V.; Carey, V.P.; Majumdar, A. Critical heat flux of pool boiling on Si nanowire array-coated surfaces. Int. J. Heat Mass Transf. 2011, 54, 5359-5367.
59. Lu, M.; Hung, C.; Huang, C.; Chen, Y. A modified hydrodynamic model for pool boiling CHF considering the effects of heater size and nucleation site density. Int. J. Therm. Sci. 2015, 91, 133-141.
60. Lee, J.Y. Lee, W. Effect of Kelvin-Helmholtz instability on CHF for thin flat plate heater, Proceedings of the 15th International Heat Transfer Conference, IHTC-15. 2014, IHTC15-9423.
61. Jun, S.; Sinha-Ray, S.; Yarin, A.L. Pool boiling on nano-textured surfaces. Int. J. Heat Mass Transf. 2013, 62, 99-111.
62. Kim, B.J.; Lee, J.H.; Kim, K.D. Rayleigh–Taylor instability for thin viscous gas films: Application to critical heat flux and minimum film boiling. Int. J. Heat Mass Transf. 2015, 80, 150-158.
63. Chu, K.; Enright, R.; Wang, E.N. Structured surfaces for enhanced pool boiling heat transfer. Appl. Phy. Lett. 2012, 100, 241603.
64. Chu, K.; Joung, Y.S.; Enright, R.; Bule, C.R.; Wang, E.N. Hierarchically structured surfaces for boiling critical heat flux enhancement. Appl. Phy. Lett. 2013, 102, 151602.
65. Lamb, H. Hydrodynamics, 6th edition, Dover Publications, New York, 1932.
66. Bellman, R.E.; Pennington, R.H. Effects of surface tension and viscosity on Taylor instability. Quar. Appl. Math. 1954, 12, P-403.
67. Wei, J.J.; Honda, H. Effects of fin geometry on boiling heat transfer from silicon chips with micro-pin-fins immersed in FC-72. Int. J. Heat Mass Transf. 2003, 46, 4059-4070.
68. Dhilon, N.S.; Buongiorno, J.; Varanasi, K.K. Critical heat flux maxima during boiling crisis on textured surfaces. Nat. Commun. 2015, 6, 8247.

69. Kruse, C.M.; Anderson, T.; Wilson, C.; Zuhlike, C.; Alexander, D.; Gogos, G.; Ndao, S. Enhanced pool-boiling heat transfer and critical heat flux on femtosecond laser processed stainless steel surfaces. Int. J. Heat Mass Transf. 2015, 82, 109-116.

**Acknowledgements (감사의 글)**

2011년 8월 UNIST에 입학하여 어느덧 5년 반의 시간 동안 석박사 통합과정을 마무리하게 되었습니다. 지난 시간을 돌이켜 보면, 항상 어떠한 것에 쫓기 듯이 집중을 하지 못하는 나날을 보낸 것 같습니다. 이러한 저를 다독여 주시고 격려 해주시는 주위의 분들 덕분에 학위 과정을 마칠 수 있었습니다. 대학원 생활을 하는데 있어 주위의 많은 분들의 도움이 없었다면 제가 이런 감사의 글을 쓸 수 있을까 싶습니다. 이 자리를 빌어 다시 한번 저에게 도움을 주신 모든 분들에게 감사드립니다.

우선 석박사 통합과정동안 저에게 많은 지도 및 격려를 아끼시지 않으셨던 지도교수님이신 방인철 교수님께 깊은 감사의 말씀을 전달해 드립니다. 철이 없던 저를 항상 다독여 주시고 교수님의 열정적인 가르침 덕분에 제가 학위 과정을 마치게 되었습니다. 연구에 대한 깊은 철학이 없었던 저에게 연구의 시작과 끝을 맺는 법을 열정적으로 가르쳐 주시고 연구에 있어서 조급함을 가지지 말고 꾸준히 연구를 하는 법을 항상 강조하신 것을 앞으로 사회에 나가서도 잊지 않도록 하겠습니다. 교수님께서 강조하신 나무를 보지 말고 숲을 보아라 라는 것을 명심하고 연구에 매진하도록 하겠습니다. 또한 사람과의 관계 및 연구를 진행하는데 있어 책임감의 중요성을 강조하신 것을 마음속 깊이 간직하겠습니다. 아직까지 교수님의 가르침에 대하여 모든 것을 깨닫지는 못하였지만 앞으로 교수님의 말씀을 이해하도록 노력하겠습니다. 감사합니다. 또한 바쁘신 와중에도 제 학위 논문을 지도해주시고 격려해주신 김지현 교수님, 신흥주 교수님, 이재영 교수님, 최기용 박사님께 이자리를 빌어 감사드립니다.

대학원 생활에 있어 연구실 식구들은 항상 저에게 큰 힘이 되었습니다. 우선 먼저 사회에 진출하신 4분의 선배님께 감사의 말씀을 전합니다. 이승원 박사님, 박성대 박사님, 강사라 박사님, 김성만 선배님. 철 없던 저에게 먼 곳에서도 많은 조언을 해주신 덕분에 제가 이런 감사의 글을 쓸 수 있게 되었습니다. 앞으로는 제가 연구실 후배들에게 선배님들이 해 주신 것처럼 많은 도움을 줄 수 있도록 노력하겠습니다. 그리고 연구실 후배들에게도 큰 감사의 말씀을 전합니다. 이제 랩의 최고참이 되어 많은 일들을 꾸려 나가고 있는 경모. 너의 연구 실력은 정말 뛰어나다고 생각해. 지금과 같은 열정으로 연구에 매진한다면 좋은 결과와 많은 것들을 이뤄낼 수 있다고 생각해. 항상 파이팅이다. 경모와 마찬가지로 다양한 일을 하면서 중심을 잃지 않고 있는 석빈. 가끔 너의 지치지 않는 연구 집중력을 보고 있으면 내가 보기에도 엄청 대단해. 그 마음 잃지 않고 생활에 나갔으면 좋겠다. 지금은 미국에 가 있는 성보, 너의 유니크한 특징을 잘 살려서 연구에도 잘 적용했으면 좋겠다. 미국에서 많은 것들을 얻고 깨닫고 오게 되면 나에게도 알려주길 바랄게. 그리고 경모, 석빈, 성보와 같은 동기이지만 한학기 늦게 들어와서 고생하고 있는 인국이. 너의 독창적인 연구 아이디어를 보면서 항상 부럽다는 생각을 많이 했어. 항상 열정적으로 일에 집중한다면 정말 좋은 연구 결과들이 쏟아져 나올 것 같다. 성보와 같이 미국에서 열심히 연구하고 있는 효, 항상 파이팅하고 너의 지치지 않는 연구 체력을 보여주었으면 해. 미국에서 많은 것들을 얻어 오길 바란다. 언제나 열정적이고 모범적인 영신이. 지치지 않는 연구 능력을 발휘해서 좋은 결과를 얻길 바랄께. 이제 본격적인 실험을 시작하는 규민이, 힘든 실험이 시작되겠지만 나 포함 다른 선배들에게 도움을 요청하면 최대한 잘 도와줄거야. 이제 나와 같이 사회로 나갈 유경이, 사회에

나가서 너의 능력을 발휘했으면 해. 선배들에게 이리 치이고 저리 치이는 민호, 너의 그 꾸준함을 계속 가져간다면 선배들보다 훨씬 뛰어난 연구 성과를 낼 수 있을 것이라고 생각해. 그리고 연구실 막내인 수민이, 선배들 사이에서 생활하느라 고생이 많다. 너의 꾸준한 연구 능력을 간직한다면 조만간 좋은 결과를 만들 것이라고 생각해.

그리고 원자력공학과 다른 연구실 대학원분들에게도 깊은 감사의 말씀을 드립니다. 2011년 초창기 대학원생들이 다같이 모여 생활하였던 102동 406호 분들에게 울산에 연고도 없던 저에게 많은 것들을 베풀어 주신 김종진 박사님, 신상훈 박사님, 정주앙 선배님, 조병진 선배님께 감사드립니다. 또한 제 초중고 선배이시고 제 친형의 친구이기도 한 먼저 사회로 나가 있는 태우형, 조만간 저도 사회에 발돋움 하도록 하겠습니다. 나와 동갑이고 대학원 생활 초기에 많은 도움을 준 경준이, 항상 파이팅하고 좋은 결과를 가지고 나중에 기분 좋게 술한잔 합시다. 또한 저에게 많은 격려를 해준 승현, 태호, 상일, 승창, 정현, 욱제, 관윤, 수영 등 원자력공학과 선후배들에게 깊은 감사의 말씀을 드립니다. 저에게 과분한 연구 결과를 낼 수 있도록 도와준 다른 과 대학원 분들에게도 감사합니다. 또한 좋은 연구 결과를 낼 수 있도록 실험 장치들을 열성적으로 세팅해 주신 네오시스 이종수 사장님께 감사의 말씀을 전달합니다.

또한 제 친구 및 학부 선후배들에게도 이 자리를 빌어 감사의 말씀을 전합니다. 언제나 제가 서울을 올라가고 힘들 때마다 만나준 친구들, 재승, 승완, 재구, 진태, 동운, 승한, 석연, 헌훈, 예준, 준형, 범주 등 많은 친구들에게 직접 만나서 말을 못하지만 여기에 고맙다는 말을 전한다. 또한 학부 때 연구실 생활을 간접적으로 경험하면서 많은 도움을 주신, 경동이형, 성휴형, 명근이형에게 감사하다고 전하고 싶습니다. 곧 제가 사회로 나가니 좋은 대접을 해드리겠습니다. 또한 다른 연구 분야에 대해서 궁금한 거 있으면 물어보는 명식이. 귀찮아 하지 않고 자세히 대답해줘서 고맙다. 내 꼬드김에 넘어가 UNIST로 오게 되어 석박사 통합과정을 하고 있는 영진이. 조금만 더 열심히 한다면 좋은 결과와 함께 너가 원하는 곳으로 갈 수 있을 거야. 그리고 학부 지도교수이신 심재우 교수님께도 감사의 말씀을 드립니다.

마지막으로 제가 하는 것마다 믿어주시고 격려해주는 사랑하는 부모님께도 깊은 감사의 말씀을 드립니다. 제 미래에 대해서 확신을 가지지 못할 때 부모님의 격려가 없었다면 이 자리는 없었을 것입니다. 깊은 사랑으로 올바른 길을 갈 수 있도록 해 주신 부모님. 감사합니다. 그리고 제 친형과 형수님께도 감사의 인사 드립니다.

2017년 1월
서 한